

# **Lithological Relevance of Near-surface Seismic Velocity Model**

**von der Naturwissenschaftlichen Fakultät  
der Gottfried Wilhelm Leibniz Universität Hannover**

zur Erlangung des Grades

Doktorin Der Naturwissenschaften

Dr.rer.nat.

genehmigte Dissertation

von

**M.Sc. Genet Tamiru**

geboren am 12.10.1973 in Addis Abeba

2009

Referent: Prof. Dr. Hans-Joachim Kümpel

Korreferentin: Prof. Dr. Jutta Winsemann

Tag der Promotion: 14.07.2009

## Abstract

The objective of this work is twofold. One of the objectives is to assess the viability of the seismic refraction tomography method to delineate shallow subsurface information using first arrival traveltimes from standard reflection data. In a standard seismic reflection method it is difficult or impossible to obtain information in the very near surface depth range where surface waves or refracted waves overlap seismic reflections. To fill this lack of information arrival times of refracted waves – unwanted signals in the reflection survey – are analysed by the first arrival refraction tomography method with the aim to complement the stacked seismic section by a detailed velocity model for the near-surface area.

The second objective is using high resolution seismic reflection P- and S-wave data: to adapt the P-wave survey parameters for high resolution information, to use shear waves instead of compressional waves for near-surface study, and to demonstrate the significance of the  $V_p$  to  $V_s$  ratio to characterize the near-surface lithology. Even though high-resolution P- and S-wave seismic reflection methods have been used for mapping the near-surface of the earth (e.g. Pugin et al., 2004), there still remains need for further enrichment of these methods for accurate lithological discrimination. This work tries to arrive at an increased understanding of these methods with the aid of newly developed acquisition devices, consisting of a P- and S-wave landstreamer unit and P- and S-wave vibrators (Polom et al., 2007). This research work is carried out in the BurVal pilot project area Ellerbeker Rinne, Northern Germany (BURVAL Working Group, 2006).

A near-surface P-wave velocity model down to a depth of 50 m, with velocity contrasts at ~10 m, ~30 m and ~50 m depths is obtained by a tomographic inversion of first arrivals from conventional seismic reflection data. A total of ~81,000 first arrivals were picked for the velocity calculation. The turning ray tomography inversion method described by Stefani (1995) is employed to define the velocity model which is implemented in ProMAX software. The resultant velocity model is found to be compatible with knowledge supplied by the borehole, shallow P-wave reflection and AEM data. This model included a thin top layer of mixture of dry sand, till and humus (velocities about 480 – 1020 m/s), a homogeneous layer of saturated sand (velocities about 1480 – 1700 m/s) and a till layer (velocities about 1800 – 2400 m/s).

High resolution shallow P- and S-wave seismic reflection data were acquired along a coincident profile line with the same acquisition parameters (1 m receiver spacing and 2 m shot spacing).

The results of the survey indicate that the two methods have different depths of investigation. The P-wave reflection data is only able to provide the shallowest strong reflection at 25 m depth but the S-wave reflection data gives shallowest strong reflections at about 4 m depth. Conversely the shallow P-wave reflection gives reflection as deep as 200 m but the shallow S-wave reflection is only able to give the deepest strong reflection at about 50 m depth. On the other hand both P- and S-wave reflection sections image comparable features at depths about 25 and 50 m from similar interfaces. The outcome of this investigation as a whole demonstrates that the shallow S-wave reflection has a better potential to image the very near-surface area than the shallow P-wave reflection, and the combined P- and S-wave reflection information allowed the near-surface strata to be imaged more effectively than using solely the P- or S-wave information.

A joint analysis of the P- and S-wave velocities via the velocity ratio in an effort to extract the lithology component of the near-surface zone is also made. The interpretation of  $V_p/V_s$  plots derived from the shallow reflection data constrained by borehole information provided the required details on the lithology of the near-surface sediments. It was found that the  $V_p$  to  $V_s$  ratio (1.5 to 3.8) for the upper 5 m depth is low and is related to a mixture of sand, till and humus in the borehole section. The  $V_p$  to  $V_s$  ratio has a higher value (7.6 to 8.7) between 10 and 20 m. This increase is due to water saturation and correlates to the water saturated sand section. For depths between 25 to 60 m the  $V_p$  to  $V_s$  ratio is approximately within the range from 4.6 to 5.8 which corresponds the till layer. Values within the range of 5.2 to 6.2 for depths below 60 m may be due to the emerging of the clay layer.

Another contribution of this work is some combined interpretation of different geophysical methods - ground penetrating radar, airborne electromagnetics, spectral induced polarization, refraction tomography, shallow P- and S-wave reflection methods. Integration of these different geophysical methods verified the complementarity of the methods for the characterization of the near-surface lithology. It also helped to improve the interpretation of the different seismic methods (refraction tomography, shallow P- and S-wave reflection). In particular the combination of these different geophysical methods together with the borehole information allows to construct a geological model for the area.

*Keywords: Near-surface seismics; seismic velocity; Reflection; Tomography; Lithological prediction*

*Stichworte: Oberflächennahen-Seismik; seismische Geschwindigkeit; Reflexion; Tomographie; lithologische Vorhersage*

# Zusammenfassung

Die Zielsetzung dieser Arbeit ist zweigeteilt: Zum einen geht es darum, die Methode der seismischen Refraktionstomographie, angewendet auf Ersteinsätze reflexionsseismischer Datensätze, auf ihre Brauchbarkeit bezüglich der Erkundung des oberflächennahen Untergrund- bzw. Geschwindigkeitsmodells einzuschätzen. Konventionell erfasste, reflexionsseismische Daten (z.B. Geophonabstand 5 m) liefern meist keine Informationen für den oberflächennächsten Tiefenbereich, da hier Oberflächenwellen oder refraktierte Wellen die reflektierten Einsätze überlagern. Diese Informationslücke wird durch Analyse der refraktierten Wellen - also für die Reflexionsseismik unerwünschte Signale - mit der Methode der Refraktionstomographie geschlossen. Hierbei ergibt sich ein detailliertes Geschwindigkeitsmodell für den oberflächennahen Tiefenbereich mit dem die reflexionsseismische Sektion dann ergänzt werden kann.

Zum anderen wird für die Erkundung des oberflächennahen Untergrundes hochauflösende Reflexionsseismik mit P- und S-Wellen angewendet: die Akquisitionsparameter werden bei P-Wellen dem oberflächennahen Erkundungsziel angepasst und es werden zusätzlich Scherwellen eingesetzt. Das Verhältnis der Geschwindigkeiten von Kompressions- und Scherwellen, also das Verhältnis von  $V_p$  zu  $V_s$ , ergibt einen weiteren wichtigen Parameter zur Charakterisierung des Untergrundes. Hochauflösende Reflexionsseismik mit P- und S-Wellen wurde zwar schon häufiger zur Erkundung des oberflächennahen Untergrundes eingesetzt (z.B. Pugin et al., 2004), es besteht aber weiterhin Forschungsbedarf im Prozessing und insbesondere bezüglich der lithologischen Interpretation der Daten. In dieser Arbeit wird versucht, ein erhöhtes Verständnis für diese Methoden zu bekommen, unter anderem auch durch den Einsatz neu entwickelter seismischer P- und S-Wellen Quellen sowie P- und S-Wellen Landstreamer (Polom et al., 2007). Die Untersuchungen finden statt in einem Testfeld des Projektes BURVAL und zwar im Gebiet der Ellerbeker Rinne in Schleswig-Holstein (BURVAL Working Group, 2006).

Aus der tomographischen Inversion der Ersteinsätze eines konventionellen seismischen Datensatzes wird ein Geschwindigkeitsmodell für den Tiefenbereich bis 50 m ermittelt und es werden Geschwindigkeitsänderungen bei ca. 10 m, 30 m und 50 m Tiefe erkannt. Insgesamt wurden 81.000 Ersteinsätze für die Geschwindigkeitsberechnung gepickt. Für die Geschwindigkeitsberechnung wurde die „turning ray tomography inversion“ Methode von Stefani (1995) benutzt, die im Programmsystem ProMAX implementiert ist. Das resultierende Geschwindigkeitsmodell zeigt Übereinstimmung mit Bohrungsdaten, flacher P-Wellen

Reflexionsseismik und AEM Daten. Das Modell beinhaltet eine dünne Verwitterungsschicht aus trockenem Sand, Geschiebemergel und Humus (Geschwindigkeiten von 480 m/s bis 1020 m/s), wassergesättigten Sand (Geschwindigkeiten von 1480 m/s bis 1700 m/s) sowie Geschiebemergel (Geschwindigkeiten von 1800 m/s bis 2400 m/s).

Hochauflösende reflexionsseismische Daten mit P- und S-Wellen wurden entlang desselben Profils und mit gleichen Messparametern aufgenommen (1 m Geophonabstand, 2 m Vibrationspunktstand). Das Ergebnis zeigt die unterschiedlichen Erkundungstiefen der beiden Verfahren. Die P-Wellen Reflexionsdaten ergeben eine erste kräftige Reflexion bei 25 m Tiefe; die Scherwellendaten ergeben bereits bei 4 m Tiefe die erste kräftige Reflexion. Andererseits werden mit den P-Wellen Reflexionen aus 200 m Tiefe ermöglicht; die tiefste Reflexion der S-Wellen kommt aus 50 m Tiefe. Im Tiefenbereich 25 m bis 50 m werden aber vergleichbare Strukturen abgebildet. Als Ergebnis ist festzuhalten, dass die flachen S-Wellen Reflexionsdaten ein höheres Auflösungsvermögen im oberflächennahen Bereich haben als die P-Wellen. Und dass die kombinierte Interpretation von P- und S-Wellen ein effizientere Abbildung des oberflächennahen Untergrundes ergeben als die Messung mit nur einer Wellenart.

Für die Beschreibung der Lithologie werden P- und S-Wellengeschwindigkeiten und das Verhältnis der Geschwindigkeiten ( $V_p/V_s$ ) analysiert. Die Geschwindigkeiten wurden aus der Reflexionsseismik ermittelt; die Interpretation der  $V_p/V_s$  Daten ergab unter Zuhilfenahme von Bohrlochinformationen detaillierten Aufschluss der Lithologie. Für die oberen 5 m ist das  $V_p/V_s$  Verhältnis gering (1,5 bis 3,8) und korreliert mit einem Gemisch aus Sand, Geschiebemergel und Humus in einer naheliegenden Bohrung. Zwischen 10 m und 20 m ist das Verhältnis höher (7,6 bis 8,7); dieser Anstieg wird auf Wassersättigung zurückgeführt und korreliert mit wassergesättigtem Sand. Für Tiefen zwischen 25 m und 60 m liegt das  $V_p/V_s$  Verhältnis zwischen 4,6 und 5,8 und korreliert mit Geschiebemergel. Werte im Bereich 5,2 bis 6,2 unterhalb 60 m stimmen mit einer auftretenden Tonschicht überein.

Ein weiterer Punkt dieser Arbeit ist die kombinierte Interpretation verschiedener geophysikalischer Methoden: Bodenradar (GPR), Hubschrauber Elektromagnetik (AEM), spektrale induzierte Polarisation (SIP), seismische Refraktionstomographie und flache P- und S-Wellen Reflexionsseismik. Durch die Vernetzung dieser unterschiedlichen Methoden ergibt sich ergänzende Information, die für die Charakterisierung der Lithologie des oberflächennahen Untergrundmodells wertvoll ist. Die Interpretation der seismischen Daten wird dadurch ebenfalls verbessert. Aus der Kombination der Ergebnisse der verschiedenen Methoden sowie Bohrlochinformation wird ein geologisches Modell für das Untersuchungsgebiet erstellt.

# Acknowledgment

Precedence of thanks should go to the Most High, the Omniscient, the fountain of wisdom and knowledge, Who has become a solace in time of despair, strength in time of weakness, company in time of loneliness, health in time of illness, and easing all the ups and downs in my university days. Without Whose blessings, all my endeavors would be fruitless and this very day wouldn't be a reality.

As his living foot prints, I will never and ever forget the sacrifices paid by my late father to make me a real 'person' and for what I am today and to whom I dedicate this 'little' work.

Unreserved tribute is due to my mentor, the erudite, seasoned humane and patient Prof. Dr. Hans-Joachim Kümpel of BGR, whose selfless support is beyond measure. His comments and advices are not only indispensable but keep the work of standard. Words lack the power to express his unprecedented role in easing my stay in Hannover. I am greatly indebted to this person of rare quality for the completion of my dissertation and studies in Leibniz Institute for Applied Geophysics - LIAG.

I owe deep gratitude also to my immediate advisor, Dr. Helga Wiederhold of LIAG, the learned and pragmatic person, whose immense contribution to the present work is expressed not only in the painstaking tasks of correcting successive drafts and in her invaluable advices which become the back bone of this dissertation, but in her whole-hearted dedication from the very out set in the design of my proposal, data processing and crucial guidance as to how I go about the work.

Special credit goes to Professor Dr. Jutta Winsemann of the Institute of Geology, Leibniz University of Hanover, for permitting me, without any hesitation, to be registered in the University, to use all the university's facilities and not the least in securing me a job so that I would focus on my studies.

It would be unbecoming of me to pass with out expressing my words of gratitude to the many who in one way or another contribute for the successful completion of my studies in LIAG in general and the Seismic and Potential Methods Section of the Institute (S1) in particular. In this regard, I

am greatly indebted to Dr. Anton Hermann Bunes for helping process refraction tomography data, Dr. Ulrich Polom, for helping process shallow P- and S-wave reflection data, Franz Binot, Dr. Hanna-Maria Rumpel, and Dr Thies Beilecke for their kind assistance, cooperation, and facilitation.

I would feel remorse if I left with out mentioning in name the following institutes. The Catholic Academic Exchange Service (KAAD) for funding my scholarship above and beyond the regular time, the Leibniz Institute for Applied Geophysics, LIAG, for allowing me to use every facility for the research work, and the Katholische Hochschulgemeinde Hanover – KHG (Catholic Student Community of Hanover) for their keen support, and the Ethiopian community in Hanover for their all rounded support.

I am always grateful for my brother, Tewodros, for his unconditional support, encouragement, and advice.

This acknowledgment won't be complete without mentioning my adorable first-born, a wonderful blessing and a life-time memory of Hanover, the lovely time I had with him during the final year of my studies gave me unprecedented tranquility and strength in finalizing my dissertation.

Last, and most importantly, heart-felt thanks goes to my dearest and beloved husband, Simon, for his constant support, patience understanding and for all his behind-the-scenes roles. Especially, I couldn't imagine overcoming the agony of living apart with out his care and love.



# Contents

<b>Abstract</b>	iii
<b>Zusammenfassung (German Abstract)</b>	v
<b>Acknowledgement</b>	vii
<b>Contents</b>	ix
<b>List of Figures</b>	xi
<b>List of Tables</b>	xx
<b>1. Introduction</b> .....	1
<b>2. Regional Setting</b> .....	4
2.1 Location.....	4
2.2 Geology.....	5
<b>3. Seismic Waves</b> .....	9
3.1 Seismic Waves in Natural Rocks.....	9
3.2 P- and S-wave Velocities.....	12
3.3 Velocity Definitions.....	14
3.4 Different ways to Quantify Seismic Wave Velocities.....	18
3.4.1 Laboratory Measurement.....	19
3.4.2 Vertical Seismic Profiling (VSP).....	20
3.4.3 Sonic Logging.....	21
3.4.4 Velocity Analysis of Surface Seismic Data.....	22
3.5 Factors Affecting Seismic Velocities.....	23
<b>4. Near-Surface Seismic Methods</b> .....	27
4.1 Near-Surface Seismic Reflection Method.....	28
4.1.1 Basic Principles.....	29
4.1.2 Data Acquisition System (source, receiver, geometry).....	31
4.1.3 Reflection Data Processing Fundamentals.....	37

4.2 Refraction Tomography Method.....	42
4.2.1 Different Algorithms.....	43
4.2.2 Basic Computational Steps.....	46
4.3 S-wave Method.....	48
4.3.1 S-wave Generation and Recording.....	49
4.3.2 S-wave Data Processing.....	51
4.4 Surface Wave Method.....	53
<b>5. Field Data Description and Analysis.....</b>	<b>55</b>
5.1 P-wave Seismic Reflection Data of 2005.....	57
5.1.1 Refraction Tomography Result from the Field Data.....	59
5.1.2 Checking the Method with Synthetic Data.....	63
5.2 Shallow P- and S-wave Seismic Reflection Data of 2006.....	67
5.2.1 P-wave Seismic Reflection Data of 2006.....	68
5.2.2 S-wave Seismic Reflection Data of 2006.....	76
5.3 Shallow P- and S-wave Seismic Section Correlation.....	83
5.4 P-wave Velocity Field: Conventional P-wave refraction Tomography Vs. Shallow P- wave Reflection.....	86
<b>6. Interpretation, Combination and Integration.....</b>	<b>89</b>
6.1 Interpretation of Refraction Tomography Result.....	89
6.2 Combining $V_p$ , $V_s$ , $V_p/V_s$ with Borehole Logs and Previous VSP Results.....	90
6.2.1 $V_p$ , $V_s$ and $V_p/V_s$ versus Lithology.....	90
6.2.2 Comparing with Previous VSP Results.....	97
6.3 Description of other Geophysical Results in the Study Area.....	99
6.4 An Integrated Interpretation of the Geophysical Results.....	103
<b>7. Conclusion.....</b>	<b>111</b>
<b>References.....</b>	<b>114</b>

**Curriculum Vitae**

# List of Figures

<b>Figure 2.1</b> .....	4
Location map of the study area.	
<b>Figure 2.2</b> .....	5
The base of Quaternary deposits (Scheer et al., 2006).	
<b>Figure 2.3</b> .....	6
Geological cross section of the area. Black line represents base of Quaternary deposits (Scheer, 2001).	
<b>Figure 2.4</b> .....	8
The available boreholes in the study area with their lithological description. Borehole -1 and Borehole-2 (Grube, 2007), Tangstedt -3914 (Scheer, 2001).	
<b>Figure 3.1</b> .....	9
Schematic diagram showing a poroelastic medium.	
<b>Figure 3.2</b> .....	14
Travel paths for different velocity definitions: source $S_0$ and red rays shall demonstrate vertical incidence (zero-offset) and recording in the borehole and thus defining average velocity and interval velocity. Blue source and rays demonstrate CMP (common midpoint) raypaths for horizontal layering and shall define stacking velocity and rms velocity.	
<b>Figure 3.3</b> .....	17
Velocity depth model and calculated rms and average velocity as well as recalculated interval velocity by Dix formula (equation (3.21)). Black: given $V$ interval, blue: calculated $V$ average, red: calculated $V_{rms}$ , blue dash dot: $V_i$ (calculated by Dix formula from $V_{average}$ ) dot: $V_i$ (calculated by Dix formula from $V_{rms}$ ).	
<b>Figure 3.4</b> .....	19
Plot of laboratory measured P- and S-wave velocity $V_p$ and $V_s$ versus pressure $P_d$ for two water-saturated sands with different grain sizes, open circle fine grained and solid circles for coarse grained (from Prasad & Meissner, 1992).	
<b>Figure 3.5</b> .....	20
Schematic diagram of a VSP survey (from DiSiena et al., 1984).	

<b>Figure 3.6</b> .....	21
(a) P-wave VSP data (Z-component) with the first break picks. (b) The average and interval velocity in m/s (Rumpel et al., 2005a).	
<b>Figure 3.7</b> .....	22
Sonic logging, (a) Borehole-compensated sonde; (b) $\gamma$ -ray (left) and P-wave velocity log (right).	
<b>Figure 3.8</b> .....	23
Surface seismic technique; (a) raypaths for two layer medium; (b) travelttime curves; (c) sample seismogram from the survey area with the direct, refracted and reflected arrivals.	
<b>Figure 3.9</b> .....	26
Summary of the effect of different rock properties on the seismic P- and S-wave velocities and the velocity ratio $V_p/V_s$ . Various rock properties are listed across the top of the figure, while the velocities and the velocity ratio are on successive rows. SS-Sand Stone, LS-Lime Stone and DO-Dolomite (Tatham & McCormack, 1991).	
<b>Figure 4.1</b> .....	28
Geometry of reflected wave paths for a horizontal interface.	
<b>Figure 4.2</b> .....	30
Ray path and travelttime diagram for a dipping reflector.	
<b>Figure 4.3</b> .....	32
Demonstration of lateral resolution depending on the radius of the first Fresnelzone.	
<b>Figure 4.4</b> .....	32
Demonstration of vertical resolution depending on velocity and frequency.	
<b>Figure 4.5</b> .....	33
Vibrators (a) photo vibrator (LIAG Vibrator) (b) basic principles.	
<b>Figure 4.6</b> .....	34
Steps in vibroseis sweep correlation.	
<b>Figure 4.7</b> .....	35
Sample of a shallow P-wave shot gather at the beginning of the profile (a) uncorrelated vibroseis data (b) Sweep signal (c) Correlated data.	

<b>Figure 4.8</b> .....	36
Landstreamer (a) Main parts of LIAG landstreamer (b) Photo of landstreamer.	
<b>Figure 4.9</b> .....	36
Principle of the common midpoint over a horizontal interface.	
<b>Figure 4.10</b> .....	37
Simple schematic diagram of the main seismic reflection processing steps for a CMP gather.	
<b>Figure 4.11</b> .....	38
Shallow P-wave shot gather record from the study area; raw data which displays surface related noises (guided, refracted and air waves).	
<b>Figure 4.12</b> .....	38
Single shot gather. (a) Scaled raw data (AGC, 100ms). (b) After application of a band pass filter (40-60-400-440 Hz). (c) After mute applied.	
<b>Figure 4.13</b> .....	40
Velocity analysis; CMP gather and its velocity spectrum with the picked velocities, and the CMP gather after correction.	
<b>Figure 4.14</b> .....	41
Migration principle: the reflection segment AB moves to segment A'B' when migrated.	
<b>Figure 4.15</b> .....	46
(a) Finite-difference mesh centred about source point A, where $B_i$ and $C_i$ for $i = 1,2,3,4$ are to be timed. (b) The expanding square method (Vidale, 1988). Point A is the source point and the point shown as filled circles are about to be timed. The traveltimes at open circles are known (from Qin et al., 1992).	
<b>Figure 4.16</b> .....	47
Typical computational steps in seismic refraction tomography: (a) Observational basis: Refraction travel time curves $\tau_{\text{obs}}$ for overlapping spreads and a dense sequence of source points, (b) computation of simplified average travel time-distance curve $\tau_{\text{mean}}$ , (c) derivation of a one-dimensional starting model $v(0)$ based on b), (d) computation of simulated travel-time curves $\tau_{\text{sim}}$ for the actual model, (e) computation of rays for the actual model, (f) determination of traveltme residuals	

$\Delta\tau = \tau_{\text{obs}} - \tau_{\text{sim}}$  (and checking of data fit), (g) application of an inversion technique to convert travel-time residuals  $\Delta\tau$  into corrections  $\delta v$  of the actual velocity model, (h) updating of the actual velocity model  $v(1) = v(0) + \delta v$ , or more generally,  $v(n+1) = v(n) + \delta v$  for the next iteration starting again with d) (Rabbel, 2006).

<b>Figure 4.17</b> .....	48
A diagram showing P-, SV-, and SH-waves in the X, Y, Z coordinates.	
<b>Figure 4.18</b> .....	50
S-wave Vibrator. (a) Photo of electro-dynamic S-wave vibrator (ELViS 4). (b) The main parts of LIAG S-wave vibrator.	
<b>Figure 4.19</b> .....	51
S-wave traces, (a) right shot, (b) left shot, (c) subtraction of the two shots.	
<b>Figure 4.20</b> .....	52
Two-way travel times ( $t_o$ ) and NMO-times ( $\Delta t$ ) of a P- and S-wave reflection from the same horizon, where $V_p = 2V_s$ .	
<b>Figure 5.1</b> .....	55
Profile map and CMP location of the survey area, profile 1 from the 2005 campaign and profile 2 from the 2006 campaign (for details of profile 2 see also Figure 5.15).	
<b>Figure 5.2</b> .....	59
Stacked depth section profile Tangstedt P-wave 2005, (Rumpel et al., 2005b).	
<b>Figure 5.3</b> .....	60
Shot gather with the picked first arrivals (red line).	
<b>Figure 5.4</b> .....	60
Starting interval velocity model.	
<b>Figure 5.5</b> .....	61
The picked (blue) and the predicted (red) travel times.	
<b>Figure 5.6</b> .....	62
Velocity field obtained from the tomography inversion. Pink line is the elevation. Figure (a) shows the 4 m misfit between elevation and the tomography result. The reason for this discrepancy is unclear; may be it is due to the mathematical calculation in the software. Figure (b) shows the situation after the shift was made to the tomography result in order to correct this 4 m difference.	

<b>Figure 5.7</b> .....	62
Ray density from the tomographic inversion.	
<b>Figure 5.8</b> .....	63
The input velocity model for producing a synthetic seismogram.	
<b>Figure 5.9</b> .....	64
Sample synthetic traces with the first break picks (minimum phase wavelet).	
<b>Figure 5.10</b> .....	64
Starting interval velocity model for first test data set.	
<b>Figure 5.11</b> .....	65
Velocity field from tomographic inversion of data set one.	
<b>Figure 5.12</b> .....	65
Ray density from the tomographic inversion of data set one.	
<b>Figure 5.13</b> .....	65
Starting model from turning ray velocity for the second test data set.	
<b>Figure 5.14</b> .....	66
Velocity field from tomographic inversion of data set two.	
<b>Figure 5.15</b> .....	66
Ray density from the tomographic inversion of data set two.	
<b>Figure 5.16</b> .....	67
Profile map and CMP location of the 2006 survey area (profile 2) and the corresponding CMP from profile 1 (profile Tangstedt 2005).	
<b>Figure 5.17</b> .....	68
Field survey layouts for the acquisition of the data. A land streamer consisting of 72 geophones with 1 m separation was used for recording the data with offset-shot.	
<b>Figure 5.18</b> .....	70
Frequency content of a reflection shot gather.	
<b>Figure 5.19</b> .....	71
Raw shot gather and amplitude spectra for the marked region; (a) for reflections between 50 and 100 ms the dominant frequency is 50 to 300 Hz; (b) for reflections between 150 and 200 ms the dominant frequency is 80 to 300 Hz.	

<b>Figure 5.20</b> .....	72
A single shot gather offset from 22.96 to 94.75 m, (a) scaled (AGC, 100ms), (b) after static correction (c) after deconvolution and application of a bandpass filter (d) after mute applied (depth scale changed).	
<b>Figure 5.21</b> .....	73
Velocity spectrum with the picked velocities at different CMP points.	
<b>Figure 5.22</b> .....	74
Stacking velocity field from the velocity analysis of CMP gather.	
<b>Figure 5.23</b> .....	74
CMP time stacked section to reference elevation (20 m NN). The arrows point to the major reflectors.	
<b>Figure 5.24</b> .....	75
Stacked (a) migrated time section, (b) depth section (reference elevation (20 m NN)). The arrows point to the major reflectors.	
<b>Figure 5.25</b> .....	76
Field survey layouts for the acquisition of the data. A land streamer consisting of 72 geophones with 1 m separation used for recording the data with a combination of end-on and split-spread shot.	
<b>Figure 5.26</b> .....	78
One sample shot gather, summed and correlated data with AGC (300 ms).	
<b>Figure 5.27</b> .....	79
Shot gather with zero-phase Ormsby band-pass filter, trace equalization (50 ms time gate) and AGC (300 ms) applied. (a) 60-70-180-195 bandpass, (b) 20-30-80-195 bandpass and (c) 40-50-180-195 bandpass.	
<b>Figure 5.28</b> .....	80
Velocity spectra, picks and CMP supergather before (left) and after (right) NMO correction.	
<b>Figure 5.29</b> .....	81
Stacking velocity field from the velocity analysis of several CMP gathers.	
<b>Figure 5.30:</b> .....	81
Stacked Time Section, the arrows point to the major reflectors.	



<b>Figure 5.31</b> .....	82
Stacked (a) migrated time section, (b) depth section (the arrows point to depth of reflectors as discussed in the text).	
<b>Figure 5.32</b> .....	83
Raw shot gather (a) P-wave with AGC (100 ms), (b) S-wave with AGC (300ms).	
<b>Figure 5.33</b> .....	84
Example of P-wave (a) and S-wave (b) prestack processed shot gather. The P-wave records are filtered with a 40-60-400-440 Hz frequency bandpass filter and the S-wave records with a 30-40-180-195 Hz bandpass frequency filter.	
<b>Figure 5.34</b> .....	85
Depth section for 100 m depth. (a) S-wave section, (b) P-wave section.	
<b>Figure 5.35</b> .....	86
Part of P-wave (left) and S-wave (right) time section from CDP 1200 to 1300. The coloured lines indicate reflections from the same horizons.	
<b>Figure 5.36</b> .....	87
P-wave refraction tomographic velocity field rescaled for the same surface locations as the shallow P-wave reflection depth section in Figure 5.37.	
<b>Figure 5.37</b> .....	87
Shallow P-wave depth section with the interval velocity field.	
<b>Figure 5.38</b> .....	88
Shallow P-wave depth section with the refraction tomography velocity field.	
<b>Figure 6.1</b> .....	89
P-wave interval velocity model from the tomography inversion and the available boreholes (B1 (at 600 m), B2 (at 2200 m) and Tangstedt 3914 (at 2800 m)).	
<b>Figure 6.2</b> .....	91
(a) P-wave interval velocity, $V_p$ , (b) S-wave interval velocity, $V_s$ , (c) P- to S-wave velocity ratio, $V_p/V_s$ , for depth down to 65 m respectively.	

<b>Figure 6.3</b> .....	94
Plots of average P- to S-wave velocity ratio, $V_p/V_s$ for the entire profile taken every 100 CMPs for a depth down to 65 m with lithology profiles from the nearest borehole logs: Tangstedt-B2 (depth 20 m) and Tangstedt-3914(only 80 m depth displayed).	
<b>Figure 6.4</b> .....	96
Plots of (a) P-wave velocity, (b) S-wave velocity, (c) P- to S-wave velocity ratio versus depth at CMP 150 and lithology log for the nearest borehole to CMP 150.	
<b>Figure 6.5</b> .....	96
Plots of (a) P-wave velocity, (b) S-wave velocity, (c) P- to S-wave velocity ratio versus depth at CMP 1300 and lithology log for the nearest borehole to CMP 1300.	
<b>Figure 6.6</b> .....	98
$V_p$ and $V_s$ interval velocities and $V_p$ to $V_s$ velocity ratios for the shallow surface seismic data at CMP 1300 (a, c & e) and from VSP results in borehole Tangstedt-3914 (b, d & f) (Rumpel et al., 2005a).	
<b>Figure 6.7</b> .....	99
Profile map of seismic, GPR, SIP, VES and AEM lines and Borehole-2 in the survey area Tangstedt.	
<b>Figure 6.8</b> .....	100
The GPR profiles L01-L04 collected with 100 MHz. The cyan lines mark a dipping reflection that can be recognized in all GPR profiles (Møller, 2006).	
<b>Figure 6.9</b> .....	102
AEM resistivity cross-section along the flightline (profile number 258.1) close to the seismic profile Tangstedt (Siemon et al., 2006), blue box corresponds to Tangstedt P-wave profile 2005 and red box corresponds to Tangstedt shallow P- and S-wave profile 2006.	
<b>Figure 6.10</b> .....	103
Inversion result along a profile at the Hasloh test site (Figure 6.7) for frequency of 1.25 Hz. Left panel: Resistivity magnitude, right panel: resistivity phase shift (Hoerdt et al., 2007).	

<b>Figure 6.11</b> .....	104
(a) Shallow S-wave reflection (720 m long) (b) GPR section (400 m long) with interpretation (Møller, 2006) (c) SIP (84 m long) interpreted result (Hoerdt et al., 2007).	
<b>Figure 6.12</b> .....	105
The GPR profile (the cyan line indicates the reflection) (Møller, 2006), the SIP resistivity section (Hoerdt et al., 2007) and the nearby borehole B2 superimposed on Part of the S-wave reflection depth section.	
<b>Figure 6.13</b> .....	107
(a) Shallow P-wave reflection depth section with the interval velocities. (b) Refraction tomography velocity model. (c) AEM resistivity cross-section (Siemon et al., 2006). Part of the AEM and refraction tomography profile that overlap the SPR profile is displayed here as well as the nearby lithology logs from borehole B1 (at 75 m) and Tangstedt-3914 (at 600 m).	
<b>Figure 6.14</b> .....	108
The shallowest refraction tomography boundary (~10 m, red dotted line), AEM resistivity cross-section and the lithologic log from borehole B2 (at 75 m) and Tangstedt-3914 (at 600 m) are inserted in the P-wave reflections depth section.	
<b>Figure 6.15</b> .....	110
Near-surface geologic model of the study area based on the seismic data, other geophysical data and the borehole information. Values of shallow P-wave reflection interval velocities ( $V_p$ ), P-wave refraction tomography velocities ( $V_{pref}$ ), shallow S-wave interval velocities ( $V_s$ ) and resistivities from AEM are shown for each layer.	

# List of Tables

<b>Table 3.1</b> .....	24
A list of typical P-wave and S-wave velocities of various rock types from (Jaeger et.al., 2007) and (Todd, 1980).	
<b>Table 3.2</b> .....	24
Typical $V_p/V_s$ values for sedimentary rocks (Domenico, 1984).	
<b>Table 5.1</b> .....	56
Acquisition Parameters for 2005 and 2006 data. The sum of the geophone number (PG) and the vibration point number (VP) gives the CMP point number. The location of PG or VP is at CMP/2.	
<b>Table 5.2</b> .....	57
Acquisition Parameters profile Tangstedt P-wave 2005 (Rumpel et al., 2005b).	
<b>Table 5.3</b> .....	58
Processing flow profile Tangstedt P-wave 2005 (Rumpel et al., 2005b).	
<b>Table 5.4</b> .....	69
Shallow P-wave acquisition parameter, profile Tangstedt 2006.	
<b>Table 5.5</b> .....	69
Data processing sequences, profile Tangstedt 2006.	
<b>Table 5.6</b> .....	77
Shallow S-wave acquisition parameters, profile Tangstedt 2006.	
<b>Table 5.7</b> .....	78
S-wave data processing sequences, profile Tangstedt 2006.	
<b>Table 6.1</b> .....	92
$V_p$ , $V_s$ and $V_p$ to $V_s$ ratio along the shallow P- and S-wave reflection profile (Figure 5.16) for the depth range 0 to 65 m, every 100 CMPs.	
<b>Table 6.2</b> .....	95
$V_p$ , $V_s$ and $V_p/V_s$ values (a) at CMP 150, (b) at CMP 1300.	
<b>Table 6.3</b> .....	109
Summary of the interpreted results from GPR, SSR, SIP, SPR, AEM and refraction tomography. For all methods except AEM the interpretation is based on the two nearby boreholes: B2 and Tangstedt-3914. AEM interpretation is based on the colour code definition from BurVal working report (Scheer et al., 2006).	

# 1. Introduction

The near-surface of the earth is diverse and a complex terrestrial environment that supports human infrastructure, provides water and mineral resources, and is the region in which human activities have considerable impact. Hence developing an understanding of the processes and properties that occur here is essential for utilizing it efficiently and properly (e.g. Butler, 2005). Therefore suitable geophysical methods (Steeple, 2005) must be used for exploring the resources, for the characterization of contaminated sites, for groundwater quality evaluation, cavity and tunnel detection, the assessment and design of built infrastructure, and to address scientific questions in this dynamic part of the earth. As a result rapid, accurate and cost effective mapping of the lithology, structure and physical properties of the near-surface of the earth is crucial.

Lithology is a description of rocks (especially sedimentary rocks), which is identified by the composition and microstructure of the rocks. As many measurable physical and other properties of rocks vary strongly with lithology, being able to relate these properties of rocks as a function of lithology is very important. Lithology of rocks is traditionally obtained on the basis of hand specimens and outcrops (e.g. Jenn et al., 2007). An alternative is the use of boreholes, another is the use of surface geophysical measurements. One example is the use of surface seismic data for estimation of lithology. To interpret the lithologic information inherent in seismic wave velocities requires an understanding of the relationship between geology and velocity. To this end, this work is interested in studying the competence of seismic parameters to lithology predictions.

For correct prediction of the lithology from seismic data accurate near-surface velocity information is mandatory. In this study, first arrival refraction tomography and high resolution P- and S-wave reflection methods are applied for near-surface lithological classification based on seismic velocity analysis in sedimentary environment.

First arrival refraction tomographic imaging technique is proposed for constructing a near-surface P-wave velocity model from refraction events of standard reflection data. First arrival refraction tomography, unlike conventional seismic refraction and seismic reflection method uses diving waves. In this approach the medium was parameterized as a number of cells, diving rays were traced through the model, and traveltimes residuals were inverted for slowness perturbations in every cell crossed by rays (Rawlinson & Sambridge, 2003). Since diving waves are expected to

fit the nonlinear moveout of first arrivals better than head waves, broader offset ranges needed to be included for processing.

High resolution seismic reflection techniques measure the velocity and depth of different velocity layers for acquiring a rather detailed picture of the very near-surface of the earth. They are used for the delineation and mapping of small-scale features at shallow depths that cannot be imaged by standard reflection methods. Imaging of such shallow depths demands generating and transmitting of high frequency broad bandwidth signals and small receiver intervals (Steeple & Miller, 1998). This in turn requires capable equipments.

The combined analysis of high resolution seismic P- and S-wave velocity information has advantage for identifying near-surface lithologies over using solely the P- or S-wave information. Since different modes of P- and S-waves travel at different speeds through the earth they respond differently to various geological situations. In addition, S-waves have a potential to provide improved resolution because of their shorter wavelengths. Most importantly the information from P- and S- wave velocities allows predicting lithology also via analysis of  $V_p$  to  $V_s$  ratio.

This dissertation is separated into seven chapters. In Chapter 2 a brief description of the location and geology of the study area is presented.

Chapter 3 recounts the propagation of seismic waves in poroelastic medium. The poroelasticity theory, which considers the solid-to-fluid and fluid-to-solid coupling in porous material and their governing equations are described. Next, the propagation velocities of P- and S-waves, the diverse velocity definition in exploration seismology, the different ways to determine seismic wave velocities and the factors controlling seismic wave velocities are dealt.

Chapter 4 gives an overview of the near-surface seismic methods. The basics of the shallow P- and S-wave reflection method are described. This includes instrumentation, acquisition and processing. Some basic concepts of first arrival refraction tomography followed by the introduction of the two inversion methods: two-point ray tracing and a wavefront construction method are given.

Chapter 5 focuses on the acquisition, processing and results of the P-wave refraction tomography and the shallow P- and S-wave reflection data. In the refraction tomography processing a simple synthetic test is demonstrated in order to show the effect of the acquisition geometry on the

resulting velocity field. Besides, a comparison between the P-wave refraction tomography versus the shallow P-wave velocity model, and the shallow P- and S-wave seismic section are made.

Chapter 6 reviews the interpretation results in the study area. This chapter also describes  $V_p$ ,  $V_s$  and  $V_p$  to  $V_s$  ratio from the shallow P- and S-wave reflection and their correlation with the borehole logs and the previously obtained VSP results. In the end the results from the seismic methods are integrated into the available geophysical data and the lithologic log.

Finally I conclude the thesis in Chapter 7 with the summary of the findings of this work.

## 2. Regional Setting

### 2.1 Location

The study area is one of the BurVal (EU INTERREG project on buried valley aquifers) pilot project areas called Ellerbeker Rinne (Scheer et al., 2006). It is situated some 10 km Northwest of Hamburg (Figure 2.1) in a typical Quaternary environment with sand and till on the surface (Ehlers, 1996). It extends from Tangstedt to Hasloh. The landscape form of the area is flat and wavy. The elevation rises up to 20 m above sea level in the area. It belongs to the north European sedimentation basin like other parts of Northern Germany. The subglacial valley (Ellerbeker Rinne) is a significant feature in the area and a good groundwater reservoir.

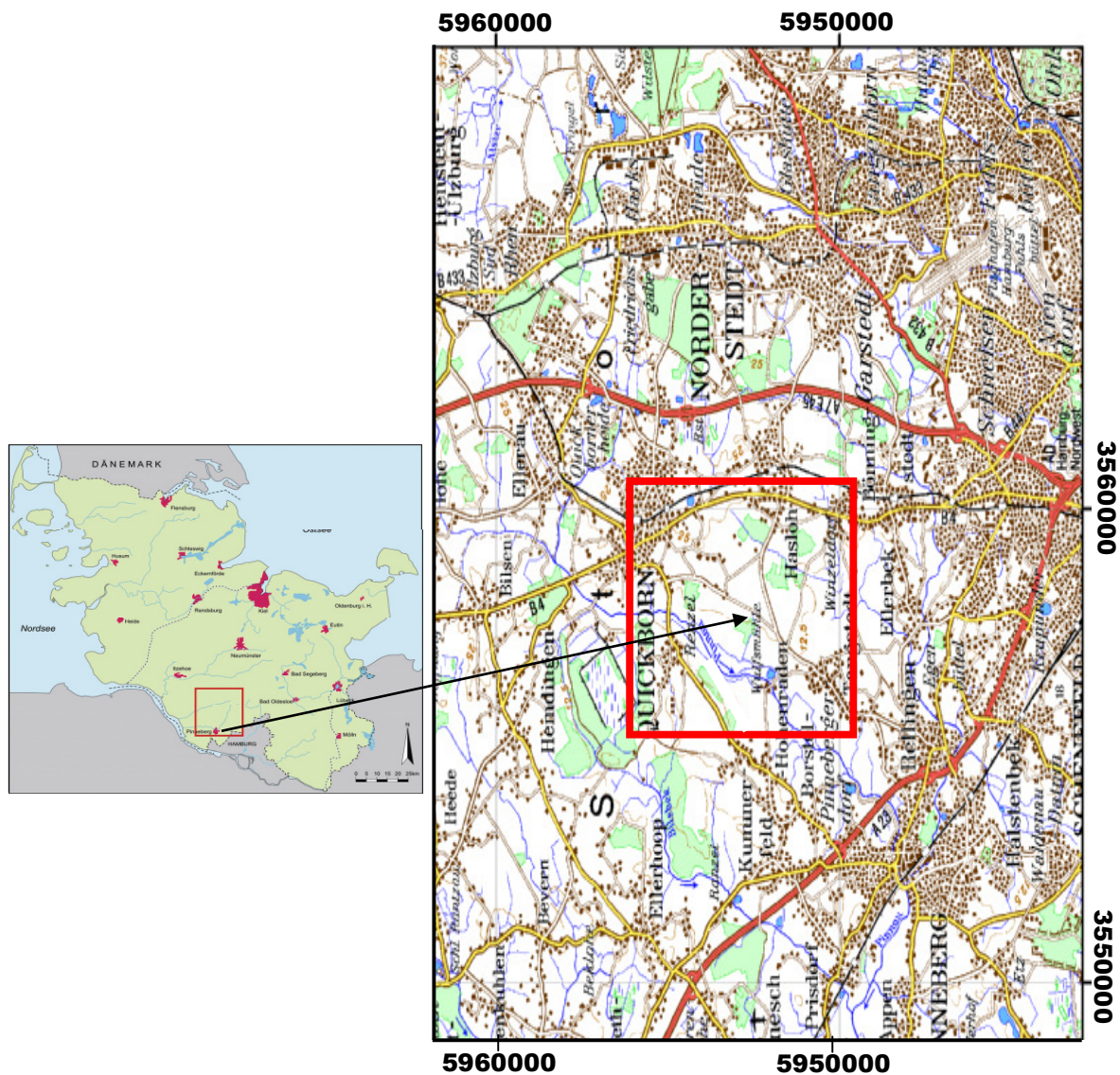


Figure 2.1: Location map of the study area.



## 2.2 Geology

The geology of the area is characterized by a thick sequence of sedimentary deposits and updoming salt structures. Mainly in the Permian age thick deposits of salt rocks had been formed which were the source of numerous rising salt structures that strongly influenced the sedimentation and stratification of the younger overlaying strata. These salt structures affect the structure of the covering sediments: some penetrate the near-surface sediments and some of them even reach the surface. The young Tertiary and the Quaternary sediments are area of concern for this study in the near-surface area.

Quaternary sediments in northern Germany are mainly characterized by glacial activity during the Pleistocene. The near-surface Quaternary sediments are formed mainly from glacial tills and sandy material of outwash plains of the Saalian age. They have a heterogeneous distribution because of rapidly varying conditions of sedimentation and erosion. Geological information from wells indicates that the thickness of the Quaternary sequence (Figure 2.2) normally varies from 20 to 60 m. But may reach more than 400 m in buried valleys (Figure 2.2); this is confirmed by geophysical investigations (e.g. Gabriel et al., 2003).

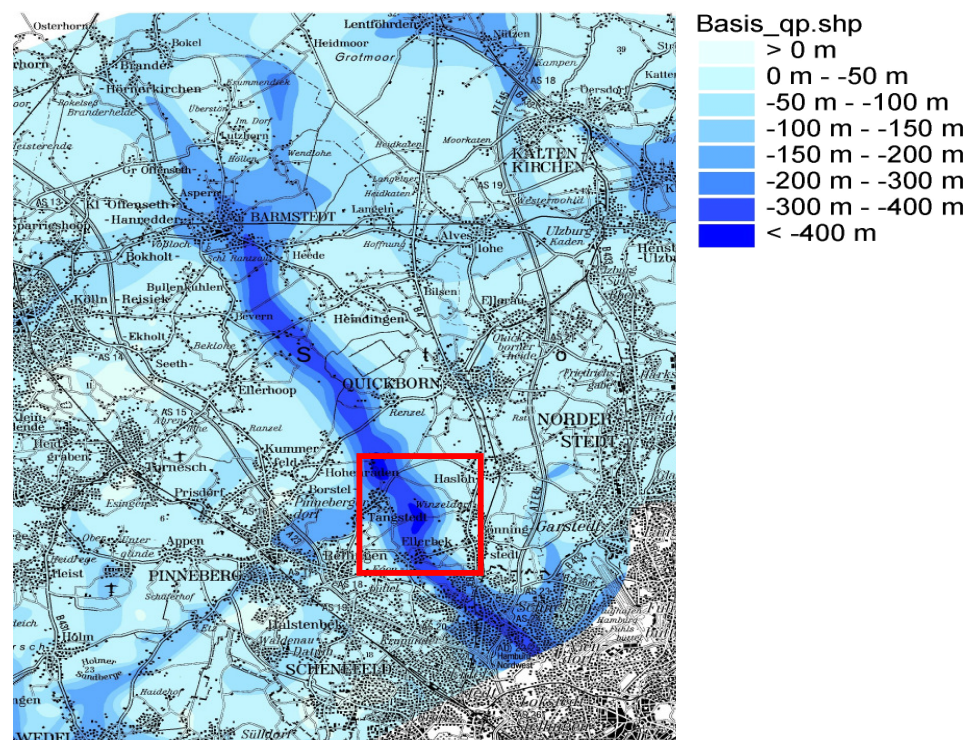


**Figure 2.2:** The base of Quaternary deposits (Scheer et al., 2006).

The origin of most Tertiary sediments is the Scandinavian Shield, from where large river systems transported huge amounts of material into the basin of the ancient North Sea. Several lateral movements of the shore line caused cycles of sedimentation with an accumulation of fine grained marine sediments. The deposits of the younger Tertiary include a fairly uniform series of powerful clay and sand horizons (Figure 2.3).

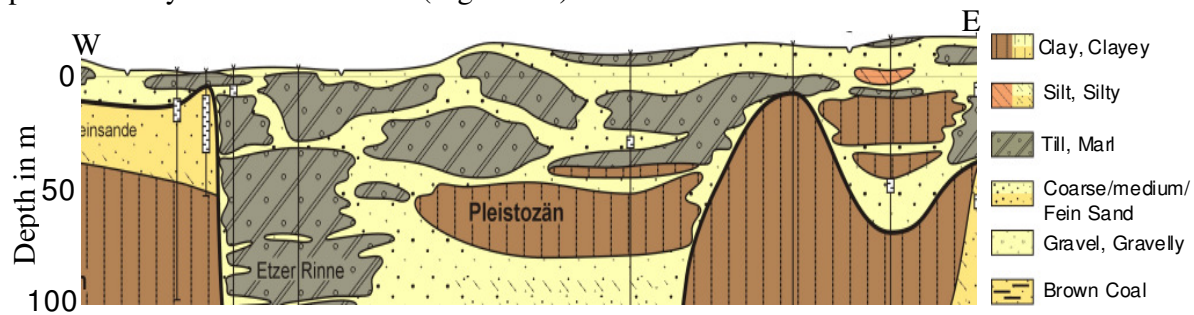


**Figure 2.3:** Geological cross section of the area. Black line represents base of Quaternary deposits (Scheer, 2001).

The near-surface aquifer system in the area is built up by medium to coarse-grained glaciofluvial sands of mostly Saalian age. These near-surface aquifers are covered with discontinuous glacial till and clay layers. The thickness of these aquifers as well as the covering glacial tills and clay layers varies strongly. Thus, the potential for ground water extraction from the near-surface aquifers is also strongly varying (Scheer et al., 2006). Since the covering clay layers are discontinuous the aquifers can be exposed to contamination and pollution. A more detailed description of the geology of the area can be found in the final report of the BurVal working group 2006 (Scheer et al., 2006).

Three boreholes (Borehole 1 (B1), Borehole 2 (B2) and Tangstedt-3914) with qualitative lithologic descriptions are available in the area. They mostly indicate a layered geology composed of sedimentary material with mineral compositions varying between till, clay and sand (Figure 2.4).

Borehole 1 was drilled to a depth of 119 meters. The first lithological unit encountered is approximately 20 meters thick and is composed of a mixture of humus and fluvial sediments that include fine, medium to coarse sand, silt, gravel and till. Beneath these heterogeneous units, between 20 and 65 m a clean layer of sand is present. At depth approximately 65 m a dark brown to black, silty and slightly calcareous 10 m thick Lauenburger clay is found. Below this unit alternate layers of sand and clay material are deposited.

Borehole 2 was drilled to a depth of 20 meters and three major lithological differences can be identified. These include an around 3 m thick mixture of humus, sand, silt, gravel and till; a complete sand unit and a gray till unit between 17-20 m.

Tangstedt 3914 was drilled to a depth of 252 m. A 10 m thick sandy and gravelly till layer is the uppermost lithological unit for this borehole. Below this unit 14 m thick fine to medium sand is present. The till below this interval is 46 m thick. A silt-clay layer is present between a depth of 70 and 113 m. Below this layer are fine, medium to coarse silty sand layers which contain a thin clay layer between 63 to 76 m and layers of brown coal.

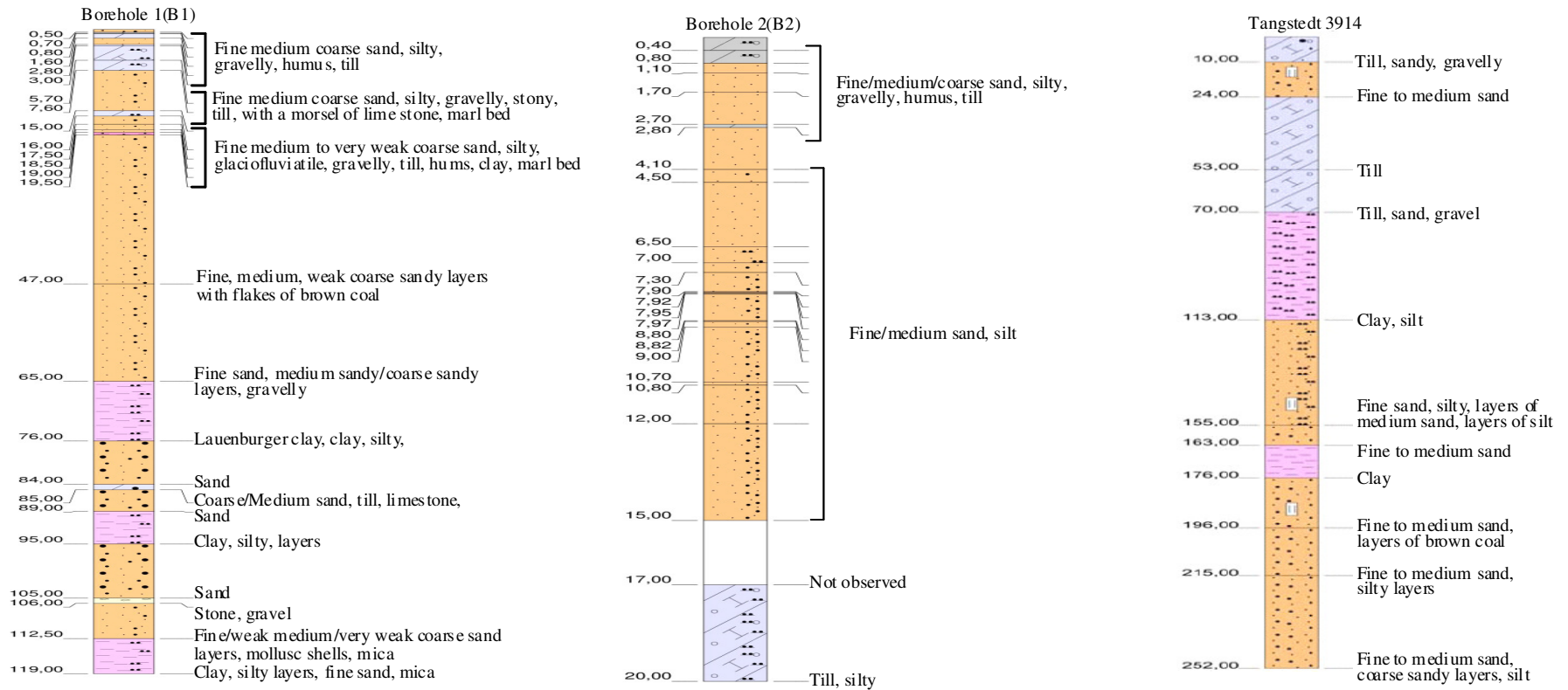


**Figure 2.4:** The available boreholes in the study area with their lithological description. Borehole -1 and Borehole-2 (Grube, 2007), Tangstedt -3914 (Scheer, 2001).

### 3. Seismic Waves

A wave is a disturbance, usually periodic, that travels with finite velocity through a medium. All wave motions have two important characteristics in common: First, energy is propagated to distant points and, second, the disturbance travels through the medium without giving the medium as a whole any permanent displacement. Waves travelling through rock governed by the laws of linear elasticity are known as seismic waves. Seismic waves are generated at a source which can be natural, such as an earthquake, or artificial, such as an explosion. The resulting waves propagate through the medium, some portion of the earth, and may be recorded at a receiver, which gives information about both the source of the waves and the material they pass through. Seismic waves originating from earthquakes are used to locate earthquake foci and to study the mechanism at the source (Aki & Richards, 1980). Seismic waves from man-made sources are used to study the near-surface structure of the earth, to locate mineral deposits (including hydrocarbons, ores, water, geothermal reservoirs, etc), archaeological sites, and to obtain geological information for engineering (Sheriff & Geldart, 1995). In the following section the propagation of seismic waves in natural rocks is discussed in detail.

#### 3.1 Seismic Waves in Natural Rocks

For a wide range of fluid-filled porous solids the elastic theory is a crude approximation for investigating wave propagation in such media. Due to the porosity of natural rocks and due to the interaction of the skeleton and the pore content, a different theoretical approach, i.e., poroelastic theory is necessary to explain various observed effects. The theory of poroelasticity that applies to most rock materials can be constructed by the idealization of a rock as a connected mineral phase permeated with voids; these voids may be interconnected (Figure 3.1).

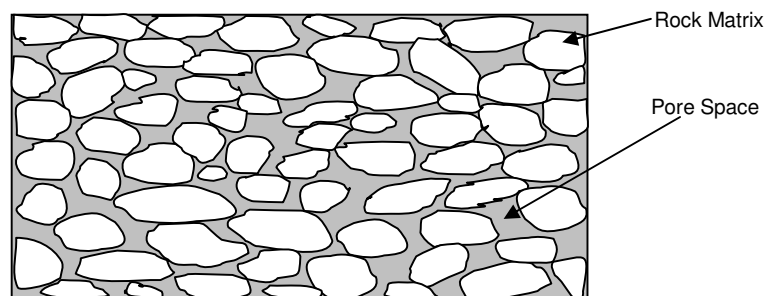


**Figure 3.1:** Schematic diagram showing a poroelastic medium

The Biot theory (Biot, 1956a,b, 1962) is used to describe the seismic wave propagation in such a medium. According to this theory, a fluid-filled porous rock is regarded as an interacting two-phase elastic system, one phase of which is the porous rock matrix and the other phase is a fluid filling the voids. The interaction between the fluid phase and the bulk material during wave propagation influences the amplitude and the phase of seismic waves significantly. Furthermore these interactions cause energy dissipation, resulting in attenuation and velocity dispersion (Mavko & Nur, 1995). A thorough discussion and definitions of poroelasticity theory can be found in many books and publications such as Garg et al (1974), Antes & Wiebe (1996), Mavko et al. (1998), Wang (2000), and Schanz (2001).

Wave propagation problems in linear elastic porous media can be described by the equation of motion based on the constitutive law and of Biot's theory. In poroelasticity theory, there are two types of equations that are coupled. These are the equations for elastic behaviour of the solid rock and the equations for elastic and fluid flow behaviour of the pore fluid. This behaviour of a linear elastic, fluid saturated medium can be illustrated by the elastic Lamés constant  $\lambda$  and  $\mu$  and two special poroelastic constitutive coefficients R and Q (Biot, 1956a):

$$\lambda = \frac{2\nu\mu}{1-2\nu} \quad (3.1)$$

$$R = \mu\Phi^2 B^2 \frac{2(1-2\nu)(1+\nu_u)^2}{9(1-2\nu_u)(\nu_u-\nu)} \quad (3.2)$$

$$Q = -R + \mu\Phi B \frac{2(1+\nu_u)}{3(1-2\nu_u)} \quad (3.3)$$

Herein,  $\nu_u$  is the undrained Poisson's ratio, and B is the Skempton pore pressure coefficient (Skempton, 1954). The shear modulus  $\mu$ , the elastic Poisson's ratio  $\nu$  (under drained conditions; see e.g. Wang, 2000), and the porosity  $\Phi$  are well known material constants in soil mechanics and can be measured using conventional laboratory measurements.

Using the above equations, the stress-strain relations for a linear elastic fluid saturated porous medium can be given by

$$\sigma_{ij}^s = 2\mu\varepsilon_{ij}^s + \left(\lambda + \frac{Q^2}{R}\right)\delta_{ij}\varepsilon_{kk}^s + Q\delta_{ij}\varepsilon_{kk}^f \quad (3.4)$$

$$\sigma^f = Q\varepsilon_{ii}^s + R\varepsilon_{ii}^f \quad (3.5)$$

where  $\sigma_{ij}^s$  and  $\sigma^f$  are the stresses, and  $\varepsilon_{ij}^s$ ,  $\varepsilon_{kk}^f$  are the corresponding elastic strain and fluid dilatation, which act on the elastic and fluid parts, respectively.

The total stress is defined as

$$\sigma_{ij} = \sigma_{ij}^s + \delta_{ij}\sigma^f . \quad (3.6)$$

The fluid pore pressure  $P$  is related to the fluid stress  $\sigma^f$  via the porosity  $\Phi$ :

$$P = -\frac{\sigma^f}{\Phi} . \quad (3.7)$$

Using the linear strain-displacement relation, the governing equations of motions for dynamic poroelastic media are (from Antes & Wiebe, 1996)

$$\frac{\partial \sigma_{ij}^s}{\partial x_j} - b\left(\frac{\partial u_i^s}{\partial t} - \frac{\partial u_i^f}{\partial t}\right) + F_i^s = \rho_{11}\frac{\partial^2 u_i^s}{\partial t^2} + \rho_{12}\frac{\partial^2 u_i^f}{\partial t^2} \quad (3.8)$$

$$\frac{\partial \sigma^f}{\partial x_i} + b\left(\frac{\partial u_i^s}{\partial t} - \frac{\partial u_i^f}{\partial t}\right) + F_i^f = \rho_{21}\frac{\partial^2 u_i^s}{\partial t^2} + \rho_{22}\frac{\partial^2 u_i^f}{\partial t^2} \quad (3.9)$$

They may be written with the constitutive equations (3.4) and (3.5) as

$$\left(\lambda + \mu + \frac{Q^2}{R}\right)\frac{\partial u_j^s}{\partial x_{ji}} + \mu\frac{\partial u_i^s}{\partial x_{ji}} + Q\frac{\partial u_i^f}{\partial x_{ji}} - b\left(\frac{\partial u_i^s}{\partial t} - \frac{\partial u_i^f}{\partial t}\right) + F_i^s = \rho_{11}\frac{\partial^2 u_i^s}{\partial t^2} + \rho_{12}\frac{\partial^2 u_i^f}{\partial t^2} \quad (3.10)$$

$$Q\frac{\partial u_j^s}{\partial x_{ji}} + R\frac{\partial u_j^f}{\partial x_{ji}} + b\left(\frac{\partial u_i^s}{\partial t} - \frac{\partial u_i^f}{\partial t}\right) + F_i^f = \rho_{21}\frac{\partial^2 u_i^s}{\partial t^2} + \rho_{22}\frac{\partial^2 u_i^f}{\partial t^2} \quad (3.11)$$

In these equations,  $u_s$  and  $u_f$  represent the solid and liquid displacements, respectively. The internal viscous friction that is caused by the relative movement between fluid and solid is

described by  $b$ .  $F_i^s$  and  $F_i^f$  are the solid and fluid body force vectors.  $\rho_{11}$  and  $\rho_{22}$  are the effective mass densities of the solid and the fluid, and  $\rho_{12} = \rho_{21}$  is a dynamic coupling parameter.

In the absence of pore fluid the equation of poroelasticity (3.10) reduces to that of elasticity:

$$(\lambda + \mu) \frac{\partial u_j^s}{\partial x_{ji}} + \mu \frac{\partial u_i^s}{\partial x_{jj}} + F_i^s = \rho_{11} \frac{\partial^2 u_i^s}{\partial t^2}. \quad (3.12)$$

Despite the fact that the above reduction disregards the fluid effect, it is a logical approximation and most seismic methods are satisfactorily based on the analysis of seismic wave propagation in a linear elastic medium.

### 3.2 P- and S-wave Velocities

There are different kinds of waves generated for seismic exploration. The two main types of body waves that travel through the interior of the earth are P-waves and S-waves. The propagation of P-waves through a medium is primarily governed by compressibility and rigidity, that of S-wave by rigidity, as well as by density and porosity in both cases. P-waves can travel through liquids, gases, as well as solids because the energy propagates through the atomic structure mainly by a series of compression and expansion (rarefaction) movements. S-waves, also called shear waves, require a mechanically solid material for effective propagation and, therefore, do not propagate in materials such as liquids or gases. Liquids and gases do not have any shear strength, i.e. there are no bonds holding the liquid and gas molecules together that will resist a shear force. In P-waves, the vibration of the rock is in the direction of propagation. In shear waves, particles oscillate perpendicular to the direction of wave propagation.

The velocity of propagation of P- and S- waves in a homogeneous isotropic elastic medium can be derived using the equation of motion and the relationship between stress and strain.

Equation (3.12) can be written in a vector form as (Tatham & McCormack, 1991)

$$\rho \frac{\partial^2 \psi}{\partial t^2} = (\lambda + 2\mu) \nabla(\nabla \cdot \psi) - \mu(\nabla \times \nabla \times \psi) \quad (3.13)$$

The above equation is commonly referred to as elastic (seismic) wave equation. We can separate the elastic wave equation into two wave equations, one for P-wave and one for S-wave, by taking the divergence and curl, respectively.



If we take the divergence, then

$$\frac{\partial^2 \nabla \cdot \psi}{\partial t^2} = \left( \frac{\lambda + 2\mu}{\rho} \right) \nabla^2 (\nabla \cdot \psi) \quad (3.14)$$

This is a wave equation for P-waves with a velocity

$$V_p = \left( \frac{\lambda + 2\mu}{\rho} \right)^{1/2} \quad (3.15)$$

The P-wave velocity can also be expressed in terms of the bulk modulus  $K$ , which is a measure of the substance's resistance to uniform compression. The following equation, relates the bulk modulus with the Lamé's constants

$$K = \frac{1}{3} (3\lambda + 2\mu) \quad (3.16)$$

Substituting in equation (3.15)  $V_p$  has the form

$$V_p = \left( \frac{K + 4/3 \mu}{\rho} \right)^{1/2} \quad (3.17)$$

Equation (3.17) shows that the P-wave velocity is a function of three separate properties of the material. It is primarily controlled by the bulk and the rigidity modulus of the material.

If we take the curl of equation (3.13), then

$$\frac{\partial^2 \nabla \times \psi}{\partial t^2} = \left( \frac{\mu}{\rho} \right) \nabla^2 (\nabla \times \psi) \quad (3.18)$$

This is a wave equation for S-waves with a velocity

$$V_s = \left( \frac{\mu}{\rho} \right)^{1/2} \quad (3.19)$$

Obviously, the S-wave velocity is determined by the shear modulus and the mass density of the medium. Its propagation velocity increases with the shear stiffness of the material.

### 3.3 Velocity Definitions

The different ways to quantify seismic velocities, e.g., direct measurements or indirect measurements, result in diverse velocity definitions. The exploration seismologist deals with interval, average, root-mean-square (rms), phase, group, normal moveout (NMO), stacking, or migration velocities. To avoid confusion the different meanings shall be illustrated in the following (after Hubral & Krey 1980, Yilmaz 2001, Sheriff 2002).

*The interval velocity* ( $V_i$ ) is the average velocity over some interval of travel path corresponding to  $t_i$  or thickness  $z_i$ . It is also often used for the average velocity calculated from sonic logs and then calculated from well surveys for the intervals between measurements (e.g., interval between geophones  $G_0$  and  $G_1$  as in Figure 3.2). Then

$$V_i = \frac{z_i}{t_i} \quad (3.20)$$

where,  $z$  is the thickness of an interval and  $\tau$  is the one-way travel time through it.

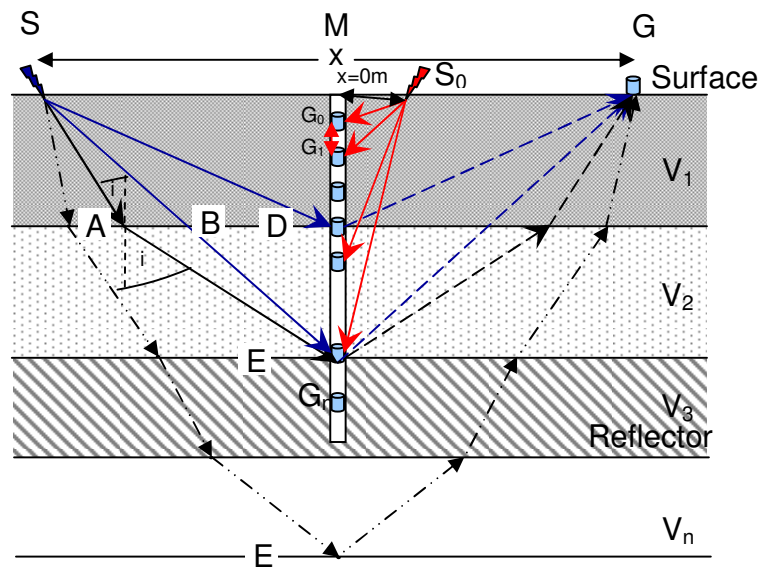


**Figure 3.2:** Travel paths for different velocity definitions: source  $S_0$  and red rays shall demonstrate near vertical incidence (zero-offset) and recording in the borehole and thus defining average velocity and interval velocity. Blue source and blue rays demonstrate CMP (common midpoint) raypaths for horizontal layering and shall define stacking velocity and rms velocity.

The term interval velocity (or Dix velocity) is also used for the velocity calculated for a vertical travel path between horizontal reflectors by Dix formula

$$V_i = \sqrt{\frac{V_n^2 t_n - V_{n-1}^2 t_{n-1}}{t_n - t_{n-1}}} \quad (3.21)$$

where  $V_n$  is the rms velocity (see below) and  $t_n$  is the zero-offset arrival time of the  $n^{\text{th}}$  reflection. This equation yields fictitious values if both reflectors are not horizontal, if there are lateral velocity variations between or above them, or if the interval is large.

**The average velocity** ( $\bar{V}$ ) is the ratio of the distance along a certain path to the time required for a wave to traverse the path, i.e.

$$\bar{V} = \frac{\int_0^t V(t) dt}{\int_0^t dt} \quad (3.22)$$

While it has meaning only with respect to a particular path, a vertical path is often implied, that is, it is given by a depth divided by the seismic traveltime to that depth, usually assuming straight raypath travel (e.g., rays from source  $S_0$  to geophones  $G_1$  to  $G_n$  in Figure 3.2). If the section is made up of parallel horizontal layers of velocity  $V_i$  and thickness  $z_i$  so that the traveltime across each layer is  $t_i = z_i/V_i$ , then the average velocity  $\bar{V}$  is

$$\bar{V} = \frac{\sum_i V_i t_i}{\sum_i t_i} = \frac{\sum_i z_i}{\sum_i (z_i/V_i)} \quad (3.23)$$

**The root-mean-square velocity** ( $V_{rms}$ ) down to a reflector (e.g., E in Figure 3.2) is defined as

$$V_{rms} = \sqrt{\frac{\sum_i V_i^2 t_i}{\sum_i t_i}} \quad (3.24)$$

**The NMO velocity** ( $V_{NMO}$ ) is the velocity for the normal-moveout correction (normal moveout is the difference between the two-way time at a given offset and the two-way zero-offset time). The traveltime equation as a function of offset is

$$t^2 = t_0^2 + \frac{x^2}{V^2} \quad (3.25)$$

where  $x$  is the distance (offset) between the source and the receiver positions (e.g., SG in Figure 3.2),  $V$  is the velocity of the medium above the reflecting interface, and  $t_0$  is twice the traveltime

along the vertical path MD (in Figure 3.2). For a single constant velocity horizontal layer, the reflection travelttime curve as a function of offset is a hyperbola. In the case of a dipping reflector the travelttime equation becomes a function also of the reflector dip angle. It still represents a hyperbola; however, the NMO velocity now is given by the medium velocity divided by the cosine of the dip angle. This means that the proper stacking of a dipping event requires a velocity that is greater than the velocity of the medium above the reflector.

For the multilayer case of a medium with horizontal iso-velocity layers the travelttime equation results in

$$t^2(x) = C_0 + C_1x^2 + C_2x^4 + C_3x^6 + \dots \quad (3.26)$$

where  $C_0=t_0^2$ ,  $C_1=1/v_{rms}^2$ , and  $C_2, C_3, \dots$  are complicated functions that depend on layer thicknesses and interval velocities; with interval velocities  $V_i$  and vertical two-way time  $t_i$  for the  $i^{th}$  layer. By making the small-spread approximation (offset small compared to depth), the series in equation (3.26) can be truncated to obtain the familiar hyperbolic form

$$t^2 = t_0^2 + \frac{x^2}{v_{rms}^2} \quad (3.27)$$

Comparing equation (3.25) and (3.27) we find that the velocity required for NMO correction for a horizontally stratified medium is equal to the rms velocity, provided the small-spread approximation is made.

**The stacking velocity ( $V_{st}$ )** is the velocity value determined by velocity analysis that is used for common-midpoint stacking. In the limit as offset approaches zero, it approaches the NMO velocity. The difference between stacking velocity and NMO velocity is sometimes called the spread-length bias. It should be noted that the stacking velocity better should be called stacking function because it is not really a velocity. It specifies the hyperbola which would describe the moveout curve for a particular reflector if the velocity were constant from the surface to the reflection. This is only the case in the very shallow beds. In most cases the stacking velocity represents the best fit of a hyperbola to the non-hyperbolic normal moveout. It should also be noted that the stacking velocity will vary with offset range.

It is given by the equation

$$t^2 = t_0^2 + \frac{x^2}{V_{st}^2} \quad (3.28)$$

**The migration velocity**, conceptually, is similar to the stacking velocity. Whereas the stacking velocity best characterizes the normal moveout of reflection times across a CMP gather of traces, the migration velocity best characterizes the moveout of diffraction times both across different CMP gathers and across traces within those gathers. Hence, the migration velocity should be the appropriate parameter for migrating seismic data. Unlike the stacking velocity, the migration velocity is insensitive to the dip of the reflector to which it pertains and hence is single valued in space and is spatially more correct. For horizontally layered media, the two forms of velocity coincide (Hubral & Krey 1980).

Figure 3.3 illustrates some velocity definitions. Based on an interval velocity model we see that the rms velocity  $V_{rms}$  resulting from equation (3.24) is larger than the corresponding average velocity  $\bar{V}$  (after equation (3.23)). We also see, if we recalculate the interval velocity  $V_i$  from rms or Average velocity using Dix formula equation (3.21), that in the case of the average velocity the resulting interval velocity is too small. The average velocity is what we are looking for, what we need for the time-to depth conversion or migration and what - for small intervals - gives the lithological relevant velocity.

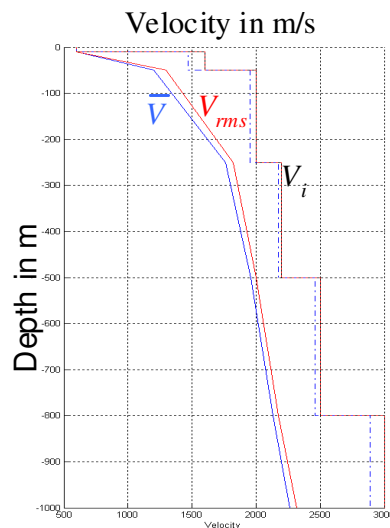


**Figure 3.3:** Velocity depth model and calculated rms and average velocity as well as recalculated interval velocity by Dix formula (equation (3.21)). Black: given  $V$  interval, blue: calculated  $\bar{V}$  average, red: calculated  $V_{rms}$ , blue dash dot:  $V_i$  (calculated by Dix formula from  $\bar{V}$ ) dot:  $V_i$  (calculated by Dix formula from  $V_{rms}$ ).

The average velocity is calculated for a straight line vertical path and is obtained from the weighted average of  $1/V_i$ , the weights being the layer thicknesses. The NMO velocity  $V_{NMO}$  holds for the one layer case (straight paths, hyperbolic form, the equation for a hyperbola is met only in a situation of constant velocity). The rms velocity applies to horizontal velocity layering as the offset goes to zero and  $V_{rms}^2$  is the weighted average of  $V_i^2$ , the weights being the one-way vertical traveltimes through each bed and more weight is given to high-velocity beds. This is consistent with the fact that the least-time path between two points involves changes in path direction that increases travel in the high-velocity layers. Thus, using  $V_{rms}$  somewhat compensates for the failure of straight-line paths to account for ray bending at interfaces (e.g., the difference of the paths SAE and SBE in Figure 3.2). The stacking velocity  $V_{st}$  even holds for curved raypaths when the velocity varies by depth and thus generally is higher than the rms velocity.

**The refractor velocity** is determined by the analysis of refracted waves. These waves travel along the layer boundary and travel predominantly horizontally in the layer using the layer with the higher velocity. The refractor velocity may be up to 20% higher than the vertical average velocity due to fine bed layering.

**Phase velocity** means the velocity of any given phase (such as a trough or a peak) or a wave of single frequency; it may differ from group velocity, the velocity with which the energy in a wavetrain travels, because of dispersion (variation of velocity with frequency).

### **3.4 Different ways to Quantify Seismic Wave Velocities**

The seismic velocity can be determined from laboratory measurements, sonic logs, and vertical seismic profiles or from velocity analysis of seismic data. It varies as a function of how it is derived from the data. For example, vertical seismic profiling (VSP) and sonic log measurements are two different techniques providing the information about the structure surrounding a particular well. The two techniques use significantly different frequencies of seismic signals.

VSP and sonic log velocities (or traveltimes) are often found to disagree. Recent field evidence (Stewart et al., 1984) of these differences suggests that the VSP traveltimes are delayed with respect to the integrated sonic times. More detailed analysis of seismic wave propagation in the

VSP shows that short-path multiples and velocity dispersion can have a significant delaying effect on the seismic traveltimes (Stewart et al., 1984).

### 3.4.1 Laboratory Measurements

In the laboratory velocities for shallow subsurface rocks are determined by measuring the travel-time of a pulse transmitted through cylindrical rock specimens with high frequency i.e. about tens to hundreds of kHz. Ultrasonic transducers are used to transmit the pulse through a sample of the material in question. As the length of the specimen is known, a velocity can be calculated. Laboratory measurements of velocity of unconsolidated sediments for shallow depths are usually made at low confining pressures ( $\sim 0.1\text{MPa}$ ). The following equation from Aracne-Ruddle et al. (1999) is often used to compute the ultrasonic wave velocities for P- and S- waves from laboratory experiments.

$$V = \frac{10^4 l}{t_{arr} - t_0} \quad (3.29)$$

Herein,  $V$  denotes velocity (of P- or S-waves), m/s;

$10^4$  is a factor converting  $\text{cm}/\mu\text{s}$  to  $\text{m/s}$ ;

$l$  is the distance travelled by the wave,  $\text{cm}$

$t_{arr}$  is the observed arrival time of the wave,  $\mu\text{s}$ ; and

$t_0$  is the system correction time ( $t_0$  established by aluminium calibration experiments),  $\mu\text{s}$ .

Figure 3.4 shows the P- and S-wave velocities as a function of pressure. The measurements were made with a frequency of about 100 kHz.

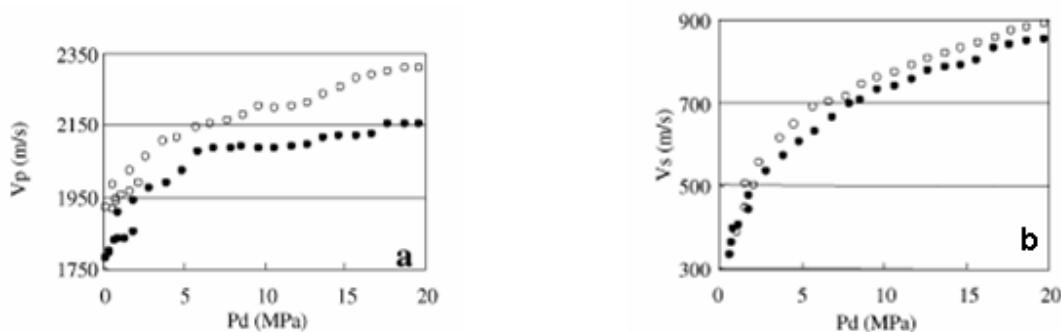


**Figure 3.4:** Plot of laboratory measured P- and S-wave velocity  $V_p$  and  $V_s$  versus pressure  $P_d$  for two water-saturated sands with different grain sizes, open circle for fine grained and solid circles for coarse grained (from Prasad & Meissner, 1992).

### 3.4.2 Vertical Seismic Profiling (VSP)

Vertical Seismic Profiling (VSP) is a form of seismic surveying that utilizes boreholes. Shots are normally fired at the surface, at the wellhead or offset laterally from it, and recorded at different depths within the borehole using special detectors clamped to the borehole wall (Figure 3.5).

Through VSP seismic wave velocities are measured from direct and reflected waves propagating through strata intersected by a borehole at frequencies from tenth to hundreds of Hertz and at scales hundreds of meters. VSP data can be used as a near-surface imaging tool directly. Its information can be applied for geotechnical purposes as well as ground water exploration. VSP generally gives better data than the surface seismic method because the energy does not have to travel as far and therefore undergoes less attenuation. It also investigates a target formation more closely and measures depth accurately. Further description is given by Hardage (1991).

First breaks plus the upgoing and downgoing events that follow first breaks can be recorded in a vertical seismic profile (Figure 3.5). VSP can supply information about both velocity and subsurface interface locations. First break times provided by VSP data can be used to determine travel time at any borehole depth. The interval velocity can also be extracted from the VSP data (Figure 3.6).

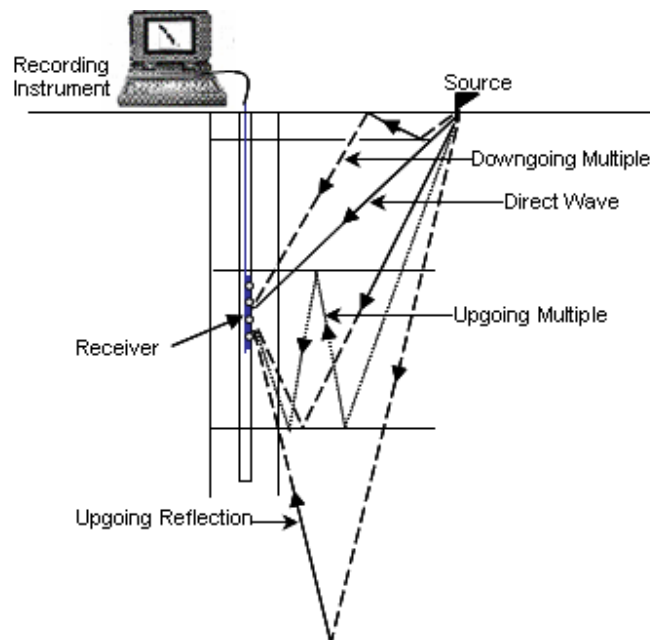


**Figure 3.5:** Schematic diagram of a VSP survey (from DiSiena et al., 1984).



VSP surveys are rarely used alone. It is a means of obtaining improved information about the subsurface. In a standard CMP survey, the velocity control provided by the VSP survey allows enhanced accuracy in the conversion of time sections to depth sections; multiples and primary reflections can easily be identified and deconvolution operators can be designed to eliminate the multiples. VSP surveys have been shown to be a useful technique for near-surface investigations (Skvortsov et al., 1992; Milligan et al., 1997).

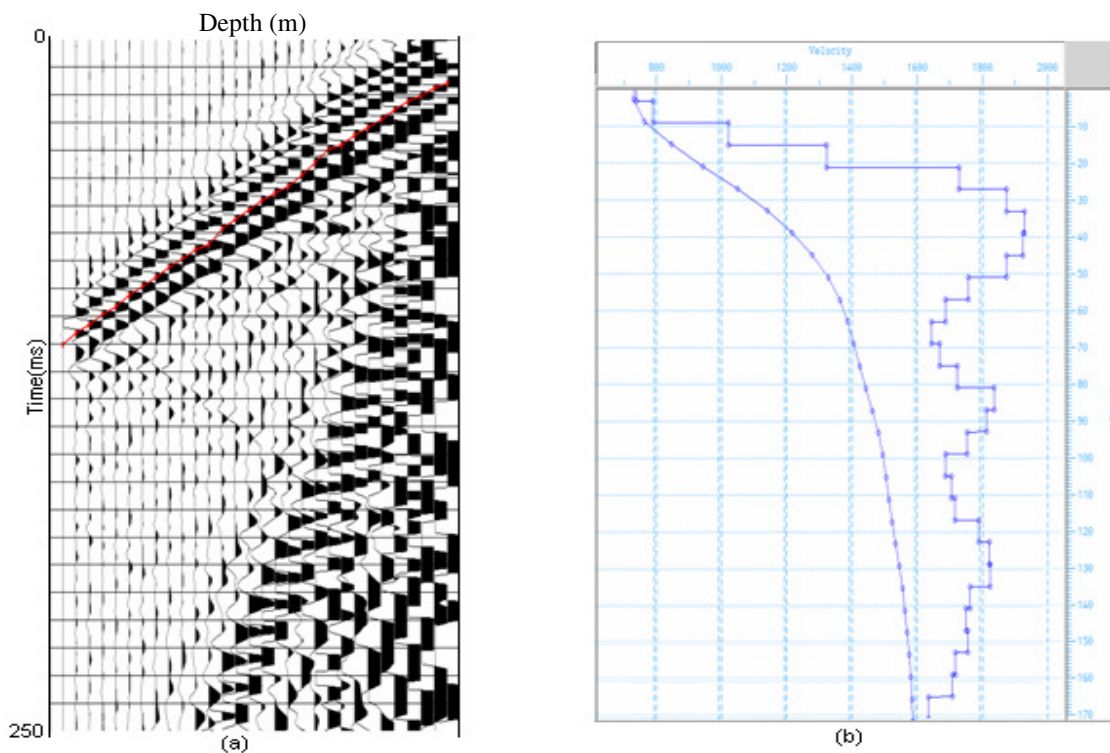


**Figure 3.6:** (a) P-wave VSP data (Z-component) with the first break picks from a vibroseis source with a zero-phase wavelet. (b) The average and interval velocities are in m/s (Rumpel et al., 2005a).

### 3.4.3 Sonic Logging

This method uses high frequency observations and is based on the study of the propagation of sonic (50-5000 Hz) and ultrasonic (20-50 kHz) pulses in rock with short source-receiver spacings. The method enables the geologic column to be sectioned into layers down to fractions of a meter thick. The seismic properties of the formation (P-wave velocity, shear-wave velocity and some times intrinsic attenuation) adjacent to the borehole can be measured with sonic logging tools.

Sonic logging makes use of one or two pulses and two or four receivers, all located in the tool, which is lowered into the well (Figure 3.7). The tool measures the travel time of a P-wave between two sensors to give the velocity. The travel time to the top of the sonic log and to other depths are often determined by direct measurement from the surface to a borehole geophone. The sonic log shows the results as the reciprocal of the P-wave velocity in the formation. A sonic log, as opposed to seismics, measures velocity more directly. For more details on sonic logging see e.g. Sheriff & Geldart (1995).

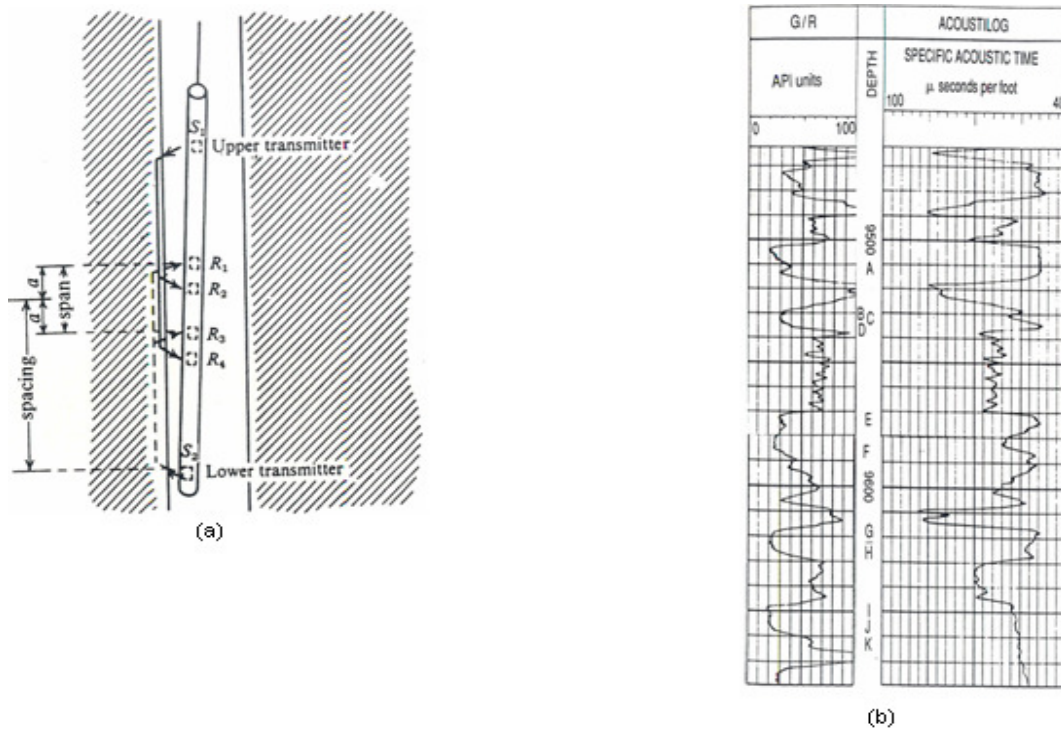


**Figure 3.7:** Sonic logging, (a) Borehole-compensated sonde; (b)  $\gamma$ -ray (left) and P-wave velocity log (right).

### 3.4.4 Velocity Analysis of Surface Seismic Data

Surface seismic data provide an indirect measurement of velocity. In surface seismic measurements, both the energy source and the receivers are positioned on the earth's surface (Figure 3.8a). The basic technique of the method consists of generating seismic waves and measuring the time required for the waves to travel through the sub-surface. The waves may be reflected and refracted back to the surface to a series of geophones. The elapsed time between the source being triggered and the arrival of the various waves is then used to determine the velocity of the waves (Figure 3.8b).

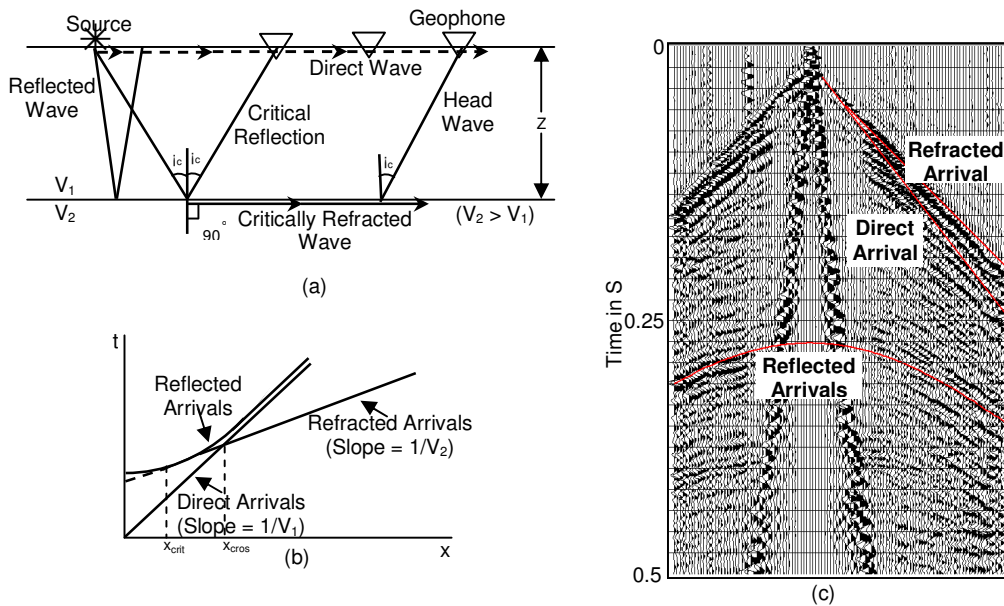


**Figure 3.8:** Surface seismic technique; (a) raypaths for two layer medium; (b) traveltime curves; (c) sample seismogram from the survey area with the direct, refracted and reflected arrivals.

Figure 3.8c shows a seismogram with direct, refracted and reflected arrivals. From the seismogram travel-time versus distance graphs can be constructed (Figure 3.8b) and velocities can be calculated for the overburden and refractor layers through the analysis of this curve. In the case of reflected arrivals the stacking and the interval velocity can be determined by applying a number of processing steps. The surface seismic method is applied in this work and will be presented in detail in the next chapter.

### 3.5 Factors Affecting Seismic Velocities

Seismic velocity generally increases downward as one goes from the unlithified sediments and soils near the surface into more consolidated rocks; it increases as well when the wave passes from the unsaturated into the saturated zone. There are a number of factors responsible for these velocity changes in the near-surface materials like lithology, porosity, cementation, pressure and interstitial fluids (Figure 3.9).

The most obvious factor controlling seismic velocity is the lithology of the media. Yet, because of much overlap between the ranges of seismic velocity for different earth materials the lithological identification is not unique (Table 3.1). For example a high velocity of sedimentary rocks generally indicates carbonates and a low velocity indicates sands or shales, whereas an

intermediate velocity can indicate either. These overlappings hinder the differentiation between carbonates and sandstone using  $V_p$ .

Rock Type	$V_p$ (m/s)	$V_s$ (m/s)
Vegetal Soil	300-700	100-300
Dry Sands	400-1200	100-500
Wet Sands	1500-2000	400-600
Clay	1100-2500	400-1000
Till	1500-2500	600-1000
Marls	2000-3000	750-1500
Saturated Shale/ Sand Section	1500-2200	500-750
Porous Saturated Sandstones	2000-3500	800-1800
Limestones	3500-6000	2000-3300

**Table 3.1:** A list of typical P-wave and S-wave velocities of various rock types from (Jaeger et.al., 2007) and (Todd, 1980).

Thus P-wave velocity cannot be used to uniquely discriminate lithology contrasts; S-wave velocity can reduce the ambiguity. Laboratory investigations from Milholland et al. (1980), Domenico (1984) and Castagna et al. (1993) suggest that a relationship exists between the ratio of seismic P-wave and S-wave velocities ( $V_p/V_s$ ) and sedimentary rock lithology. Therefore the  $V_p/V_s$  relation may be a better key to the determination of lithology from seismic data. The  $V_p/V_s$  intervals in Table 3.2 represent 90 percent confidence intervals with the exception of the velocity ratio for shale (Tatham & McCormack, 1991).

Rocks	$V_p/V_s$
Sandstone	1.59-1.76
Calcareous Sandstone	1.67-1.76
Dolomite	1.78-1.84
Limestone	1.84-1.99
Shale	1.70-3.00

**Table 3.2:** Typical  $V_p/V_s$  values for sedimentary rocks (Domenico, 1984).

Porosity is another important factor in determining the elastic wave velocity of rocks. Generally, increasing porosity leads to lower velocities for both P- and S-waves. Several studies have been conducted in order to determine a relationship between P-wave velocity and porosity for a variety of sedimentary rocks. One of the earliest and most widely used relations is the Wyllie time-average equation of Wyllie et al. (1958),

$$\frac{1}{V_p} = \frac{\Phi}{V_{p-f}} + \frac{1-\Phi}{V_{p-m}} \quad (3.30)$$

where  $\Phi$  is the porosity,  $V_p$  is the P-wave velocity of the saturated rock,  $V_{p-m}$  the P-wave velocity of the mineral rock and  $V_{p-f}$  the P-wave velocity of the pore fluid. This relation is valid when the rocks have relatively uniform mineralogy, when they are fluid saturated and at high effective pressure. The Wyllie time-average equation can be used to estimate porosity values by utilizing interval velocities extracted from seismic data. Assumptions and limitations for the Wyllie time average equation and suggested improvements by others are discussed by Mavko et al. (1998).

Pore fluids play another role in altering the bulk properties of porous rock, namely through pore pressure. In fact  $V_p$  is primarily affected by variations in pore fluid properties. For example,  $V_p$  of water saturated media is higher than  $V_p$  for the same material when it is air saturated.  $V_s$  is only essentially dependent on changes in pore fluid density which is due to the lack of rigidity in fluids ( $\mu_{fluids} = 0$ ).

Density is a basic property used to describe rock materials. The dependence of P- and S-wave velocity on density is not immediately obvious but, in general, denser rocks have higher seismic velocities, contrary to what one would expect from a first glance at equations (3.17) and (3.19). This occurs because the elastic moduli  $K$  and  $\mu$  are also dependent on  $\rho$  and increase more rapidly than  $\rho^{1.0}$ . A linear relationship, termed Birch's law, between density and seismic velocity is of the form

$$V = a\rho + b \quad (3.31)$$

where  $a$  and  $b$  are constants; it fits measurements from many natural rocks fairly reasonably (Fowler et al., 2005). For porous rocks Gardner's relation represents a useful empirical relationship (Mavko et al., 1998):

$$\rho_b \approx 1.741V_p^{0.25} \quad (3.32)$$

with P-wave velocity  $V_p$  in km/s and bulk density  $\rho_b$  in g/cm<sup>3</sup>.

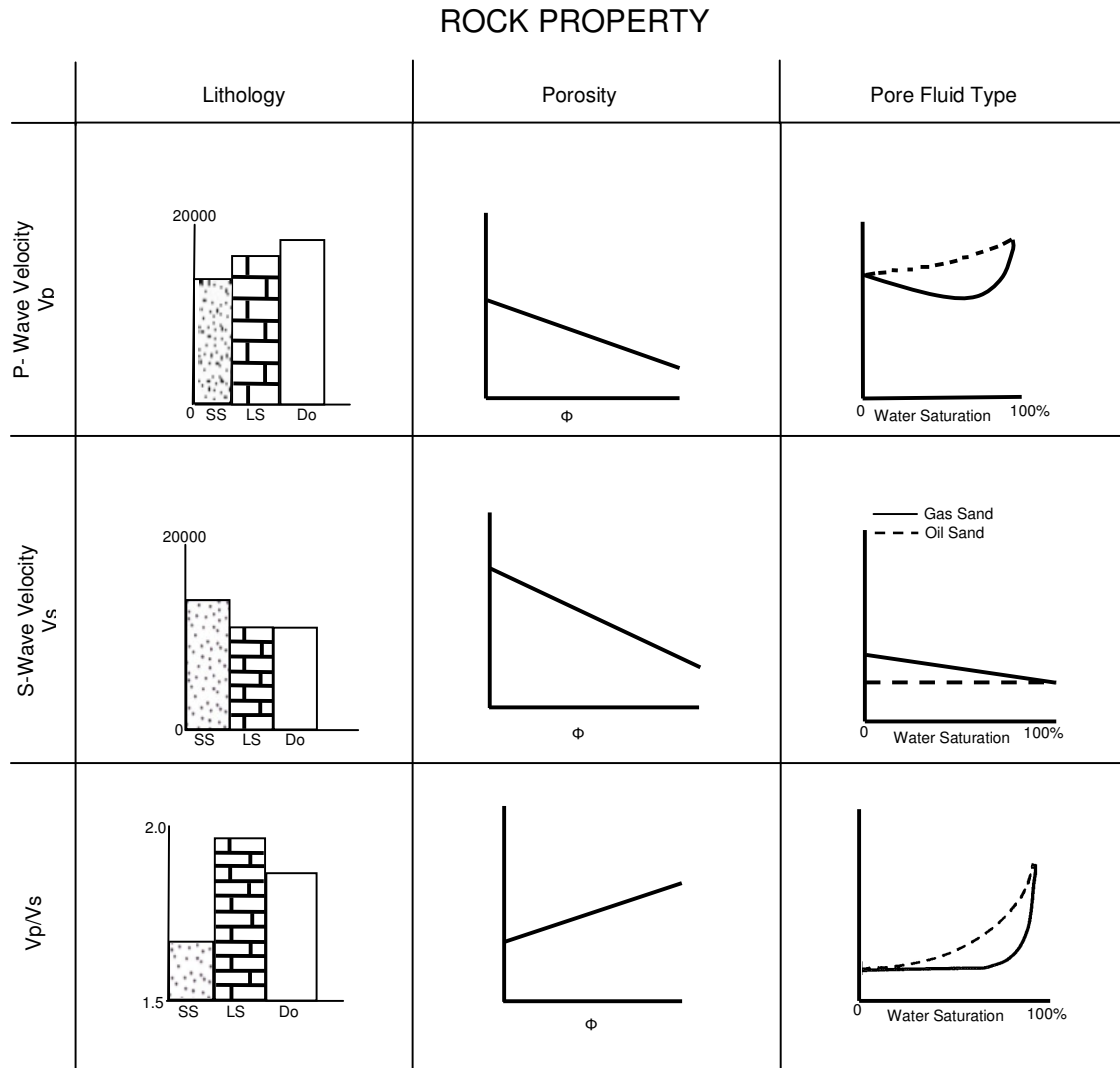


**Figure 3.9:** Summary of the effect of different rock properties on the seismic P- and S-wave velocities and the velocity ratio  $V_p/V_s$ . Various rock properties are listed across the top of the figure, while the velocities and the velocity ratio are on successive rows. SS-Sandstone, LS-Limestone and DO-Dolomite (Tatham & McCormack, 1991).

## 4. Near-Surface Seismic Methods

Near-surface seismic methods are geophysical techniques that involve the generation and recording of seismic waves for the purpose of mapping the shallow subsurface. Its fundamental principle is to accurately record ground motion caused by known sources in a known location. The near-surface seismic method is targeting subsurface structure within a couple of hundred meters. It is applied to a broad range of problems, such as locating the water table, mapping shallow bedrock surface, delineating shallow faults, mapping geologic structure and stratigraphy of materials. It is also applied in hazard assessment and aquifer contamination study.

Interest in the development and application of near-surface seismic techniques for investigating a wide variety of geological, environmental and engineering problems has grown significantly over the past two decades. It has been in the spotlight of several researches: Knödel et al. (2007), Kirsch (2006), Butler (2005), Rubin & Hubbard (2005), Spitzer et al. (2000), Miller et al. (1995), Pullan & Hunter (1990), Miller & Steeples (1990), Steeples & Knapp (1982), Doornenbal & Helbig (1983), Steeples (1984) and several others have attempted to resolve small-scale structures in the very shallow subsurface (<100 m depth).

In near-surface seismic techniques both the source and the receiver are deployed at the surface in order to image the different layers of the ground. The source and the receiver are arranged in a spread with a certain offset for that source-receiver pair. In this technique structural information is derived principally from paths that fall into two main categories: headwave or refracted paths, in which the principal portion of the path is along the interface between two rock layers and hence is approximately horizontal, and reflected paths in which the wave travels downward initially and at some point is reflected back to the surface, the overall path is essentially vertical.

For the detailed sub-surface characterization there are different options as near-surface reflection seismic methods with P- and S-waves, first arrival analysis with refraction tomography or even the analysis of surface waves. The next section includes the fundamentals of the aforementioned techniques and applications.

## 4.1 Near-Surface Seismic Reflection Method

In near-surface seismic reflection high frequency signals generated by a small seismic source are transmitted into the ground, reflected at shallow subsurface boundaries where there is a change in acoustic impedance  $I$  (the product of material density and seismic velocity, equation 4.1), and recorded as a function of time by a series of receivers (geophones) on the ground surface (Figure 4.1). The amount of energy that is reflected by an interface is dependent upon the acoustic impedance contrast, the greater the contrast the more energy is reflected. Contrasts in acoustic impedance are generally associated with lithological boundaries, such as the overburden bedrock interface.

$$I = \rho V \quad (4.1)$$

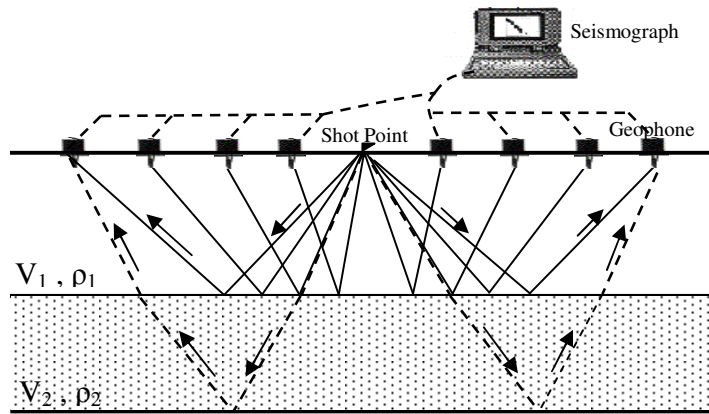


**Figure 4.1** Geometry of reflected wave paths for a horizontal interface

The strength of a reflection is defined by the reflection coefficient,  $R$ . It is the ratio of the amplitude of the reflected wave to the amplitude of the incident wave. In the general case for an interface between two solids when the incident angle is not zero, four waves are generated: the reflected P-wave and S-wave and the transmitted P-wave and S-wave. The partition of energy is expressed by Zoeppritz's equations.

The reflection coefficient for normal incidence (or for angles of incidence on an interface close to zero) is given by

$$R = \frac{\rho_2 V_2 - \rho_1 V_1}{\rho_2 V_2 + \rho_1 V_1} \quad (4.2)$$

where  $\rho_1$ ,  $V_1$  are the density and velocity respectively of the medium of the incident ray, and  $\rho_2$ ,



$V_2$  are the density and velocity of the other medium in contact with the incident ray medium. The value of the reflection coefficient would, therefore, change its sign depending upon whether the incidence is considered from above or from below the reflecting boundary. Incidence from a medium with high impedance value to a medium with low impedance value gives a negative reflection coefficient and incidence from the other side gives a positive reflection coefficient. The energy recorded by the geophone depends on the value of R, which can vary theoretically from -1 to +1. Typical values of R are approximately -1 from water to air, meaning that nearly 100% of the energy is reflected and none is transmitted; ~ 0.5 from water to rock; and ~ 0.2 for shale to sand (Upadhyay, 2004). The transmission coefficient is defined in analogue way as the ratio of the amplitude of the wave transmitted through an interface to that of the incident wave. Reflection and transmission coefficient add up to 1.

#### 4.1.1 Basic Principles

The theory and principles used in near-surface seismic reflection method is an adaptation of the theory and procedure pioneered in the deeper seismic reflection surveying. In seismic reflection surveys the travel-times of waves reflected from subsurface interfaces are measured to obtain information about depths and geometrical shapes of the interfaces. The most important problem in seismic reflection surveying is the translation of two-way travel time to depth. While travel times are measured, the one parameter, that most affects the conversion to depth is seismic velocity. In this section the basic relation between travel times and the location of the reflecting interface is described.

For the simple case of a single horizontal reflector at a depth  $Z$  beneath a homogeneous top layer of velocity  $V$  the equation for the travel time  $t$  of the reflected ray from a shot point to a detector at a horizontal offset  $X$  is given by the ratio of the travel time path length to the velocity:

$$t = (x^2 + 4z^2)^{1/2} / V \quad (4.3)$$

Substituting  $x = 0$  in equation (4.3), the travel time for a geophone at the source is obtained:

$$t_o = \frac{2Z}{V} \quad (4.4)$$

In the case of a dipping reflector, the reflectors in reality are often not horizontal but dipping, e.g., Figure 4.2, the travel times can be derived with the help of the cosines rule as follows:

$$\frac{V^2 t^2}{(2Z \cos \theta)^2} - \frac{(x + 2Z \sin \theta)^2}{(2Z \cos \theta)^2} = 1 \quad (4.5)$$

The equation has the form of hyperbola, where the symmetry axis does not lie on the zero offset time axis (Figure 4.2).

$$V^2 t^2 = (2Z \cos \theta)^2 + (x + 2Z \sin \theta)^2 \quad (4.6)$$

$$t^2 = \frac{(2Z)^2}{V^2} \left[ 1 + \frac{x^2 + 4xZ \sin \theta}{4Z^2} \right] \quad (4.7)$$

Using the standard binomial expansion, the following expression is obtained:

$$t \approx t_0 \left( 1 + \frac{x^2 + 4xZ \sin \theta}{8Z^2} \right) \quad (4.8)$$

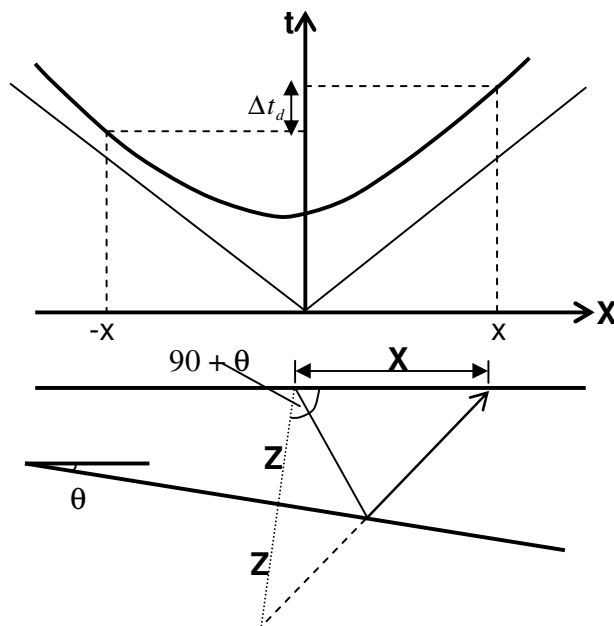


**Figure 4.2:** Ray path and traveltime diagram for a dipping reflector.

The normal moveout, that is the variation of reflection arrival with offset, for the horizontal layer case is

$$\Delta t_n \approx \frac{x^2}{2V^2 t_0} \quad (4.9)$$

and the additional dip moveout is

$$\Delta t_d \approx \frac{2x}{V} \sin \theta. \quad (4.10)$$

### **4.1.2 Data Acquisition System (source, receiver, geometry)**

Mapping of small-scale features in the near surface needs much higher resolution than it is usually demanded in conventional seismic surveys. Improvement of horizontal resolution to the limits defined by the first Fresnel zone (Figure 4.3) of the target reflectors may be achieved by simply decreasing source and receiver intervals. In contrast, higher vertical resolution requires broader bandwidth signals (Figure 4.4), which in turn suggests that special account for the capabilities of the source and recording instrumentation is needed. Sources must be capable of generating a wide band of high frequencies (>100 Hz), and receivers must be capable of faithfully recording them. Early summaries of the instrumentation and special acquisition strategies required for successful applications of shallow 2-D seismic techniques were given by Knapp & Steeples (1986a, 1986b).

The field layout is done analogue to exploration seismology that means, that the common-midpoint (CMP) method is commonly used. Subsurface reflection segments are covered by several shot-receiver pairs at different offsets. This multi-fold coverage is realized by continuously moving source points and geophone spreads along a seismic profile.

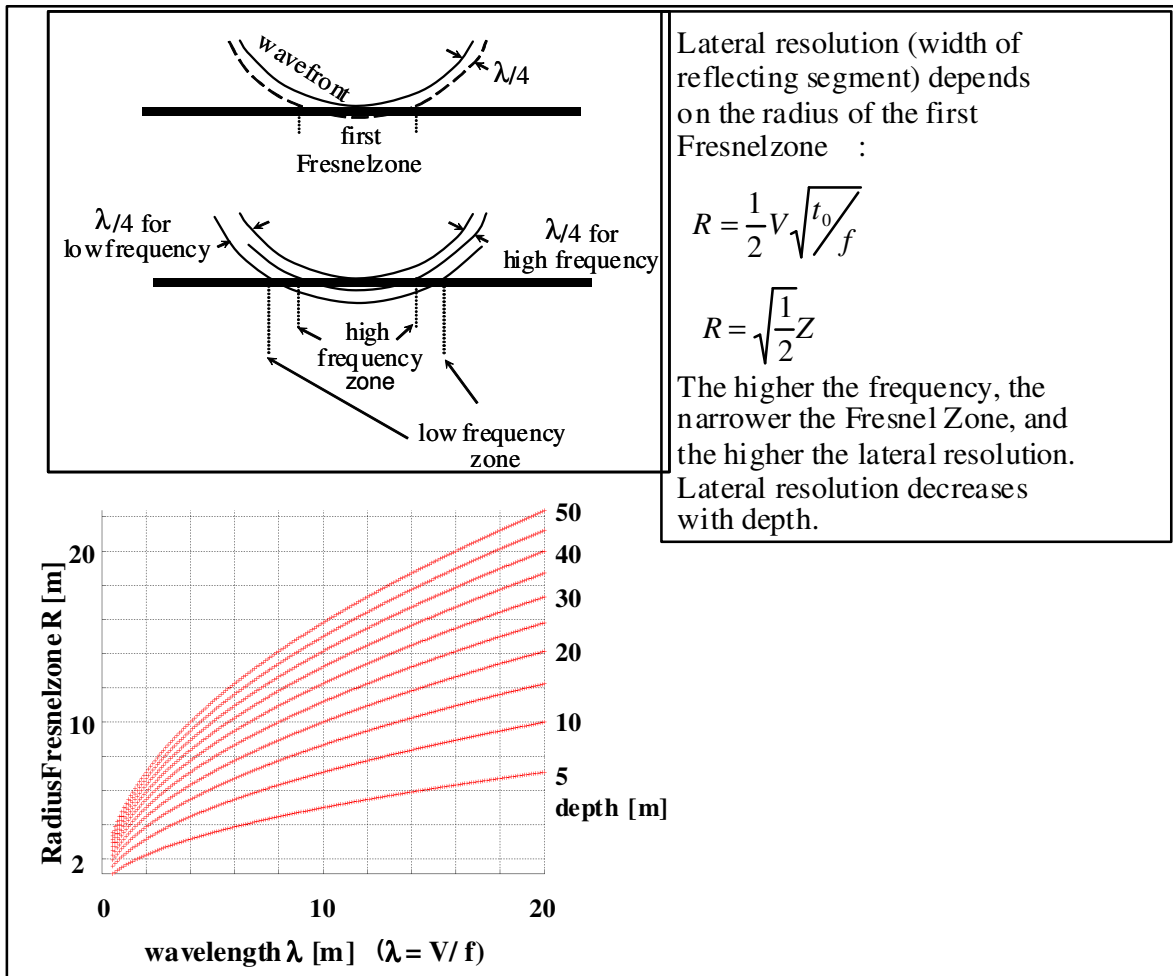


Figure 4.3: Demonstration of lateral resolution depending on the radius of the first Fresnelzone.

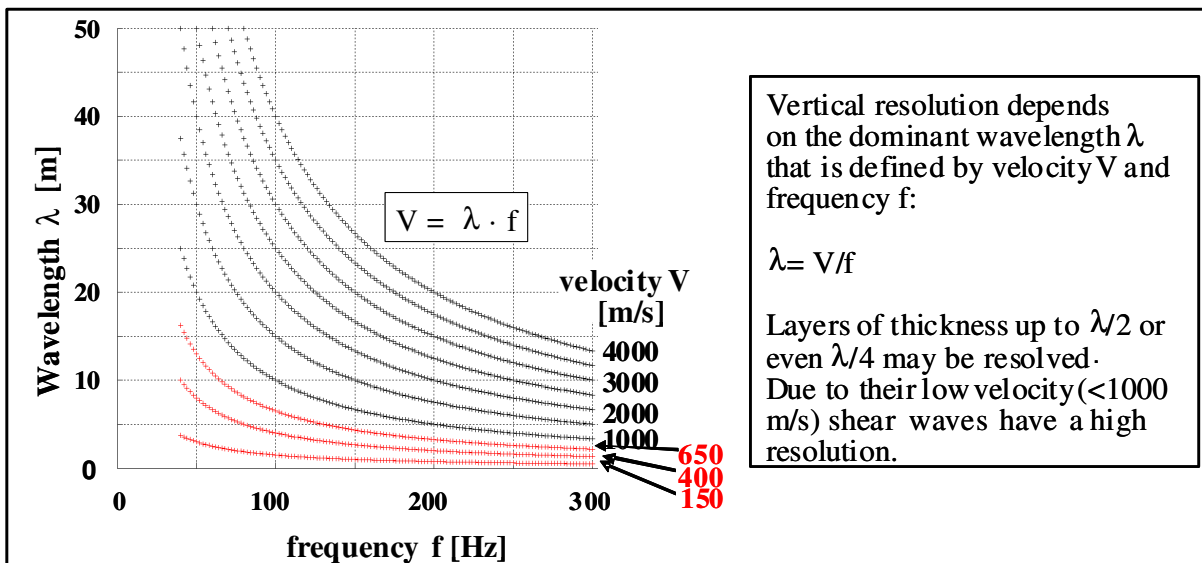
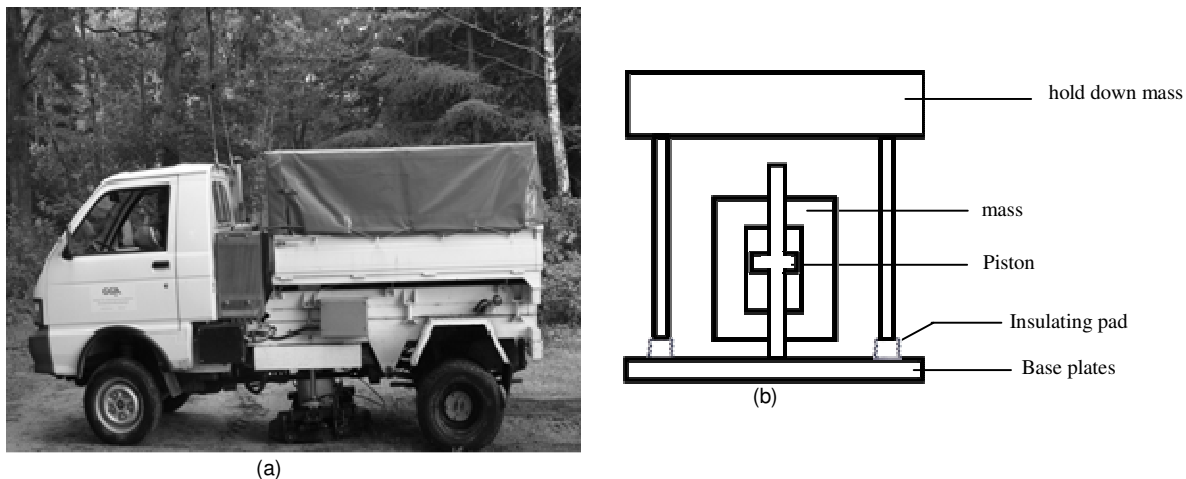


Figure 4.4: Demonstration of vertical resolution depending on velocity and frequency.

The selection of seismic recording equipment, energy source, and data-acquisition parameters is often critical to the success of a shallow-reflection project. In this study for near surface seismic reflection a vibroseis source and a landstreamer are used. Below, the principle and purpose of the vibroseis source and the landstreamer and the field acquisition technique are described.

Vibroseis is the most common non-explosive source used for reflection surveying and is now widely used in acquisition. It is a non-destructive method with a controllable frequency range. It often uses truck-mounted vibrators (Figure 4.5) to pass energy into the ground by an extended vibration signal of low amplitude and continuously varying frequency known as sweep signal. A typical sweep signal lasts from several seconds up to a few tens of seconds and varies progressively in frequency.



**Figure 4.5:** Vibrators (a) photo vibrator (LIAG Vibrator) (b) basic principles.

The field record is cross-correlated with the known sweep signal (Figure 4.6). The correlated record has a similar appearance as the type of seismogram that would be obtained with a high-energy impulsive source such as an explosion, but the seismic arrivals appear as symmetrical (zero phase) wavelets known as Klauder wavelets. Telford et al.(1990) defines the Klauder wavelet as the autocorrelation of a linear vibroseis sweep.

The basic seismic convolutional model for a vibroseis source is

$$x(t) = r(t) * s(t) \tag{4.11}$$

where  $x(t)$  is the recorded trace,  $r(t)$  is the geological reflectivity,  $s(t)$  is the sweep and  $*$  is the convolution operator.  $x(t)$  has a recording length of  $r(t) + s(t)$ .

To remove the sweep, the trace is crosscorrelated ( $\otimes$ ) with the sweep. The equation for the deconvolved sweep  $cc(t)$  is

$$cc(t) = r(t) * s(t) \otimes s(t) \quad (4.12)$$

This equation can be simplified to

$$cc(t) = r(t) * k(t) \quad (4.13)$$

since the crosscorrelation of two identical sweeps is defined as a Klauder wavelet,  $k(t)$ . The recording length is now reduced to  $r(t)$ .

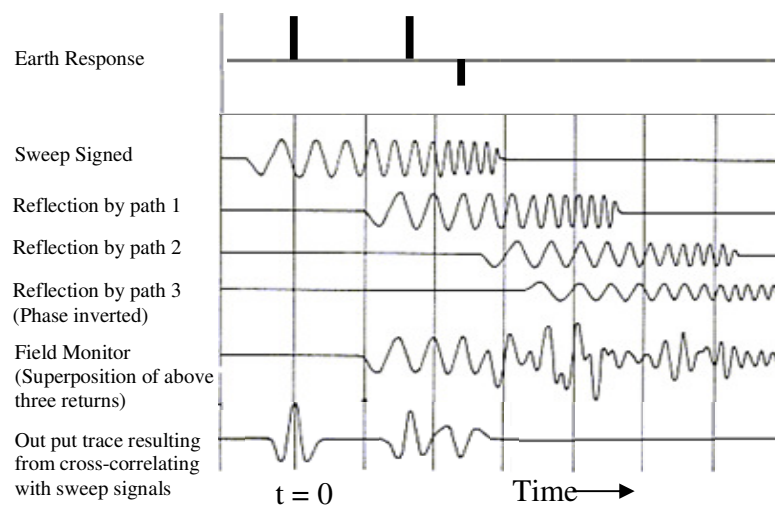


**Figure 4.6:** Steps in vibroseis sweep correlation (Kearey, 2002).

When the recorded data is crosscorrelated with the sweep, the remaining data will only contain information that is common to both waveforms; therefore the method acts also as a filter for the random noise eliminating the noise component outside the bandwidth (Figure 4.7).

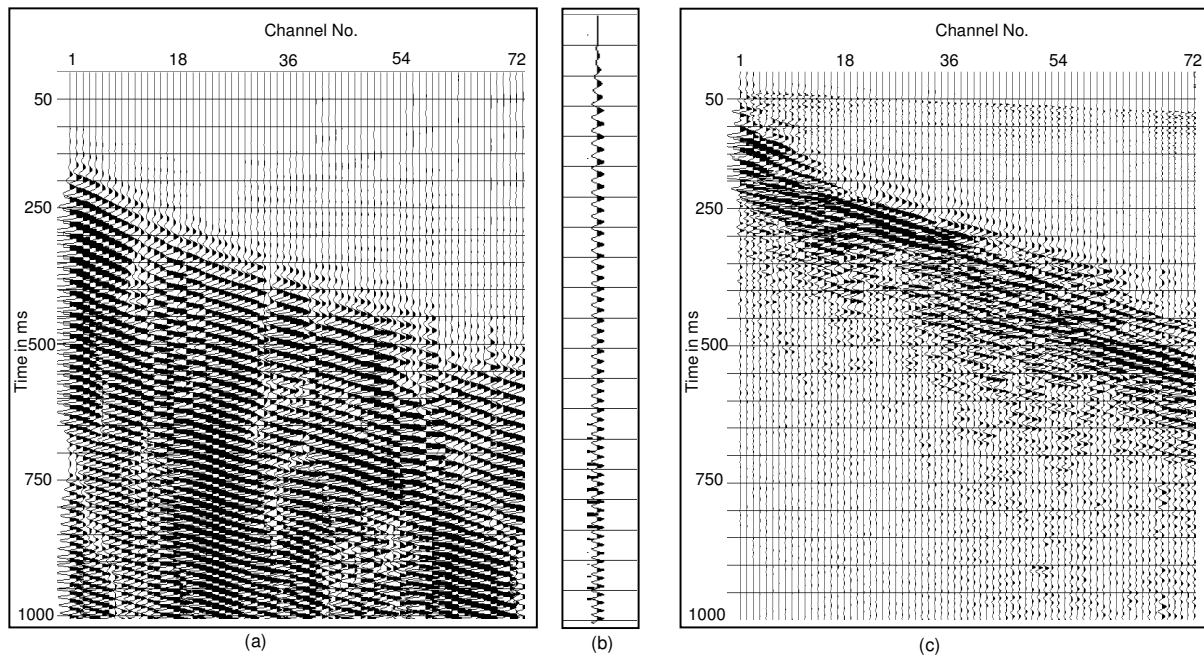


**Figure 4.7:** Sample of a shallow P-wave shot gather at the beginning of the profile  
 (a) uncorrelated vibroseis data (b) sweep signal (c) correlated data.

The planting and collecting of geophones in the field are time and labour consuming factors in high resolution seismic surveying. To reduce this effort land-streamer systems have been developed (e.g., Kruppenbach & Bedenbender (1975), van der Veen & Green (1998), Jensen et al. (2002), Miller et al. (2003)). Land streamers appear to provide a fast and comparatively economical method to collect the large volumes of data at close sensor spacings required to resolve near-surface velocity structures and provide a seismic image of the subsurface. Their usage reduces the costs of data acquisition.

The land streamer (Figure 4.8) used for this acquisition is constructed by LIAG institute (Polom et al., 2007). This land streamer comprises 72 SM4 20 Hz vertical geophones attached to segments of a standard seismic cable. The geophones are fastened by a rubber band on a metal base plate and the cables are kept inside a plastic hose for protection (Figure 4.8a). The spacing between receivers along a single cable segment is 1 m and thus the total streamer length is 72 m. The three point edition spike base plate creates a fair geophone-to-ground coupling and helps easy transportation. The other quality of this land streamer is that it is easy to replace the vertical geophones with horizontal geophones.

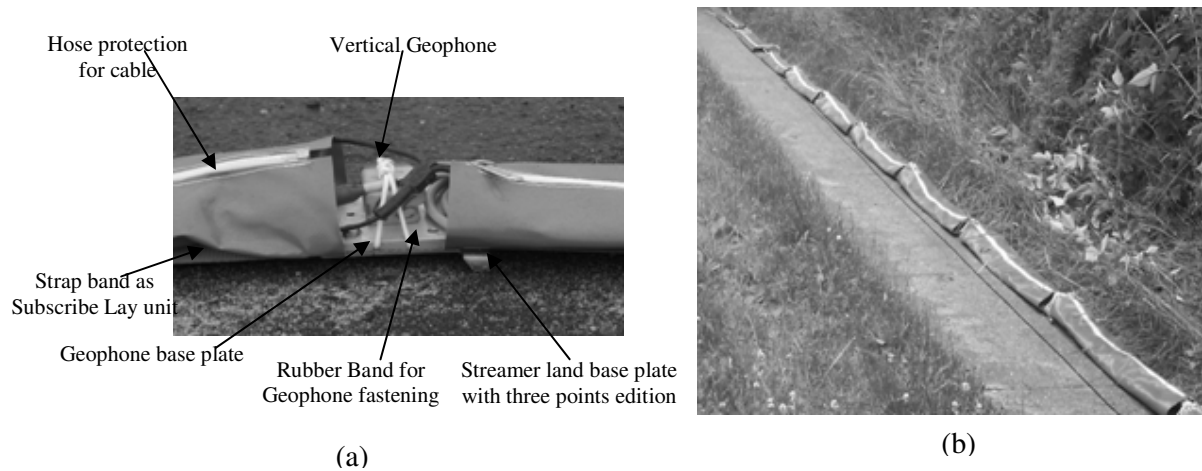


**Figure 4.8:** Landstreamer (a) Main parts of LIAG landstreamer (b) Photo of landstreamer.

Most modern seismic surveys widely use the common midpoint (CMP) technique of data acquisition, which has become the standard method for two-dimensional multichannel seismic surveying. In CMP technique shots are deployed at a number of different positions in relation to the geophone array in order to obtain reflections from the same point on the interface at different geophones in the array (Figure 4.9). The degree of redundancy at a particular point in the subsurface is known as fold. The fold of a CMP,  $N_{CMP}$ , is determined by the receiver spread length (= number of receivers  $N_G$  times receiver interval  $\Delta X_G$ ) and the shot interval  $\Delta X_S$  :

$$N_{CMP} = \frac{N_G \cdot \Delta X_G}{2\Delta X_S} \quad (4.14)$$

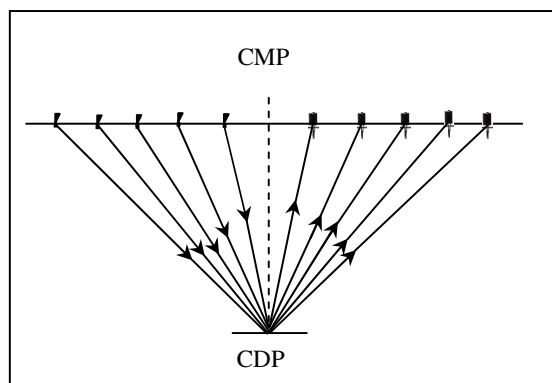


**Figure 4.9:** Principle of the common midpoint over a horizontal interface.



### 4.1.3 Reflection Data Processing Fundamentals

The main goal in processing reflection seismic data is to convert the data recorded in the field to the final seismic section, preferably a depth section. One step in processing seismic data is enhancing the signal with respect to the noise. This embraces improving of the temporal resolution of the seismic data; i.e. to remove the character of the input seismic signal (source) from the data and obtain the idealized impulse response of the earth model. And to improve the lateral resolution of the seismic data.

For most basic shallow high-resolution seismic reflection data the processing steps (Figure 4.10) employed routinely in conventional seismic surveying can be applied. However the processes are not a simple scaling down but special processing strategies are vital. There are three principal stages in seismic reflection data processing: deconvolution, stacking and migration (Yilmaz, 2000). Deconvolution is the most important process that aims to improve the vertical resolution and recognition of events. Stacking combines all the traces in a CMP gather together to increase the signal-to-noise ratio which improves the data quality. Migration is an inverse wave scattering calculation that relocates seismic reflections to the location of their origin. In addition, there are many auxiliary processes that are necessary to improve the primary processes.

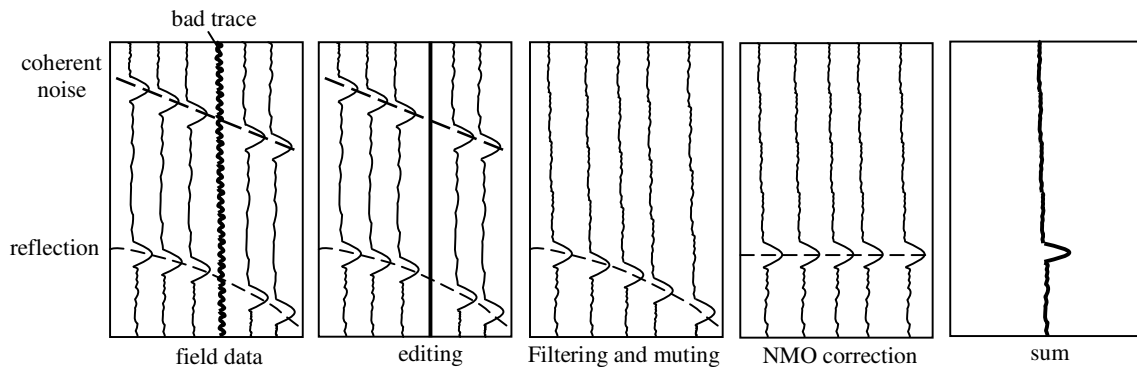


**Figure 4.10:** Simple schematic diagram of the main seismic reflection processing steps for a CMP gather.

Once the field geometry is incorporated into the data, they can be edited to remove dead traces (traces containing no information), traces that are dominated by noise or those monocyclic waveforms caused by electronic interference (Figure 4.10). As a seismic wave travels away from its source energy is lost by geometrical spreading or spherical divergence. As the rate of energy loss can be calculated, it can be compensated by applying a gain function to the data.

In near-surface seismic surveys various surface-related noises are superimposed on the shallow reflections. These noises mainly include direct waves, ground roll, guided waves, refractions or air waves (Figure 4.11). Either a combination of deconvolution, bandpass filtering and f-k filtering or simple spectral balancing is the most effective means of enhancing the amplitude and visibility of reflected signals relative to these noises (Baker et al., 1998), or application of carefully selected mutes helps not to mis-process and mis-interpret the surface-related noises as reflections. Figure 4.12 provides an example of scaled, filtered and muted shot gather acquired in the study area.

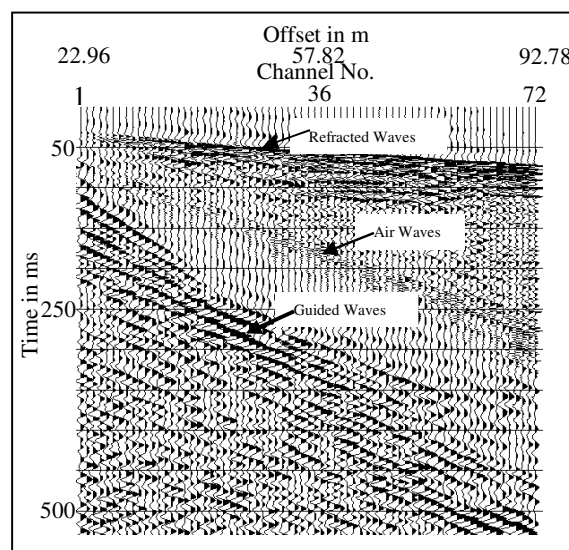


**Figure 4.11:** Shallow P-wave shot gather record from the study area. the raw data which displays surface related noises (guided, refracted and air waves).

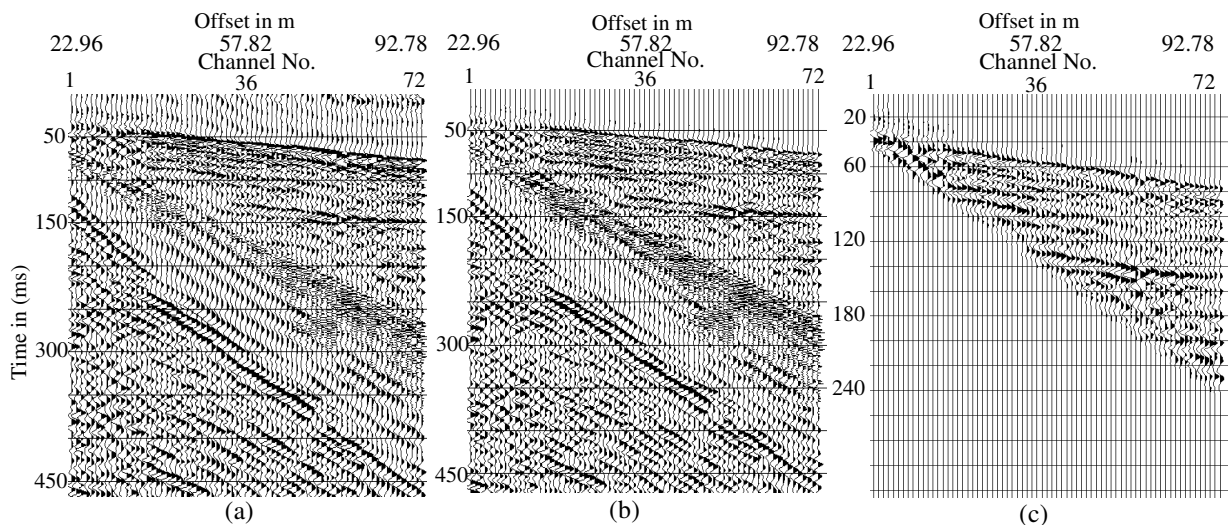


**Figure 4.12:** Single shot gather. (a) Scaled raw data (automatic gain control (AGC), 100ms). (b) After application of a band pass filter (40-60-400-440 Hz). (c) After mute applied.

Two types of correction are needed to be applied to reflection times on individual seismic traces in order that the resultant seismic sections give a true representation of geologic structure. These are the static and dynamic corrections. Static corrections are made to seismic reflection data to compensate for time shifts in the data caused by changes in topography and variations in near-surface seismic wave velocity. Dynamic correction is applied to reflection times to remove the effect of normal moveout.

Static corrections are an integral component in the processing of virtually all seismic reflection data recorded on land. Elevation and refraction static corrections are time shifts applied to traces to adjust for long-wavelength changes in elevation, or in thickness and propagation velocity of the weathering zone at different sources and receivers. The standard method is to perform datum statics, whereby each source and receiver is shifted in time to a flat datum. Refraction statics build a model for the low-velocity subsurface and compensates the travel time variations caused by the weathering zone velocities.

The proper handling of static corrections is an issue that is of critical importance to shallow seismic reflection surveys because of the high frequencies used, and the significant velocity and thickness variation that frequently exist in the very near surface range. Because of the high frequency involved, static time-shifts of only a few milliseconds can be comparable to the period of a seismic signal (Pugin and Pullan, 2000).

The purpose of the NMO correction is to subtract the additional time to a reflector due to increasing source-to-receiver offset, and to flatten the hyperbolic reflection (Figure 4.10). The NMO-correction depends on the offset and the velocity (equation 4.9). To obtain a flattening of the reflections, the velocity must have the correct value. One of the methods to determine the velocity is the analysis of velocity spectra for selected CMP gathers. The velocity spectrum is obtained by calculating the normal moveout for a range of velocities and displays the semblance as a measure of multichannel coherence (Figure 4.13). This can be plotted as traces or as iso-amplitudes. This method is commonly used by interactive software to determine the velocities. A detailed velocity analysis is an important and often time consuming step in the processing flow.

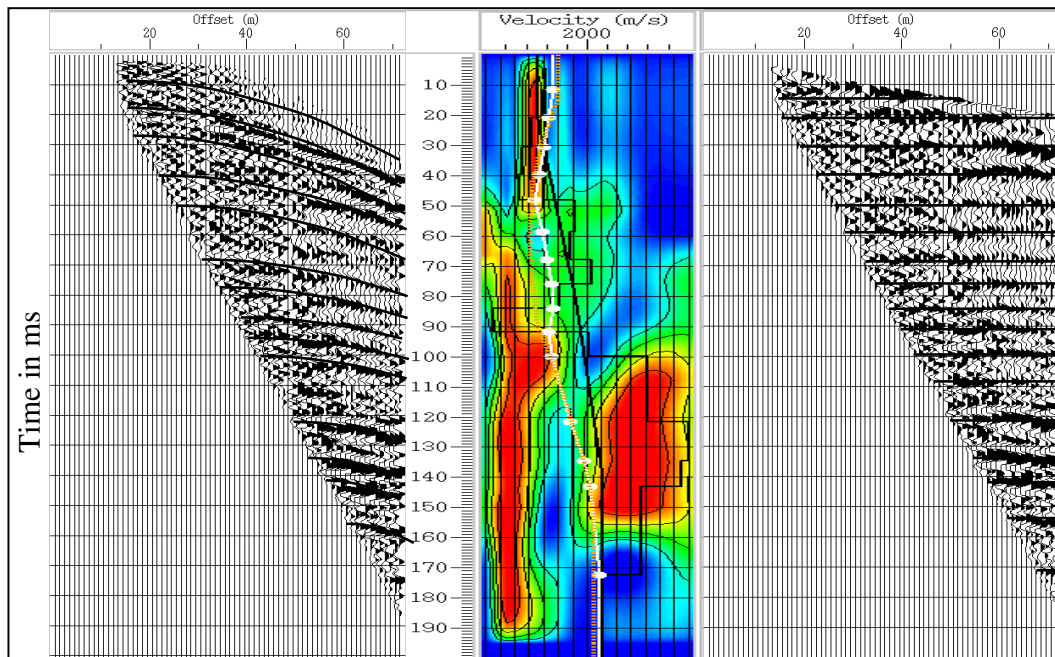


**Figure 4.13:** Velocity analysis; CMP gather (left) and its velocity spectrum with the picked velocities (middle), and the CMP gather after correction (right).

The final phase of seismic reflection processing involves stacking and migration. It is probably the most important phase of the seismic processing chain because at this point the image is constructed.

Migration is a central step in the seismic data processing flow. It is a wave-equation-based process that removes distortions from reflection records by moving events to their correct spatial locations (Figure 4.14), and by collapsing energy from diffractions back to their scattering points. Migration techniques are categorized in a variety of ways, relating to algorithm implementation. An algorithm which uses RMS velocities analytically and does not account for ray bending at interfaces is characterized as a time migration. On the other hand, an algorithm which uses interval velocities and accounts for ray bending at interfaces is characterized as a depth migration (Yilmaz, 1987). The most apparent difference between time and depth migration occurs in the final display of migrated traces. Time migration produces a time section, which interpreters can compare relatively easily with unmigrated time sections. The goal of time migration is to produce an image, not a geologically valid velocity field. On the other hand, depth migration is a more powerful interpretive processing tool, and its results can give us greater confidence in both the geologic structure and the velocity field than time migration can (Gray et al., 2001).

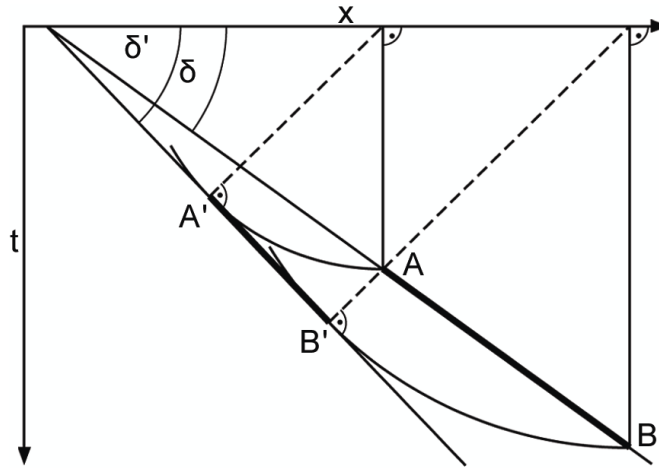


**Figure 4.14:** Migration principle: the reflection segment AB moves to segment A'B' when migrated.

Migrations are further categorized on the basis of algorithm or technique by which the migration correction is performed such as: Kirchhoff migration, Finite-difference migration, Reverse-time migration and Frequency-wavenumber migration. The theory of these methods has been presented in Yilmaz (1987) especially for poststack migration. Following discussions will expand upon the major characteristics of the Finite-difference migration implementations, since this migration method applied for the reflection data in this paper.

The tool Finite-difference migration in the ProMAX processing system encompasses those techniques which employed finite difference methods to solve the appropriate differential wave equation. The finite-difference migrations were based upon the approach outlined by Claerbout & Doherty (1972). It is applied in two steps: wavefield extrapolation and imaging. The wavefield extrapolation step consists of downward continuing the recorded data, using the scalar wave equation, into a form corresponding to a repositioning of the recorded plane. The imaging step consists of outputting a portion of migrated data corresponding to the zero travelttime of the repositioned dataset. The data are recursively migrated by using the output of one wavefield extrapolation as input for the next.

According to the type of wave equation being solved finite-difference migration classified into explicit and implicit finite-difference migration. Explicit finite-difference migration is based on repeated application of a local convolution. Implicit finite-difference migration methods solve an approximate “one-way” wave equation that supports only inherently stable solutions by design (Yilmaz, 1987).

## **4.2 Refraction Tomography Method**

In section 4.1.2 I have stated that direct waves and head waves (refractions) are noise for the seismic reflection method. This is completely contrary in methods using refraction or diving waves to characterize the near surface depth range. Conventional analyses of seismic refraction data sets have been utilizing a number of methods for a very long time. The general Reciprocal Method (GRM), delay-time, intercept-time or other similar techniques require simplifying assumptions such as constant velocity layers or lateral homogeneity. Where this assumption is not valid, these methods have limitations; one limitation is the inability to identify the existence of hidden layers or blind zones because of insufficient velocity contrast or layer thickness. Another limitation is incorrect depth calculations to layers where velocity reversals exist, i.e., where layer velocities do not increase with progressive depth (Rucker, 2000).

For example the GRM method (Palmer, 1981) calculates refractor depths using overlapping refraction arrival times from both forward and reverse shots. It uses the assumption that seismic velocities increase as a function of depth, i.e., the underlying strata to present a higher seismic velocity than the overlying layer. It is an iterative method that involves a set of XY-distance test values in the search for optimum XY (geophone separation). It is most applicable to subsurface layers dip less than approximately  $20^\circ$  and continuity of refractor surfaces across a profile (Rucker, 2000).

Refraction tomography, a recent method of interpreting seismic refraction data (Hiltunen, et al., 2007), is designed to resolve velocity gradients and lateral velocity changes; enabling it to be applied in settings where conventional techniques fail. Instead of a refraction wave model a diving wave model is used. The method uses only first arrival time data and profile geometry as input. It uses a gridded, inversion technique to determine the velocity of individual 2-D blocks (pixels) within a profile and computes a best-fit velocity model by minimizing the difference between calculated and observed travel times. The method is easily applied and is well suited for

investigation of areas dominated by complex shallow structure, significant velocity gradients and variable topography.

### 4.2.1 Different Algorithms

During the past few years a number of refraction traveltime tomography algorithms has been developed. These algorithms are based either on a two-point ray tracing or a wavefront construction method (Zhang et al., 1998).

#### (i) Two-point ray tracing

One of the methods to compute the travel times of seismic waves propagating in 2-D layered structures with smooth variations of velocity inside layers is based on numerical ray tracing. Under numerical ray tracing we understand the numerical integration of ray tracing systems inside layers. This method is based on turning rays and solves a damped least-squares problem for both velocity and refractor depth.

The two point ray tracing algorithm (Cerveny, 1987; White, 1989; Stefani, 1995) is valid for smooth velocity structures. It is used to compute raypaths and traveltimes by ray tracing, ray bending or shooting rays. Respective programs are suitable for media characterized by relatively smooth slowness variation without pronounced vertical velocity contrasts. In the following the two-point ray tracing algorithm by White (1989) is described.

The linearized formulation of the travel time is presented as follows:

The travel time along a ray in a continuous medium whose velocity  $v_o(x)$  is

$$t(v_o(x)) = \int_{L_o} \frac{dl}{v_o(x)} \quad (4.15)$$

where  $L_o$  represents the ray path. If the velocity of the medium is perturbed by  $\delta v(x)$  such that  $v(x) = v_o(x) + \delta v(x)$ , then the perturbed travel time is

$$t(v(x)) = \int_L \frac{dl}{v(x)} \quad (4.16)$$

where  $L$  is the new ray path. The time through the perturbed medium can be expressed as an expression about  $v_o(x)$  as

$$t(v(x)) = tv_o(x) + \frac{\partial t}{\partial v} \Big|_{v=v_o} \delta v(x) + \frac{\partial t}{\partial L} \Big|_{v=v_o} \frac{\partial L}{\partial v} \Big|_{v=v_o} \delta v(x) + O[\delta^2 v(x)] \quad (4.17)$$

Using Fermat's principle which states that the travel time for the ray path is stationary (i.e.  $\partial t / \partial L | v = v_o = 0$ ), and discarding the terms of  $O[\delta^2 v(x)]$  we obtain

$$\delta \tau = t(v(x)) - t(v_o(x)) = \frac{\partial t}{\partial v} \Big|_{v=v_o} \delta v(x). \quad (4.18)$$

Differentiating equation (4.15) and substituting the result in (4.18),

$$\delta \tau = - \int_{L_o} \frac{\delta v(x)}{v_o^2(x)} dl. \quad (4.19)$$

Here the problem is formulated in terms of velocity instead of slowness.

If the medium is discretized into a grid of  $N$  cells, each with an associated slowness value  $v_j$ ,  $j = 1, \dots, N$  then (4.19) can be approximated by

$$\delta \tau = \sum_{j=1}^N \frac{\partial t}{\partial v_j} \delta v_j. \quad (4.20)$$

For a set of  $M$  rays, a linear system of equations is formed from (4.20)

$$\delta \tau = A \delta v, \quad (4.21)$$

where  $\delta \tau$  is the vector of travel time residuals ( $t_{observed} - t_{calculated}$ ),  $A$  is the Jacobian matrix  $\partial t_i / \partial v_j$ , and  $\delta v$  is the velocity perturbation vector.

### (ii) *Wavefront method*

The wavefront methods include a finite difference approximation to the eikonal-equation solution (e.g. Vidale, 1988; Qin et al., 1992; Hole and Zelt, 1995), analytical method (e.g. Vinje et al., 1993) and the shortest path ray tracing methods (e.g. Moser, 1989, 1991; Saito, 1989, 1990). Wavefront methods can simulate wave propagation in the entire model and find diffracted ray paths, head waves and ray-paths to the shadow zone. The method allows to calculate travel times and ray-paths on a large number of grids rapidly and accurately.



The finite difference calculation of traveltimes (Vidale, 1988) has been proved to be an accurate and efficient way to compute, on a regular grid, the traveltimes of first-arrival seismic waves through virtually any velocity structure.

Vidale (1988) presented a method that solves for first arrival traveltimes by a finite-difference solution to the eikonal equation

$$\left(\frac{\partial T}{\partial x}\right)^2 + \left(\frac{\partial T}{\partial z}\right)^2 = s^2(x, z), \quad (4.22)$$

where  $T(x, z)$  is the first arrival time for a seismic energy propagating from a point source through a medium with a slowness distribution of  $s(x, z)$ . Rather than solving for traveltimes along a raypath, the eikonal equation solution gives the travel times throughout the model.

In Vidale's method, the solution region is developed along an expanding square. He proposed the following scheme to solve equation (4.22):

For a source located at point  $A$  (Figure 4.15) the arrival times at the four points  $B_1, B_2, B_3$  and  $B_4$  can be computed by taking the product of the distance  $h$  and the average slowness between points  $A$  and  $B_i$ .

$$T_{B_i} = h \frac{(s_{B_i} + s_A)}{2} \quad (4.23)$$

Then the arrival times  $T_{C_i}$  at the four corner points can be computed with the following formulas:

$$T_{C_i} = T_A + \sqrt{2(h\bar{s}_i) - (T_{B_{i+1}} - T_{B_i})^2} \quad (4.24)$$

when  $i = 4$ ,  $T_{B_{i+1}} = T_{B_1}$ ,

and where  $\bar{s}_i = \frac{1}{4}(s_A + s_{C_i} + s_{B_i} + s_{B_{i+1}})$ ,  $T_A = 0$ , since it is the origin time of the source.

The grid points in Figure 4.15a are timed and now the ring of the field circle shown in Figure 4.15b is about to be timed. The open circles indicate points where the traveltimes were calculated.

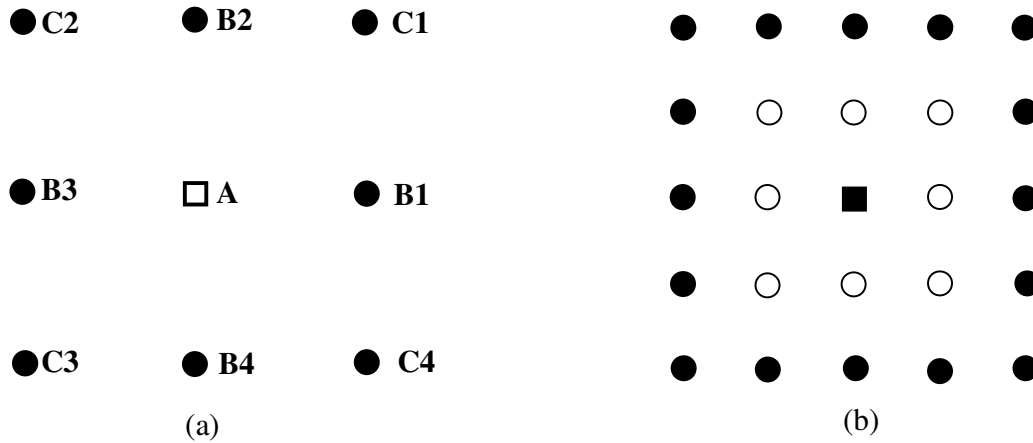


**Figure 4.15:** (a) Finite-difference mesh centred about source point  $A$ , where  $B_i$  and  $C_i$  for  $i = 1,2,3,4$  are to be timed. (b) The expanding square method (Vidale, 1988). Point  $A$  is the source point and the point shown as filled circles are about to be timed. The traveltimes at open circles are known (from Qin et al., 1992).

## 4.2.2 Basic Computational Steps

Implementing a refraction tomographic inversion method requires several steps. These steps include first arrival traveltimes picking, image plane parameterization, ray tracing and segmentation, residual time computation and velocity updating to minimize the error.

Picking of the first arrival times of certain seismic events recorded by receivers is the first step in the processing scheme. Picking these traveltimes of the events accurately plays an important role in the inversion. The next phase of the inversion is to image plane parameterization which involves discretizing the medium to be imaged into a grid of rectangular elements or cells. And defining a starting velocity model from first break picks and from prior geological and geophysical information.

The raytracing and segmentation phase involve ray tracing through an initial estimate of the velocity model, computing travel times and ray paths between the source and receiver location as

well as obtaining a ray segment in each cell crossed by a ray. After the determination of the predicted traveltimes and raypaths the residuals (the differences between observed (picked) and calculated (predicted) travel times) for each ray will be computed. Then the initial velocity model is adjusted in order to minimize the traveltime residuals. Figure 4.16 shows the main steps in the tomography inversion process.

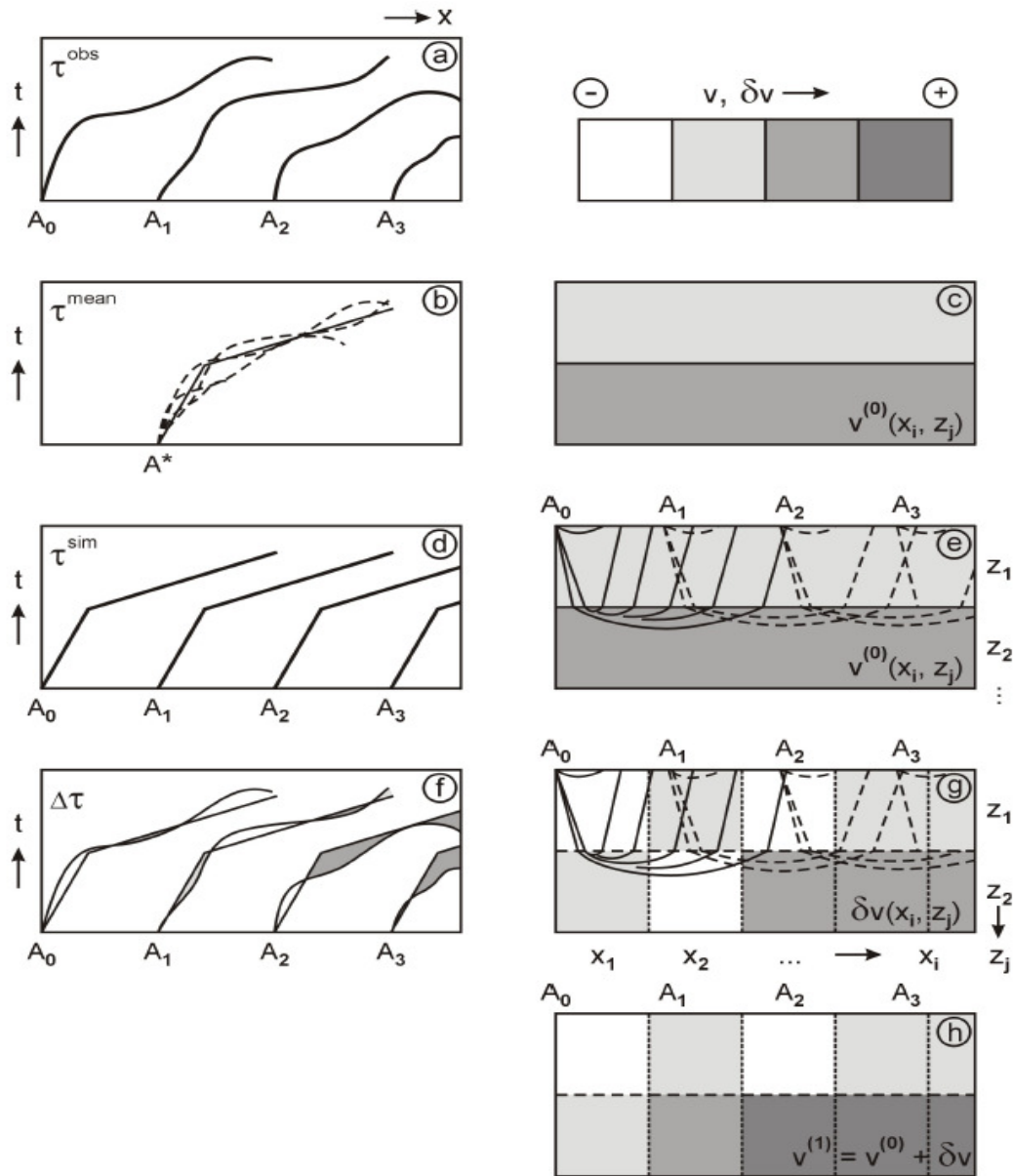


**Figure 4.16:** Typical computational steps in seismic refraction tomography: (a) Observational basis: Refraction travel time curves  $\tau_{\text{obs}}$  for overlapping spreads and a dense sequence of source points, (b) computation of simplified average travel time-distance curve  $\tau_{\text{mean}}$ , (c) derivation of a one-dimensional starting model  $v^{(0)}$  based on b), (d) computation of simulated travel-time curves

$\tau_{sim}$  for the actual model, (e) computation of rays for the actual model, (f) determination of traveltime residuals  $\Delta\tau=\tau_{obs}-\tau_{sim}$  (and checking of data fit), (g) application of an inversion technique to convert travel-time residuals  $\Delta\tau$  into corrections  $\delta v$  of the actual velocity model, (h) updating of the actual velocity model  $v(1)=v(0)+\delta v$ , or more generally,  $v(n+1)=v(n)+\delta v$  for the next iteration starting again with d) (Rabbel, 2006).

### 4.3 S-wave Method

A shear wave is a body wave in which the particle motion is perpendicular to the direction of propagation. Those waves having energy polarized to particle motion in the vertical plane (in relation to the propagation direction) are called vertically polarized shear waves (SV-wave) and those having energy polarized to particle motion in the horizontal plane (in relation to the direction of propagation) are called horizontally polarized shear waves (SH-wave). SH-waves have no vertical component and therefore travel the entire path from source to receiver as shear waves, but recorded SV-waves commonly start as P-waves at the source and are converted to SV-waves by reflection along the way. The SH-wave data are simplified in that SH waves convert only to SH upon reflection and transmission unlike SV propagation which is coupled with P. Because of this property of the SH-wave most of S-wave surveys have concentrated on the generation and recording of SH-waves.

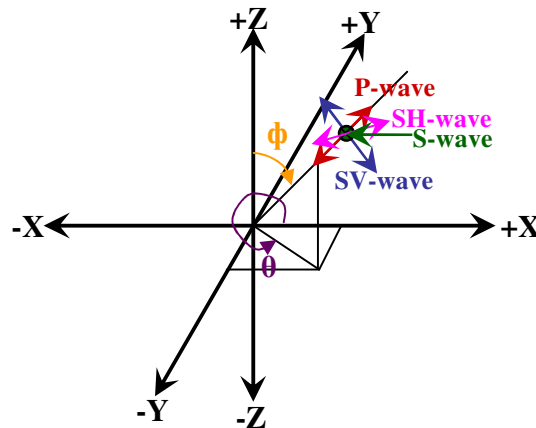


**Figure 4.17:** A diagram showing P-, SV-, and SH-waves in the X, Y, Z coordinates.

Nearly all seismic exploration is carried out with P-waves. But recently, interest has been growing in near-surface applications of shear-waves (especially SH-waves). Their use in shallow reflection studies shows good promise to make a contribution to near-surface studies. S-waves carry different information than P-waves, because they depend on different elastic properties (see

equations 3.15 and 3.19). The shear modulus  $\mu$  is most important in engineering studies; it can provide useful information on subsurface formation rigidity. If both P- and S-wave velocities can be measured then we have a source of additional information about the physical parameters of the layers and consequently about their lithological characteristics such as porosity, pore filling and facies (see section 3.5).

S-waves have increased resolution because of their lower velocities and consequently shorter wavelengths compared with P waves. For example S-wave velocities in sediments are often a factor of 4 to 6 lower than P-wave velocities. This means the S-wave length is 4 to 6 times shorter than the P-wave length which results in a much higher resolution for subsurface layering. This remarkable velocity difference (Table 3.1) provides an important advantage of S-wave reflection surveys in characterizing near-surface structures.

Near-surface reflection surveying using S-waves contributes valuable information to engineering and environmental studies. It is a powerful tool for delineating near-surface geological structures, can provide accurate soil stratigraphy, near-surface faulting, void detection, bedrock topography, channel identification and estimation of geotechnical properties of sediments. The use of shallow S-wave reflections has not yet been widespread, but a few examples can be found in the literature: Pullan et al. (1990), Hasbrouck (1991), Woolery et al. (1996), Carr et al. (1998), Inazaki (2000), Pugin et al. (2004), and Polom et al. (2008).

### **4.3.1 S-wave Generation and Recording**

An S-wave survey requires a reliable energy source with sufficiently high seismic efficiency. S-waves can be generated using different sources like explosion, horizontal hammering and an S-wave vibrator. For example in horizontal hammering a plate is pressed hard into the ground and one edge is struck by a horizontal blow; this horizontal force equals the shearing stress. In the case of an S-wave vibrator unlike with a P-wave vibrator (section 4.1.2) the reaction mass moves horizontally and not vertically; the force is transferred to the ground in the form of horizontally shearing stress.

In this work a small S-wave vibrator, the Electro-dynamic S-wave vibrator (ELViS 4), was used as S-wave seismic source. This S-wave vibrator is developed by LIAG Institute (Polom, 2005). A photograph of the S-wave vibrator is shown in Figure 4.18a. This device works in a frequency range of 20 – 500 Hz. The main parts of this vibrator are displayed in Figure 4.18b. It consists of strong permanent magnets (preferably Neo-Delta magnets) and transformer units. The

transformer units are inverted to create an alternating magnetic field. Due to the changing magnetic field the mass moves back and forth; that generates a shearing stress to the ground.

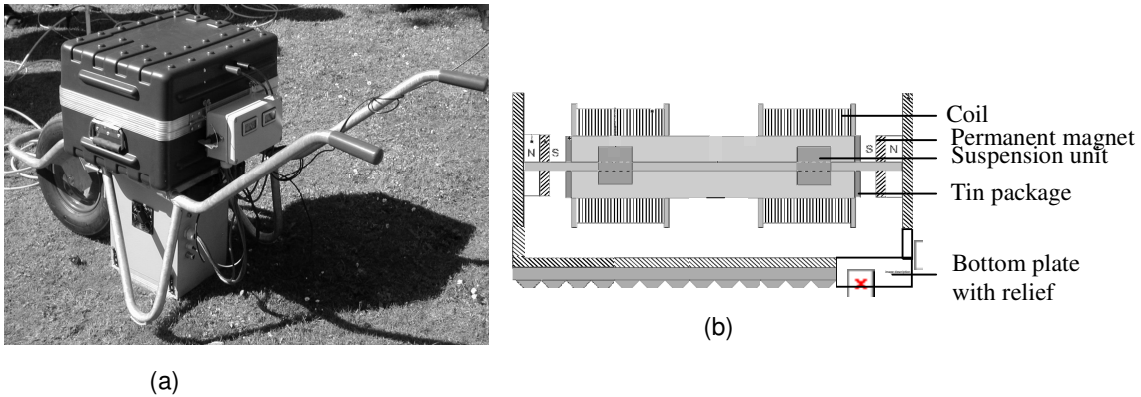


**Figure 4.18:** S-wave Vibrator. (a) Photo of electro-dynamic S-wave vibrator (ELViS 4).  
(b) The main parts of LIAG S-wave vibrator.

For S-wave data recording a horizontal geophone which detects the horizontal movements is required. For such kind of geophone the coil is horizontally oriented. Conventional fieldwork for near-surface application is time consuming and costly because it requires a dense planting of geophones. To increase the speed and efficiency of shallow seismic S-wave data recording and decrease the acquisition costs S-wave land streamer is developed (Inazaki, 1992, 1999). The S-wave land streamer used for this survey was built by LIAG Institute (Polom et al., 2007). The main features of the land streamer are similar to those of the P-wave land streamer (see section 4.1.2) except that the vertical geophones are replaced by horizontal geophones (Figure 4.8).

It is very difficult to generate S-waves without simultaneously generating P-waves. A simple method is developed for separating the two wave types, CMP stacking (Helbig, 1987; Hasbrouck, 1991). SH-wave records require two shots, striking the source in opposite directions ( $180^\circ$ ) perpendicular to the seismic line; which generates both P- and SH-waves. If we subtract the two records P-wave components cancel out and the sum of the two SH-components remains. Figure 4.18 shows S-wave traces from a single shotpoint one from the right and one from the left and the sum of the two shots from the survey area.

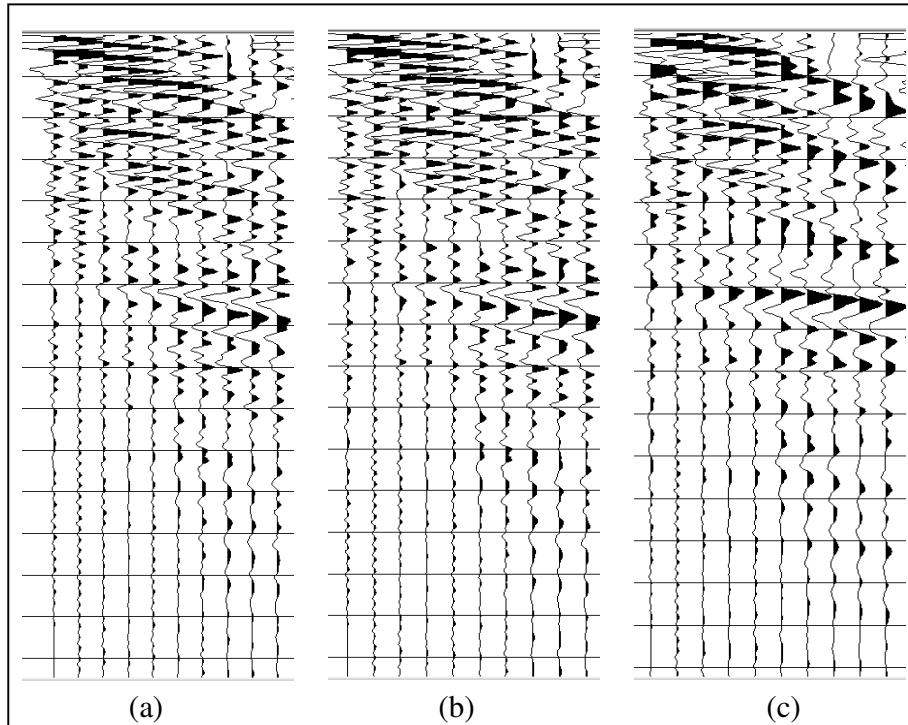


**Figure 4.19:** S-wave traces, (a) right shot, (b) left shot, (c) subtraction of the two shots.

### 4.3.2 S-wave Data Processing

S-wave data processing is similar to P-wave processing (section 4.1.2) in many regards, but there are some important differences. For noise attenuation and therefore improvement of the signal to noise ratio the same measures are available as for P-wave seismics.

The S-wave frequencies are generally a little lower than the P-wave frequencies and consequently differ less from the noise frequencies; this makes filtering more difficult. The noise wavelengths and the apparent wavelengths of the signals are very similar in many parts of the seismogram which makes the choice of an effective wavelength filtering difficult. Deconvolution and (f, k) filtering can be applied to compensate the above mentioned short-comings. Deconvolution restores the impaired parts of the spectrum to their original form and reproduces the output amplitudes and also attenuates noises such as multiples, surface waves and interspersed technical frequencies. (f, k) filtering helps to clear the noises (the Love waves ) from the seismogram.

S-wave static correction calculation is not simple like that for P-wave. The picking of S-wave first arrivals is impeded by the earlier weak P-wave arrivals. The increase of velocity occurring in comparatively moderate jumps makes the choice of an appropriate correction refractor velocity problematic. Steps such as eliminating uncertain first arrivals, determining lateral refractor

velocity variations and calculating the intercept time require more sophistication and time. These all make refraction-based static corrections not applicable for S-wave data. Besides the lateral velocity variations are much less important for S-waves than for P-waves. Consequently, static corrections become a minor issue for processing S-wave data.

Due to the lower velocities, S-wave reflections exhibit considerably larger normal moveout times than P-wave reflections and require correspondingly larger dynamic corrections for the stacking procedure.

For the NMO time from equation 4.9, we have

$$\Delta t = \frac{x^2}{2V^2 t_o}$$

Assuming a  $V_p/V_s$  ratio of 2 ( $V_p = 2V_s$ ) and keeping the interval  $x$  between the source and the geophone position constant, then for an S- and P-wave reflected from the same horizon we have ( see Figure 4.20)

$$\Delta t_s = 2\Delta t_p \tag{4.25}$$

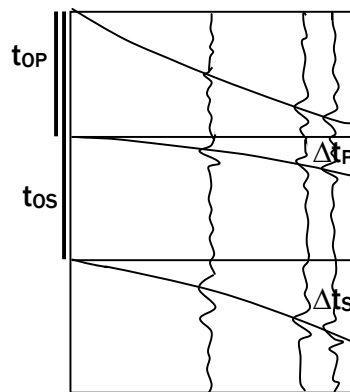


**Figure 4.20:** Two-way travel times ( $t_o$ ) and NMO-times ( $\Delta t$ ) of a P- and S-wave reflection from the same horizon, where  $V_p = 2V_s$ .

In the general case the P-wave processing method (NMO correction, CMP stacking, migration) discussed in section 4.1.2 is applied also for the processing of S-wave seismograms.



## 4.4 Surface Wave Method

The surface wave is a seismic wave which travels near the surface of the earth. It includes Love and Rayleigh waves. Surface waves, especially Rayleigh waves are very useful for estimating the S-wave velocity of near-surface materials. Rayleigh waves travel along a free surface, such as the earth-air interface. They are the result of interfering P- and SV-waves. The particle motion of Rayleigh waves moving from left to right is elliptical in a counterclockwise (retrograde) direction. The motion is constrained to the vertical plane consistent with the direction of wave propagation (Babuska and Cara, 1991).

The Rayleigh wave velocity is determined by the material properties, primarily by the shear wave velocity but also to a lesser degree by the compression wave velocity and by the material density of the subsurface. It is representative of the material stiffness over depths where there is significant particle motion. For the case of a solid homogenous half-space (and a Poisson ratio of  $\frac{1}{4}$ ), the Rayleigh wave travels with a velocity of approximately  $0.9194V$ , where  $V$  is the S-wave velocity in the half space (Sheriff and Geldart, 1982).

Surface wave methods are non-destructive and non-intrusive methods and provide ways to obtain shallow subsurface details. There are two primary surface wave techniques. These are the spectral analysis of surface waves (SASW) and multi-channel array surface wave (MASW) methods. The basis of these techniques is the dispersive characteristic of Rayleigh waves when travelling through a layered medium.

The SASW method is a seismic method that uses the dispersive characteristics of Rayleigh waves to determine the variation of the S-wave velocity of layered systems with depth (Stokoe et al., 1994). Dispersion refers to the variation of Rayleigh wave phase velocity with frequency or wavelength. The method is based on the principal that surface seismic waves of high frequency propagate only in near-surface layers, and surface waves of low frequency propagate at different velocities if stiffness varies with depth.

An SASW field procedure consists of two (or four) geophones close together and any mechanical source of high-frequency energy. An expanding receiver spread is used to avoid near field effects associated with Rayleigh waves and the source-receiver geometry is optimized to minimize the

body wave signal. The receiver spread is used to make field measurements of surface wave phase velocity at numerous wavelengths and using these measurements to calculate a dispersion curve. A dispersion curve displays the variation in surface wave velocity with wavelength (frequency). After a dispersion curve is calculated from the field data, forward modelling is used in the laboratory to evaluate the shear wave velocity profile.

The MASW method was first introduced by Park et al. (1999) to investigate the near-surface materials for their elastic properties. It uses a multi-channel array, which makes it possible to distinguish the fundamental-mode Rayleigh wave from higher modes and body waves. The fundamental framework of the method is based on the multichannel recording and analysis approach long used in seismic exploration surveys. Unlike the conventional SASW method, multi-station recording permits a single survey of a broad depth range and high levels of redundancy with a single field configuration. The acquired data are first analyzed for dispersion characteristics and, from these the shear-wave velocity is estimated using an inversion technique.

## 5. Field Data Description and Analysis

Seismic reflection data for this study were acquired in two separate campaigns in the Ellerbeker Rinne area (Figure 2.1). The two campaigns took place in the year 2005 and the year 2006. In the first campaign standard reflection data was collected (profile 1). In the second campaign sets of shallow P- and S-wave reflection data (profile 2) were acquired for obtaining detailed information of the near surface area. The line parameters and the corresponding CMP points are summarized in Table 5.1.

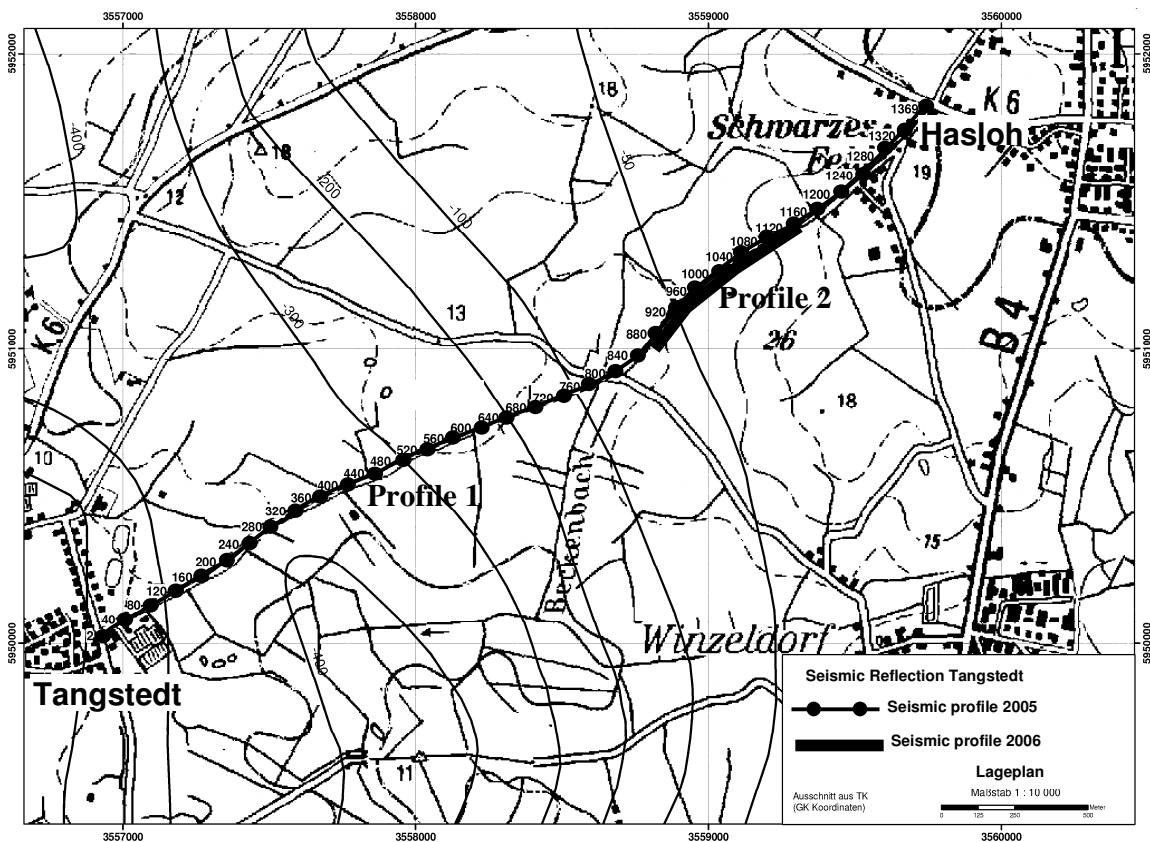


**Figure 5.1:** Profile map and CMP location of the survey area, profile 1 from the 2005 campaign and profile 2 from the 2006 campaign (for details of profile 2 see also Figure 5.15).

Profile	Acquisition time	Profile geophone (PG)		Vibration points (VP)		CMP points		Profile length (m)	Corresponding CMP's	
		first	last	first	last	first	last		first	last
Tangstedt P-wave 2005	30/05-07/06/2005	1	684	1	685	2	1369	3415	1152	881
Tangstedt P-wave 2006	29/06/2006	0	720	1	648	25	1368	684	25	1368
Tangstedt S-wave 2006	26-28/06/2006	0	720	1	720	1	1440	720	25	1368

**Table 5.1:** Acquisition Parameters for 2005 and 2006 data. The sum of geophone number (PG) and the vibration point number (VP) gives the CMP point number. The location of PG or VP is at  $CMP/2$ .

## 5.1 P-wave Seismic Reflection Data of 2005

During the first campaign in the year 2005 P-wave reflection data were collected along a profile between Tangstedt and Hasloh called profile 1 (Figure 5.1). The profile was originally planned for standard seismic reflection survey (~500m target depth) for locating a buried valley and to define an aquifer (BurVal Working Group 2006). Here the data are used for the refraction tomography method in a near-surface application.

The profile is 3,415 m long and runs in west east direction. For the seismic source a small vibrator MHV2.7 of LIAG-Institute was used (Bram 1997). The signal is generated with a sweep frequency of 50-200 Hz. The field sampling interval was 1 ms and the field recording length was 1.5 s. Four shots were vertically stacked per each shot point to improve the signal-to-noise ratio. For comparing the signal form to an impulse source a hammer blow was done for every 48<sup>th</sup> point.

The data were acquired using a fixed spread with single 20 Hz geophones. A spacing of 5 m was employed for both the sources and receivers, thus yielding a common depth point (CMP) spacing of 2.5 m. The survey was set up with split-spread mode with 120 active geophones. There were a total of 683 shots and a nominal fold of 96. Maximum source-receiver offsets are 600 m. The P-wave data was recorded with a seismic measuring apparatus Geometrics Geode. For the parameters see also Table 5.2.

Seismic source	Vibrator (MHV 2.7 P-wave vibrator)
Recording instrument	Geometrics Geode (Geometrics Inc., Tulsa OK, USA), 24-channel each
Receiver	SM 4/7 (20 Hz)
Number of geophones	120
Geophone spacing	5 m
Shot spacing	5 m
CMP spacing	2.5 m
Maximum offset	600 m
Maximum fold	96
Sweep frequency	50-200 Hz, 10 s length
Recording length	1.5 s
Sample interval	1 ms
Polarisation	SEG standard
Data format	SEG-2

**Table 5.2:** Acquisition Parameters profile Tangstedt P-wave 2005 (Rumpel et al., 2005b).

The data is processed with commercial seismic processing software called ProMAX (Landmark Corp., Version 1998.6). The reflection-processing flow is presented in Table 5.3. The stacked section after migration and a time-to-depth conversion performed is shown in Figure 5.2. This depth section lacks information at the near surface range ( $\sim < 50$  m). To fill this lack of information arrival times of refracted waves – unwanted signals in the reflection survey – are analysed in the following section by the refraction tomography method with the aim to complement the stacked seismic section by a detailed velocity model for the near-surface area.

	Processing Steps
Prestack Processing	Data reformat (SEG-2 to ProMAX format)
	Assignment of field geometry
	Quality control (elimination of bad traces)
	Spherical divergence correction ( $1/(t \cdot v^2)$ )
	Mute (elimination of surface waves)
	Trace equalization
	Zero phase spiking deconvolution
	Automatic gain control (400 ms)
	Air blast attenuation
	Static correction to floating datum
	Dynamical correction (NMO-correction)
	Residual static correction
	CMP-Stack
Poststack-Processing	Static correction to final datum (0 m NN, 1600 m/s)
	Trace equalization
	FX Deconvolution (50-250 Hz)
	Steep dip FD time migration (single velocity function)
	Time/depth conversion

**Table 5.3:** Processing flow profile Tangstedt P-wave 2005 (Rumpel et al., 2005b).

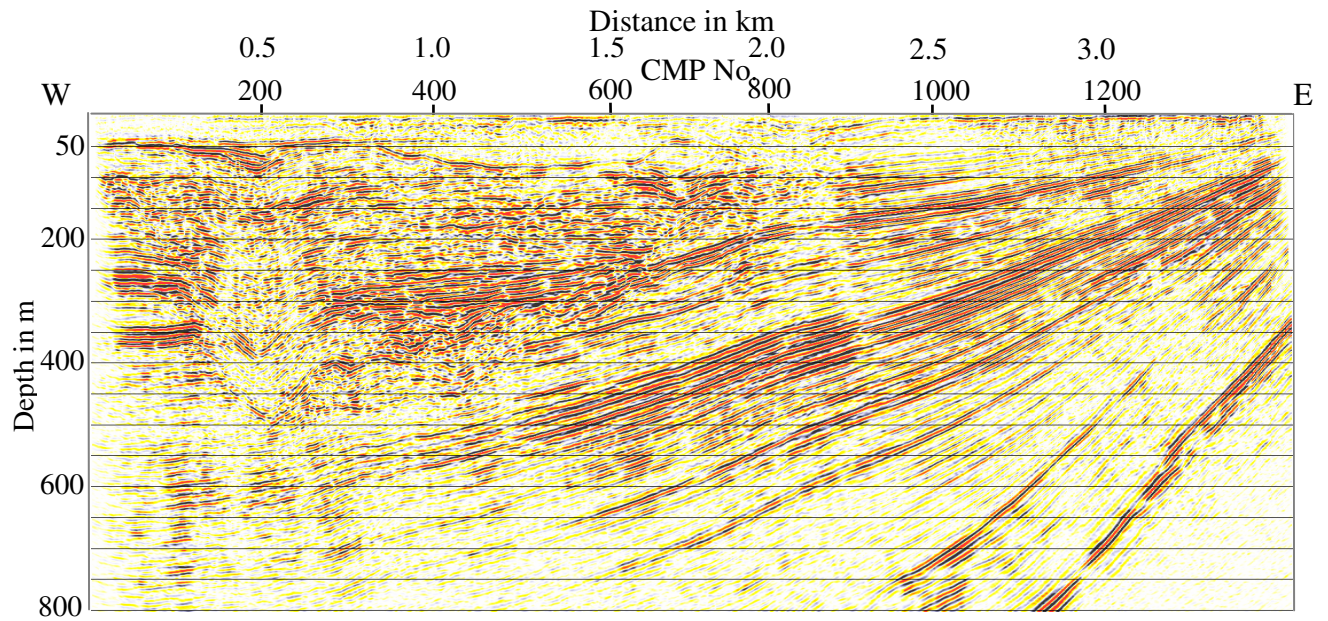


**Figure 5.2:** Stacked depth section profile Tangstedt P-wave 2005(Rumpel et al., 2005b).

### 5.1.1 Refraction Tomography Result from the Field Data

In an attempt to define the near-surface velocity model the refraction tomography method is employed on the first arrivals records from the seismic reflection data of 2005 (section 5.1). A manual picking was performed to determine the initial estimates of first arrival times for ~81,000 traces. Time picking was made at the positive peak of the first arrivals because the source wavelet is at zero phase as the source is of type vibroseis. A total of 46,198 picks from 683 shots were made; the remaining 30% of the shots were not pickable because of noise and lack of accuracy. The energy of most of the shots was sufficient to observe the refracted P-wave arrivals over the observation distance (offset) of maximum ~300 m. Figure 5.3 shows a typical example of a shot gather with the picked first arrivals.

All operations, from the first-break picking to the reconstruction results, were realized using ProMax (Landmark Corp., Version 1998.6) seismic processing software. The software applies the turning ray tomography (TRT) algorithm (section 4.2.1). TRT employs first arrival turning rays (continuously refracted direct rays) from a conventional acquisition geometry to iteratively solve for velocity in the near surface between sources and receivers (Stefani, 1995). Because ray coverage decreases with increasing depth, the reliability of velocity models obtained with TRT also decreases with depth (Stefani, 1995). Generally, the velocity distribution may be considered reliable for depths of 1/5 of the maximum source-receiver offset.

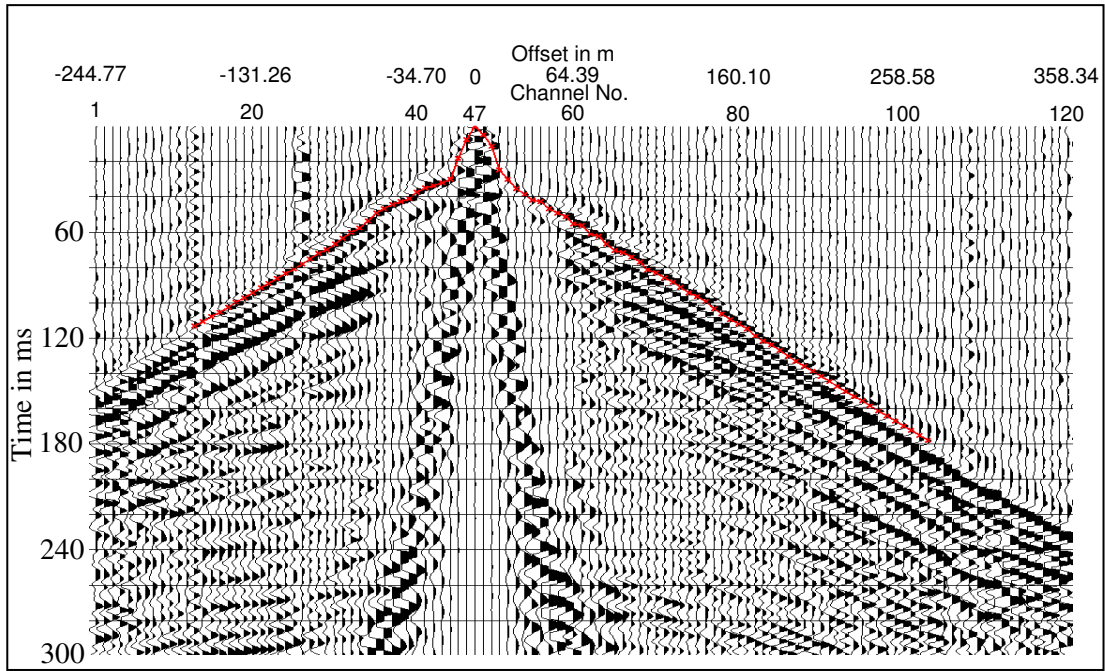


**Figure 5.3:** Shot gather with the picked first arrivals (red line).

To start the inversion process an initial velocity model is needed which is used to trace the rays. The starting interval velocity model (Figure 5.4) is defined by averaging and smoothing the first break picks using the flat layer assumption of refracted arrivals. In the starting interval velocity model the velocity is increasing with depth and has no lateral velocity variation. The velocity increases from 1372 m/s at the top layer to 1868 m/s at the bottom layer for the depth of the first 100 m.

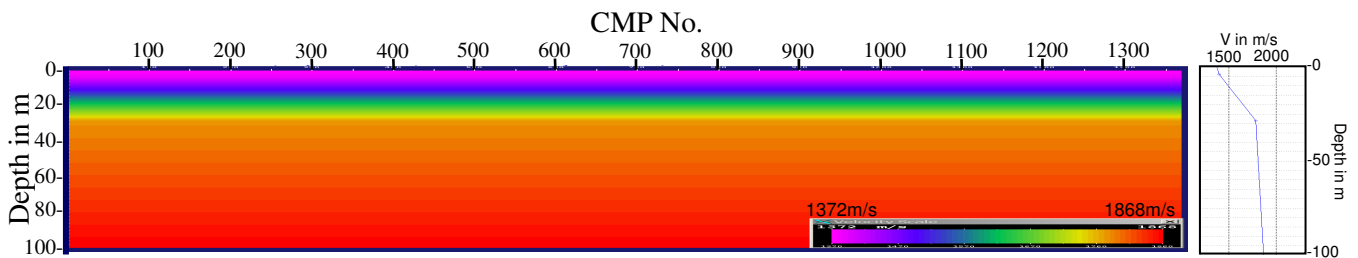


**Figure 5.4:** Starting interval velocity model.

Rays are traced through the starting interval velocity model in a shooting approach from the source to the receiver. The starting model produces the predicted travel times. It is also used to produce the ray paths which are used for tomography inversion. The inversion method is based on an iterative solution of the linearized problem, and allows for determination of continuous velocity variations as well as geometry of sub-horizontal interfaces.



The turning ray tomography discretizes the starting interval velocity field into a grid of small constant gradient cells. The differences between picked and predicted travel times, the residual travel times, for each ray are then computed. The initial velocity model is adjusted in order to minimize the travel-time residuals. After adjustment of the velocity model, a new travel-time is calculated. Figure 5.5 shows partly the picked travel times and the predicted travel times along the profile.

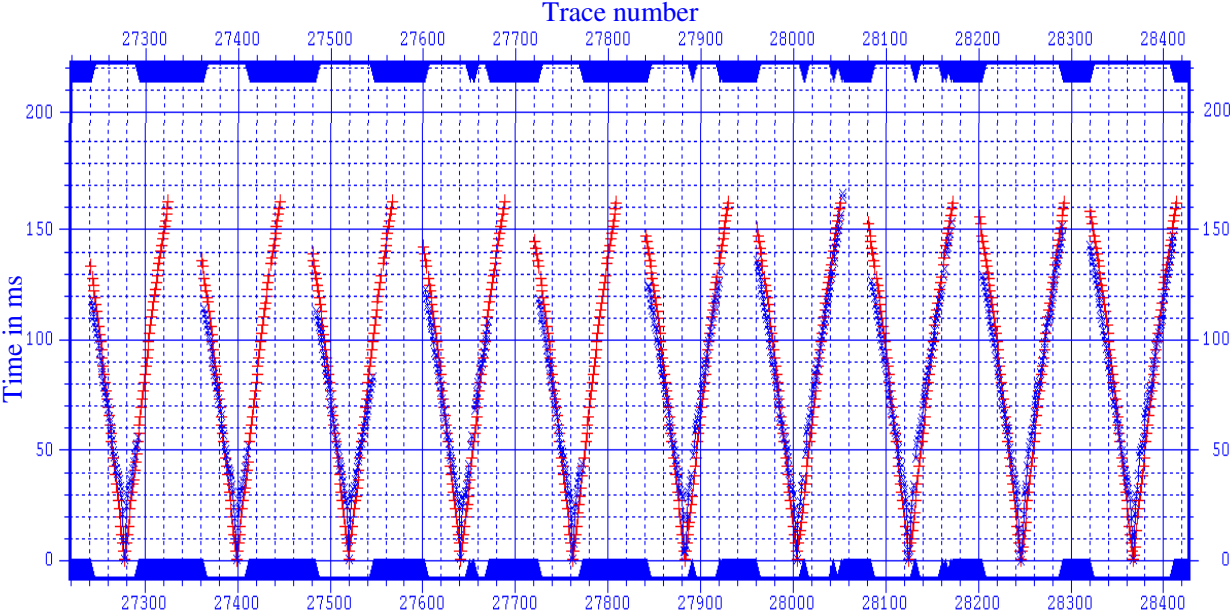


**Figure 5.5:** The picked (blue) and the predicted (red) travel times.

The inversion software calculates the interval velocity using the travel time deviations between picked travel times and those predicted for a starting model (the residual travel times). After some tests the tomographic inversion is performed with a horizontal cell size of 3 m and a vertical cell size of 2 m. The inversion is rerun three times in order to minimize the residual travel time and there were 8 iterations for each inversion over the range of eigenvalues from 1 to 0.2. The criterion used for estimating the reliability of the tomogram is the RMS value of travel-time residuals. The RMS residual between calculated and all observed first-arrival times is ~8 ms.

The interval velocity model obtained by tomographic inversion (Figure 5.6) has interval velocities that vary both laterally and vertically. Although it is difficult to see sharp, high contrast boundaries the velocity field can be approximated into three layers. In the upper ~10 m of the velocity field, velocities are low, mostly ranging from ~450 m/s to ~1000 m/s and there are some larger gradient (anomalies) to the east. The velocities vary from ~1300 m/s to ~1600 m/s at a depth of about 12–30 m. From ~30 m up to ~50 m the velocity variation is in the range of ~1800 to ~2400 m/s and there is also a strong lateral variation within this depth.

As it can be seen from the ray coverage density (Figure 5.7) no information is offered below ~50 m depth. One can also observe some features (vertical structures) in the interval velocity field along the profile. In order to understand these structures whether they are artefacts or real geologic features synthetic data sets are tested in the following section.

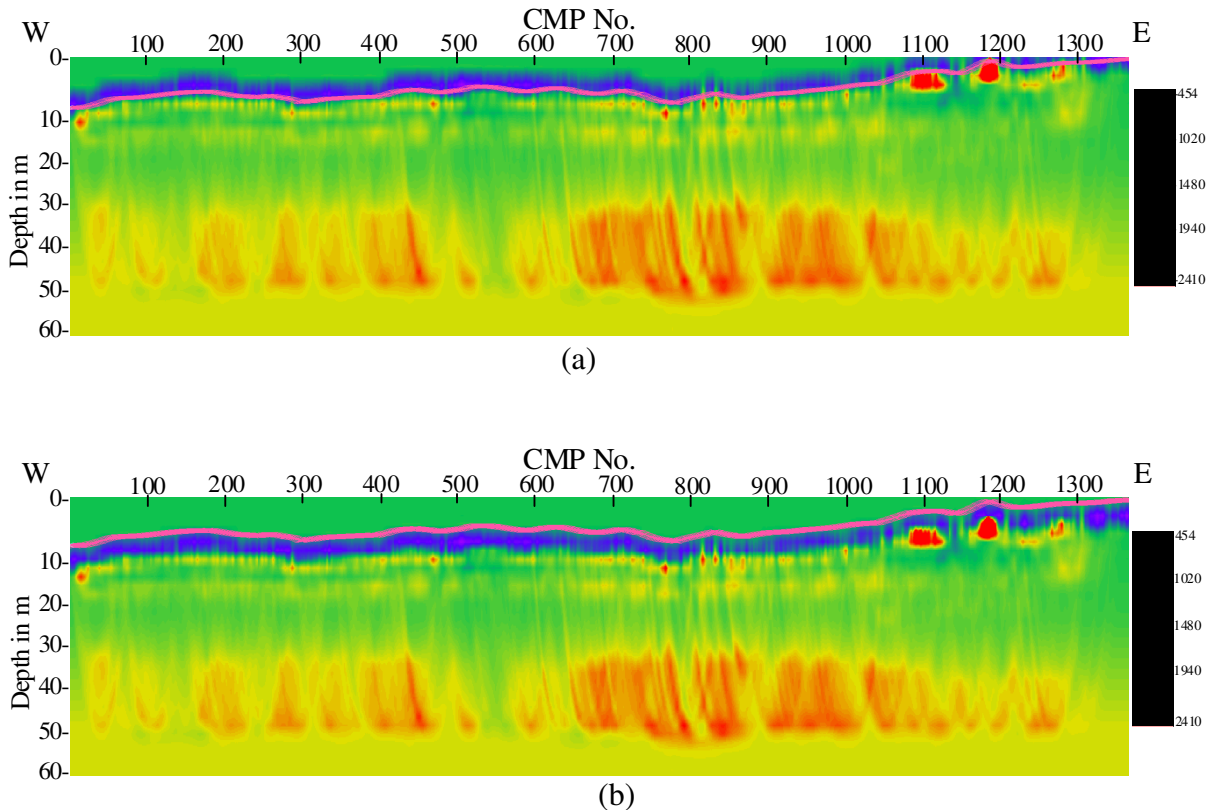


**Figure 5.6:** Velocity field obtained from the tomography inversion. Pink line is the elevation. Figure (a) shows the 4 m misfit between elevation and the tomography result. The reason for this discrepancy is unclear; may be it is due to the mathematical calculation in the software. Figure (b) shows the situation after the shift was made to the tomography result in order to correct this 4 m difference.

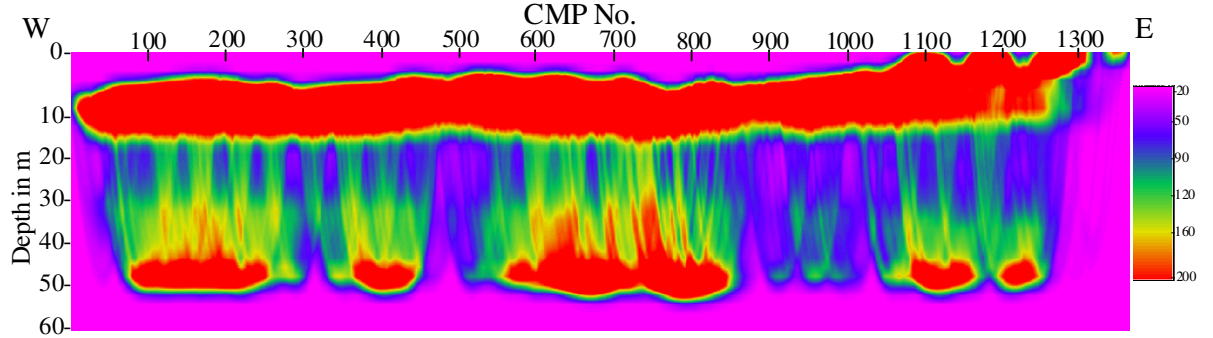


**Figure 5.7:** Ray density from the tomographic inversion.

### 5.1.2 Checking the Method with Synthetic Data

In order to test the effect of the acquisition geometry on the resulting velocity field synthetic data sets were generated using a finite difference modelling. The input velocity model (Figure 5.7), for producing the synthetic data, is derived based on the Vertical Seismic Profiling (VPS) data from the study area (Rumpel et al. 2005a). The model includes a velocity of 350 m/s for the weathering layer, a velocity ranging from 700 m/s-1400 m/s for the second layer, 1400 m/s-2200 m/s for the third layer and a constant velocity of 2200 m/s for the bottom layer with a total depth of 100 m. The model has no lateral velocity variation.

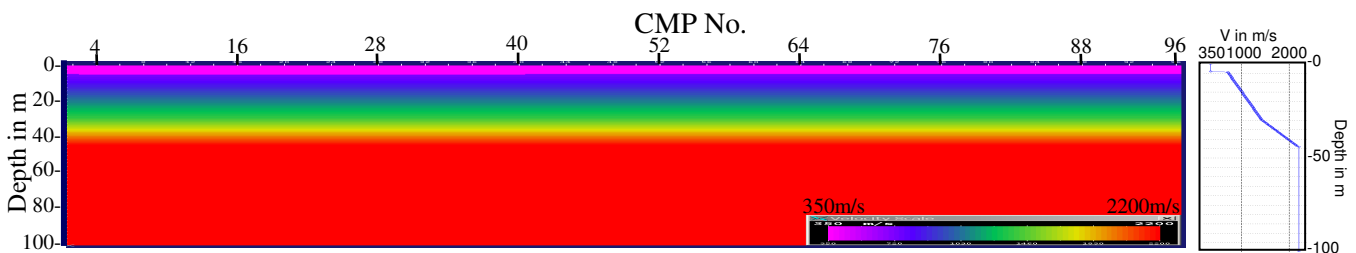


**Figure 5.8:** The input velocity model for producing a synthetic seismogram.

The source wavelet used for synthetic trace generation consisted of a maximum frequency at 200 Hz with a peak amplitude at 80 Hz. The data were calculated with a sampling rate of 1 ms for 350 ms. To avoid the reflections from the limits of the model, absorbing boundary conditions were chosen. With these parameters two acquisition geometries were designed: a first data set with 48 receivers and 24 shots and a second data set with 48 receivers and 48 shots.

For the first data set the geometry has 48 receivers with 5 m spacing and 24 shots, i.e., shot points for every second geophone. From the above input velocity model (Figure 5.8) and the geometry, the synthetic seismic traces are generated using finite difference modelling. A total number of 1152 traces with 24 shot gathers were obtained. Figure 5.9 shows one sample shot with the first break picks.

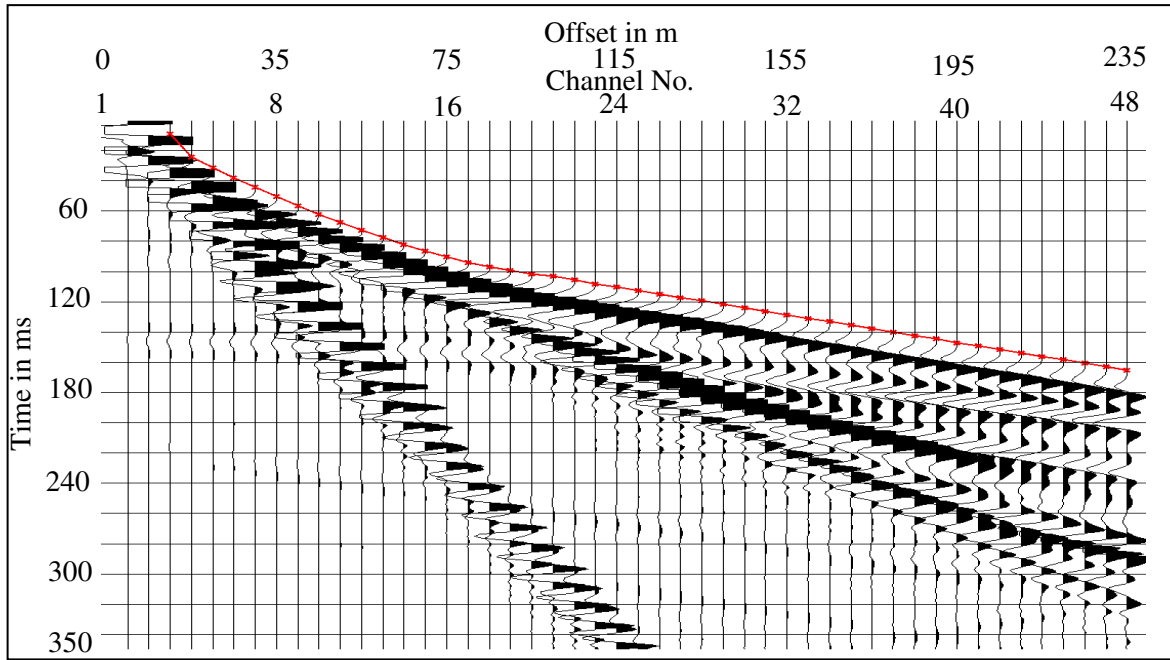


**Figure 5.9:** Sample of synthetic traces with the first break picks (minimum phase wavelet).

The travel times of the first arrivals of the synthetic data were picked and from these picks the starting interval velocity model (Figure 5.10) for the inversion is created. The interval velocity ranges from 850 m/s on the top layer to 2387 m/s to the bottom layer for the depth of the first 100 m.

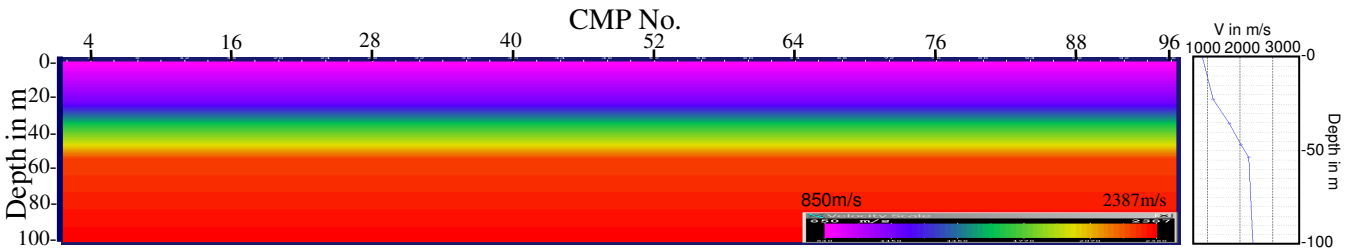


**Figure 5.10:** Starting interval velocity model for first test data set.

After inverting data set one an interval velocity model is obtained (Figure 5.11). In the interval velocity field the velocity is increasing with depth and there is also a slight lateral velocity variation. The velocity ranges on average from 640 m/s to 2060 m/s for the first 40 m depth. The results obtained from the inversion are influenced by the initial model but they are not smooth having some holes in regular intervals laterally. The ray-tracing coverage diagram (Figure 5.12) also reveals the holes or areas with low ray density which is most likely due to the source-receiver geometry.

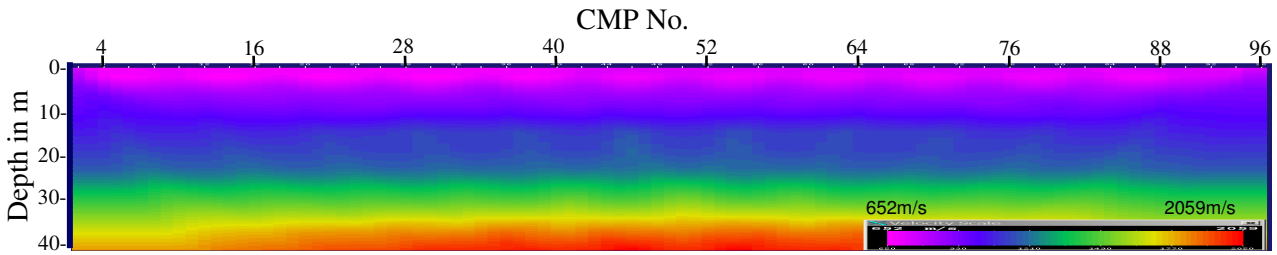


**Figure 5.11:** Velocity field from tomographic inversion of data set one.

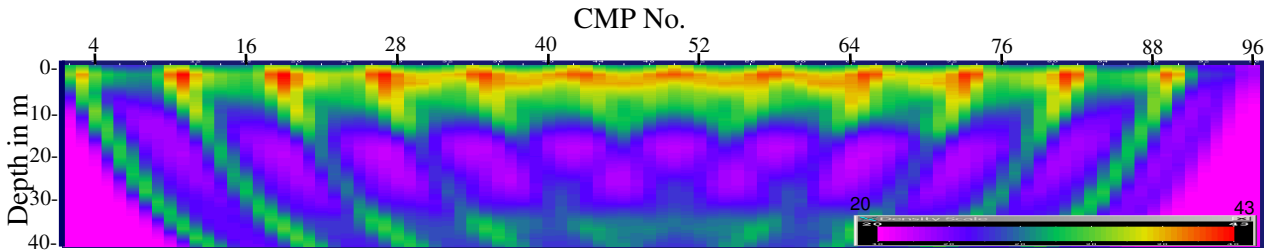


**Figure 5.12:** Ray density from the tomographic inversion of data set one.

For the second data set the geometry has 48 receivers with 5 m spacing and 48 shots i.e. shot points at every geophone. From the input velocity model (Figure 5.8) and the new geometry, 2304 synthetic traces from 48 shot gathers were generated. From these synthetic travel time picks the starting velocity model (Figure 5.13) for the tomographic inversion is created. The velocity ranges from 881 m/s on the top layer to 2367 m/s to the bottom layer for the depth of the first 100 m.

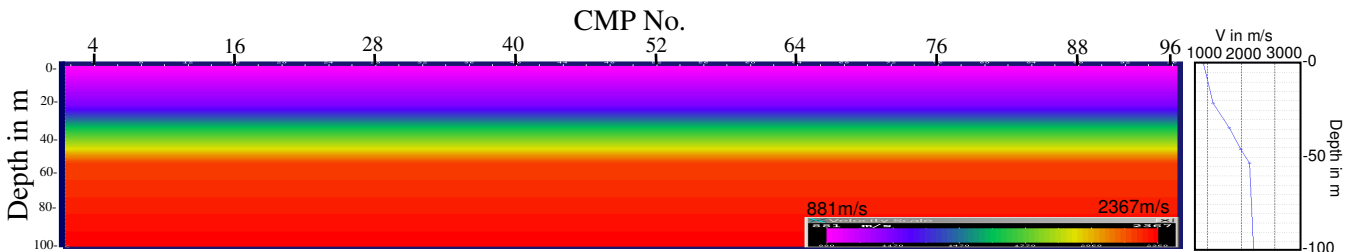


**Figure 5.13:** Starting model from turning ray velocity for the second test data set.

The velocity model (Figure 5.14) obtained by inverting the second data set shows the velocity ranging on average from 725 m/s to 2075 m/s for the first 40 m in depth. It has only very slight lateral velocity variation and reveals a smooth velocity field; some slight velocity variation only occurs at the edge where data coverage is poor. The ray-tracing coverage diagram (Figure 5.15) also reveals a smooth ray density distribution which is the result of the relatively dense source-receiver geometry.

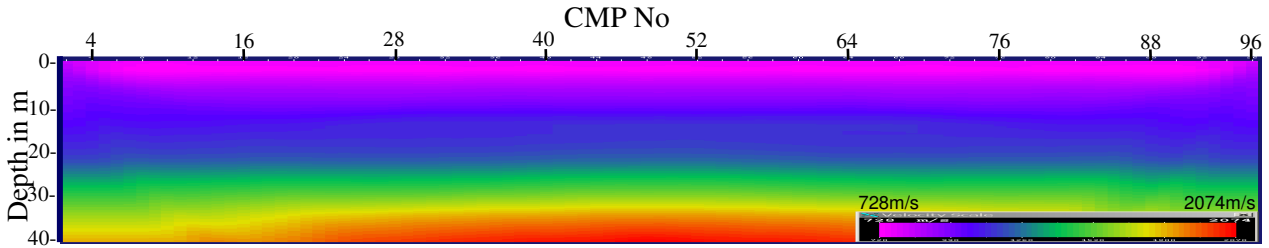


**Figure 5.14:** Velocity field from tomographic inversion of data set two.

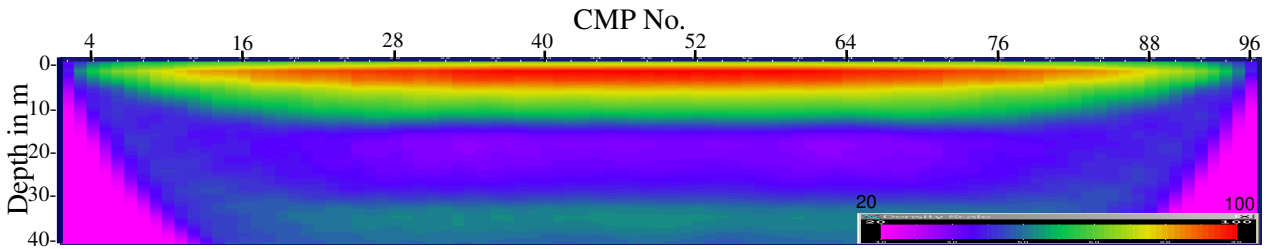


**Figure 5.15:** Ray density from the tomographic inversion of data set two.

The results obtained by both acquisition geometries are qualitatively equivalent although they have some essential difference. After inverting both data sets the interval velocity models (Figure 5.10 & 5.13) generally match to the input velocity model (Figure 5.8). On the other hand, the velocity field from the first data set has some unsmoothed structures or holes which is the result of the acquisition geometry whereas in the second data set such effects are not observed. This points out that the vertical structures or holes in tomographic inversion may result from the field data layout (section 5.1.1) along the profile, i.e. may be artefacts due to the acquisition geometry.

## 5.2 Shallow P and S-wave Seismic Reflection Data of 2006

Data collection during the May 2006 (Figure 5.16) focused on very shallow subsurface P- and S-wave seismic reflection with high resolution. The specific objective of this investigation is firstly to image the very near surface structures and to compare P- and S-wave reflection data in order to show their potential for delineating near surface lithology. Secondly to constrain and presumably verify the first arrival travel time tomography results (see section 5.1) from the 2005 conventional P-wave reflection data.

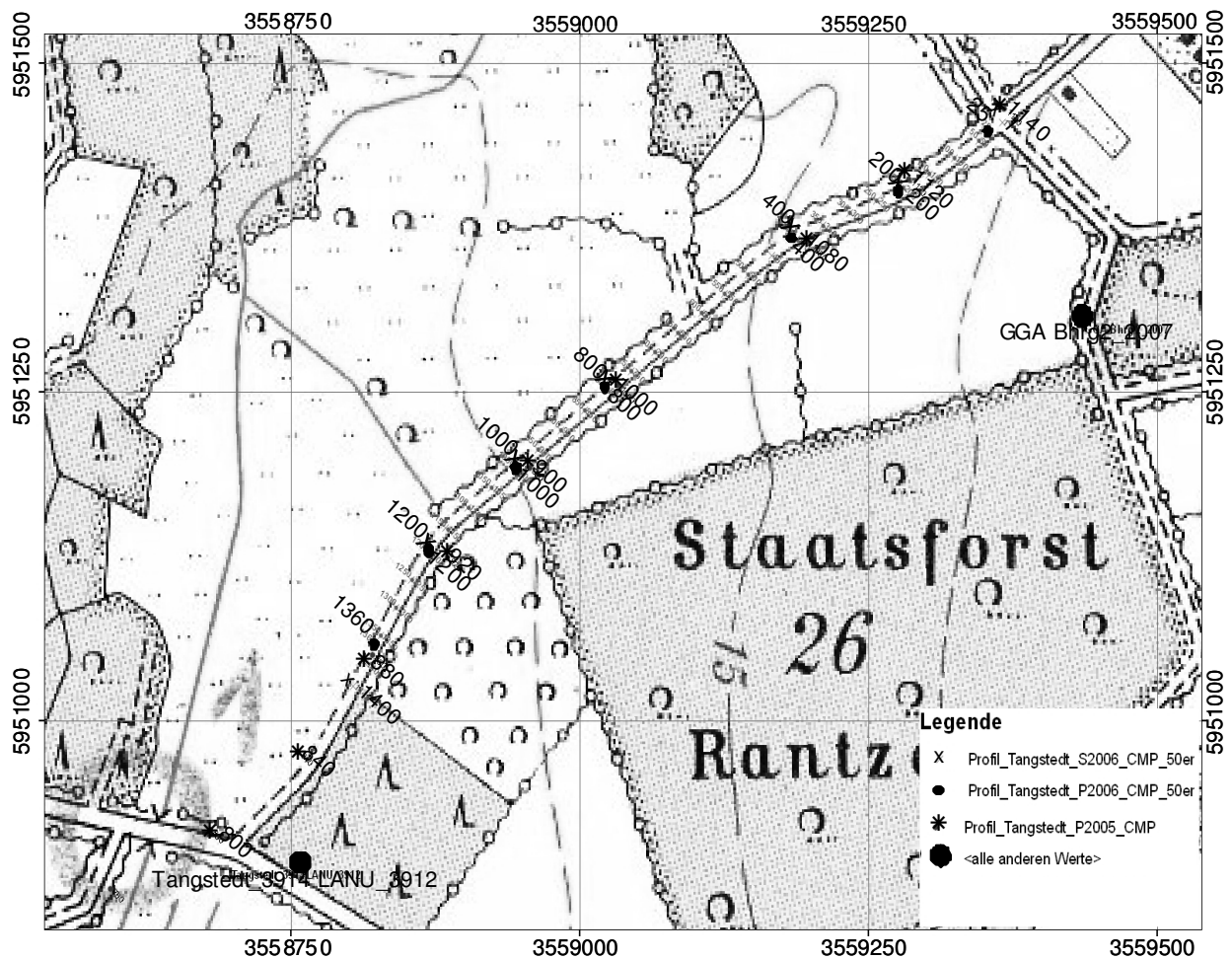


**Figure 5.16:** Profile map and CMP location of the 2006 survey area (profile 2) and the corresponding CMP from profile 1 (profile Tangstedt 2005).

Both P- and S-wave data were acquired using a 72 m length landstreamer. Vibrator sources were used in both cases (P- and S-wave vibrator). All data were processed in CMP technique on a workstation with Landmark's ProMAX seismic processing package (Landmark Corp., Version 2003.12.1).

## 5.2.1 P-wave Seismic Reflection Data of 2006

The survey was conducted along the eastern part of the 2005 Tangstedt line (Figure 5.1 & 5.16), in Ellerbeker Rinne. The survey started at the eastern end of the line. A streamer (Figure 4.8) was used for recording the signal with 72, 14 Hz Geophones for every shot, with a geophone spacing of 1 m. For the seismic source a vibrator (Figure 4.13) was used with a sweep frequency of 40-440 Hz and a total recording length of 13 s and sampling interval of 0.5 ms. There were 353 shots of shot point spacing 2 m and total profile length of 720 m.

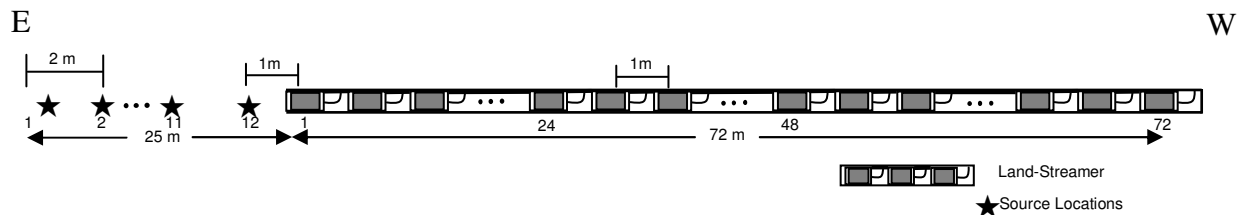


**Figure 5.17:** Field survey layouts for the acquisition of the data. A land streamer consisting of 72 geophones with 1 m separation was used for recording the data with offset-shots.

The survey was set up with offset-shots (Figure 5.17). The design of the acquisition used is: the receiver line is not moved all at once as the source location moves (from E to W) along the profile, but rather the streamer is pulled 24 m after the twelfth movement of the source. The closest geophone to the source is always at 25 m at the beginning of the shot for each session while the source moves towards the geophone. Uncorrelated vibroseis P-wave data was recorded with Geometrics Geoden. Data quality is typically good in the upper 700 ms and decreases significantly beyond this time. Table 5.4 summarizes the basic acquisition parameters.

The P-wave data processing procedure intends to derive a detailed velocity-depth model for the shallow subsurface (~50 m). The first 700 ms two way travel time data was processed. The processing routine (Table 5.5) consisted of: killing dead/noisy traces; automatic gain control (AGC); prestack band pass filtering; muting ground roll, air wave and refracted wave; CMP sorting; velocity analyses; normal move-out corrections, static corrections; CMP stacking; migration and depth conversion.



Seismic source	Vibrator (MHV 2.7 P-wave vibrator)
Recording instrument	Geometrics Geode (Geometrics Inc., Tulsa OK, USA), 24-channel each
Receiver	Land streamer (SM4 14 Hz geophone) orientation vertical (Z-component)
Number of geophones	72
Geophone spacing	1 m
Shot spacing	2 m
CMP spacing	0.5 m
Minimum offset	1 m
Maximum offset	97 m
Maximum fold	25
Sweep frequency	40-440 Hz, 10 s length
Recording length	13 s
Sample interval	0.5 ms
Polarisation	SEG standard
Data format	SEG-2

**Table 5.4:** Shallow P-wave acquisition parameter, profile Tangstedt 2006.

	Processing Steps
Raw data preparation	Assignment of field geometry
	Trace editing
	First break picking
Signal-to-noise enhancement	AGC scaling (100 ms)
	True amplitude recovery (Power raised function)
	Spiking predictive deconvolution (50 ms length)
	Bandpass filter (40-60-400-440) Hz
	Static correction (refraction static), 20 m NN
	Bottom mute (15 ms taper)
Velocity Analysis	Sorting to CMP gather
	Interactive velocity analysis
	NMO correction
	Stretch mute (15%)
Stacking	Stack
	F-X deconvolution
	AGC scaling (150 ms)
	Migration
	Depth conversion

**Table 5.5:** Data processing sequences, profile Tangstedt 2006.

The data were scaled using an automatic gain control (AGC) function before and after prestack processing with 100 ms and 150 ms window length, respectively. The decay of amplitudes with distance is compensated with time-raised power correction function of power constant 1.5 using true amplitude recovery tools. Deconvolution was performed to improve the resolution by suppressing multiples and collapsing the effective wavelet. In this processing, a zero phase spiking predictive deconvolution with a 50 ms operator length was applied to the data followed by a bandpass frequency filter.

The field data was spectrum analysed to determine the dominant frequency band. The frequency spectra (Figure 5.18) shows that the shot gather reflects the frequency spectrum of the sweep, but the low frequencies (50-100 Hz) dominate and the spectral power decreases with increasing frequency. Frequency spectra of different portions of the shot gathers were also inspected (Figure 5.19). Besides, a number of band pass filter tests was applied. This is usually done by trying several bandpasses and picking the best one. 40-60-400-440 Hz was chosen to attenuate noise outside the sweep frequencies.

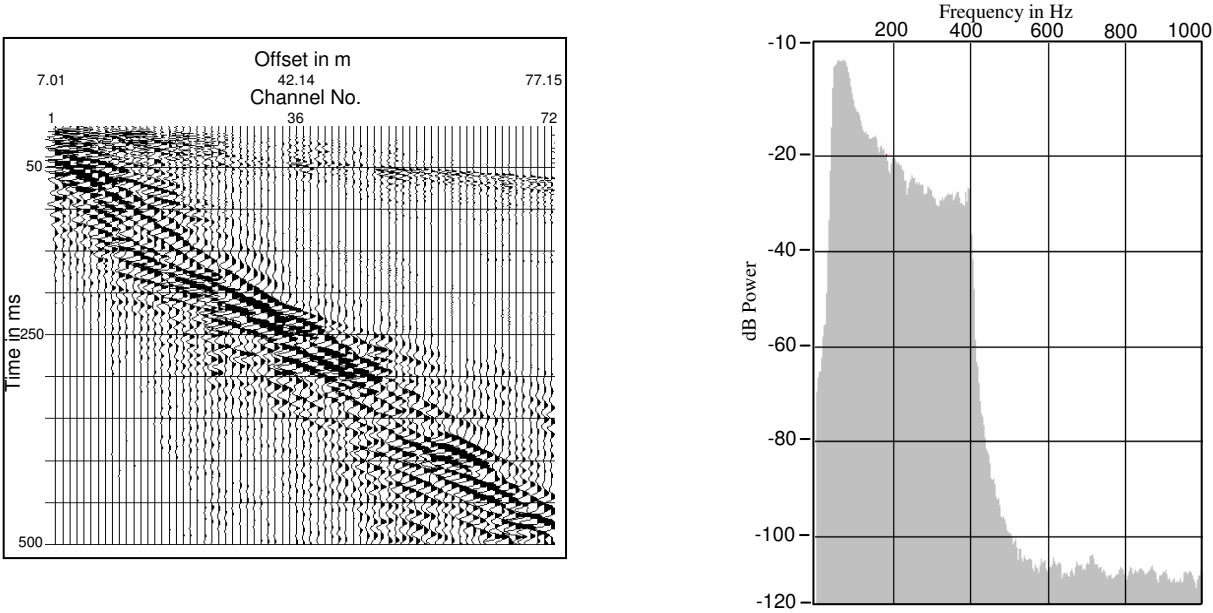


**Figure 5.18:** Frequency content of a reflection shot gather.

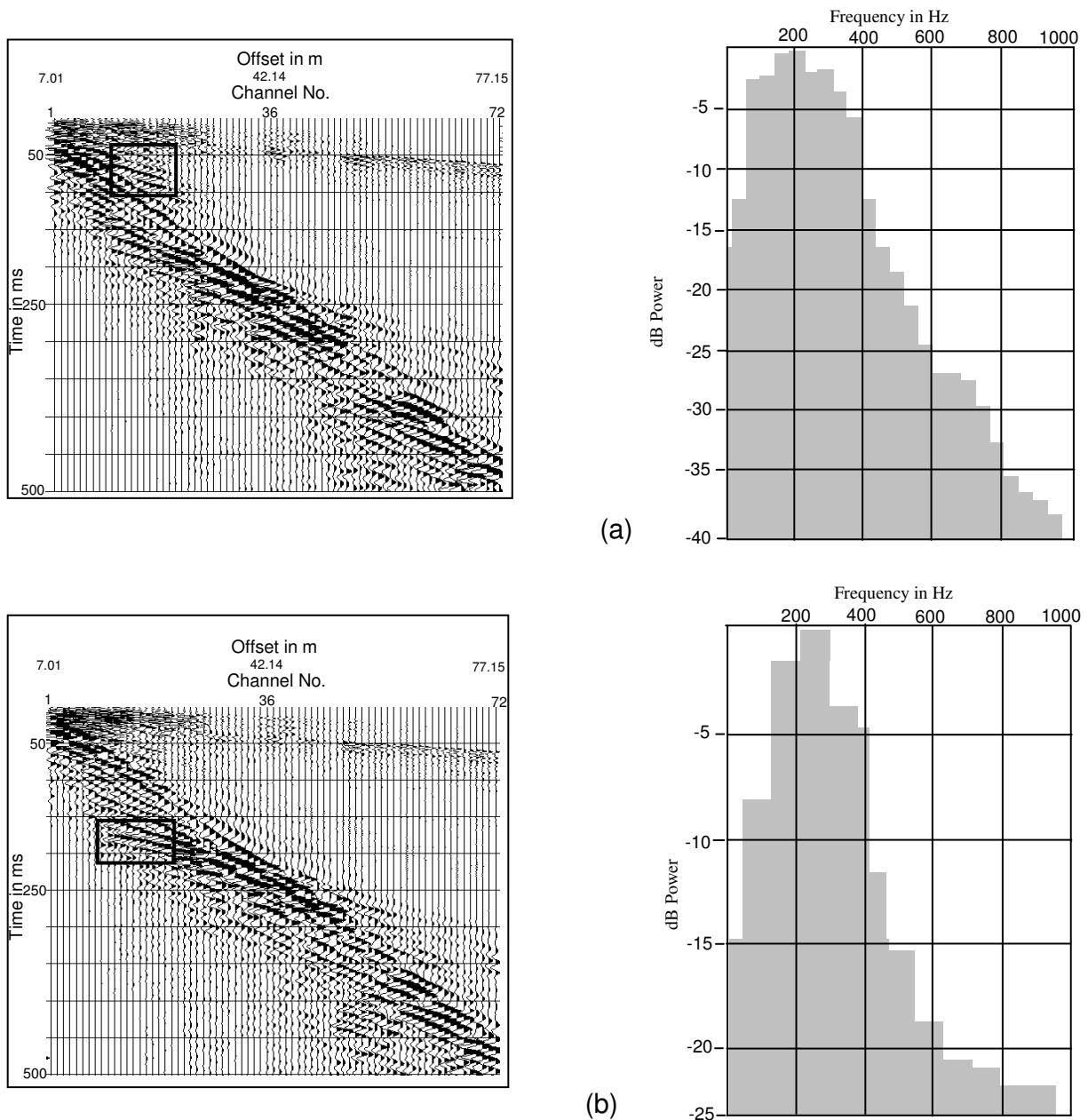


**Figure 5.19:** Raw shot gathers and amplitude spectra for the marked region. (a) Reflection between 50 and 100 ms, the dominant frequency is 50 to 300 Hz. (b) Reflection between 150 and 200 ms, the dominant frequency is 80 to 300 Hz.

Static corrections are made to move the apparent position of the sources and receivers to the high datum. Source and receiver static shifts are calculated from time picks of the first arriving refractions. A replacement velocity of 1800 m/s and a datum of 20 m NN was used for the refraction statics calculations which locate the datum at the top of the highest location in the profiles (Figure 5.20b) in order to image the shallowest reflections on the eastern margin where the elevation rose to this height. Bottom mute with 15 ms taper have been used to remove source-generated noises (air, guided and surface waves) from the shot gather (Figure 5.20d).

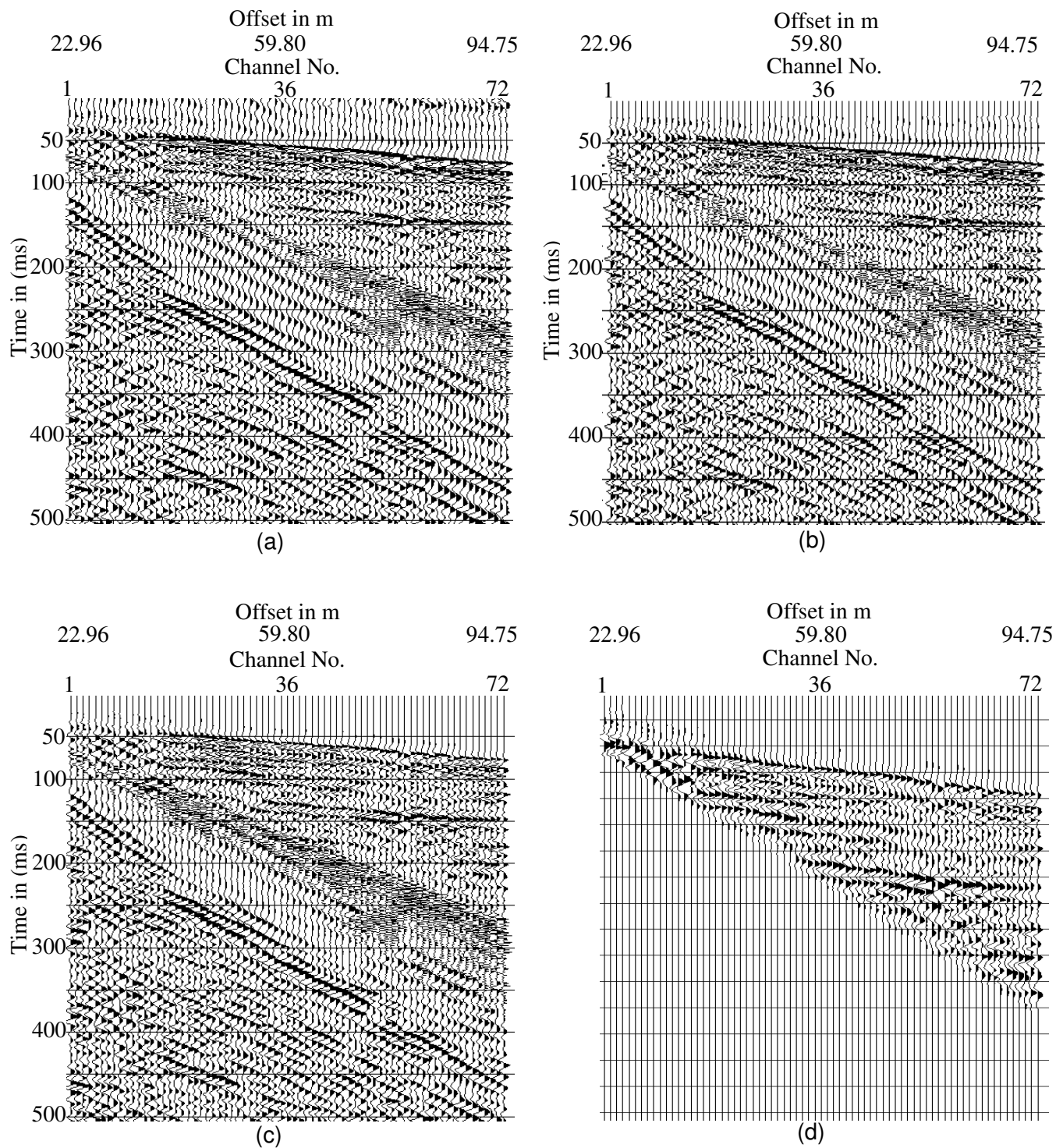


**Figure 5.20:** A single shot gather offset from 22.96 to 94.75 m, (a) scaled (AGC, 100ms), (b) after static correction, (c) after deconvolution and application of a band pass filter, (d) after mute applied (depth scale changed).

The prestack processing steps suppressed successfully most of the noises and other low-frequency events, revealing some clearly distinguishable reflection events in the shot gathers (Figure 5.20d).

Detailed velocity analysis proved to be the most important and time-consuming step in the processing flow. For the calculation of the velocity function for performing NMO correction the traces are sorted to form a CMP gather. The velocity analysis is performed on these selected CMP gathers. The rms velocity function was developed through detailed analysis of semblance plots (Figure 5.21), constant velocity stacks and NMO corrected gathers. These velocity functions then are spatially interpolated between the analysis points across the entire profile. The velocity scanning was performed on each CMP gather during a velocity panel analysis that ranged from 1000 to 2500 m/s. Subsequently a range of stretch-mutes were tested. A maximum 15% stretch mute is applied to remove the effect of NMO stretching. A velocity of ~1800 m/s at ~20 ms, ~1865 m/s at 80 ms, ~1915 m/s at 120 ms and ~2075 m/s provided the best alignment of normal move out (NMO) corrected seismic signals for the example given in Figure 4.13 (corresponding to the left analysis in Figure 5.21).

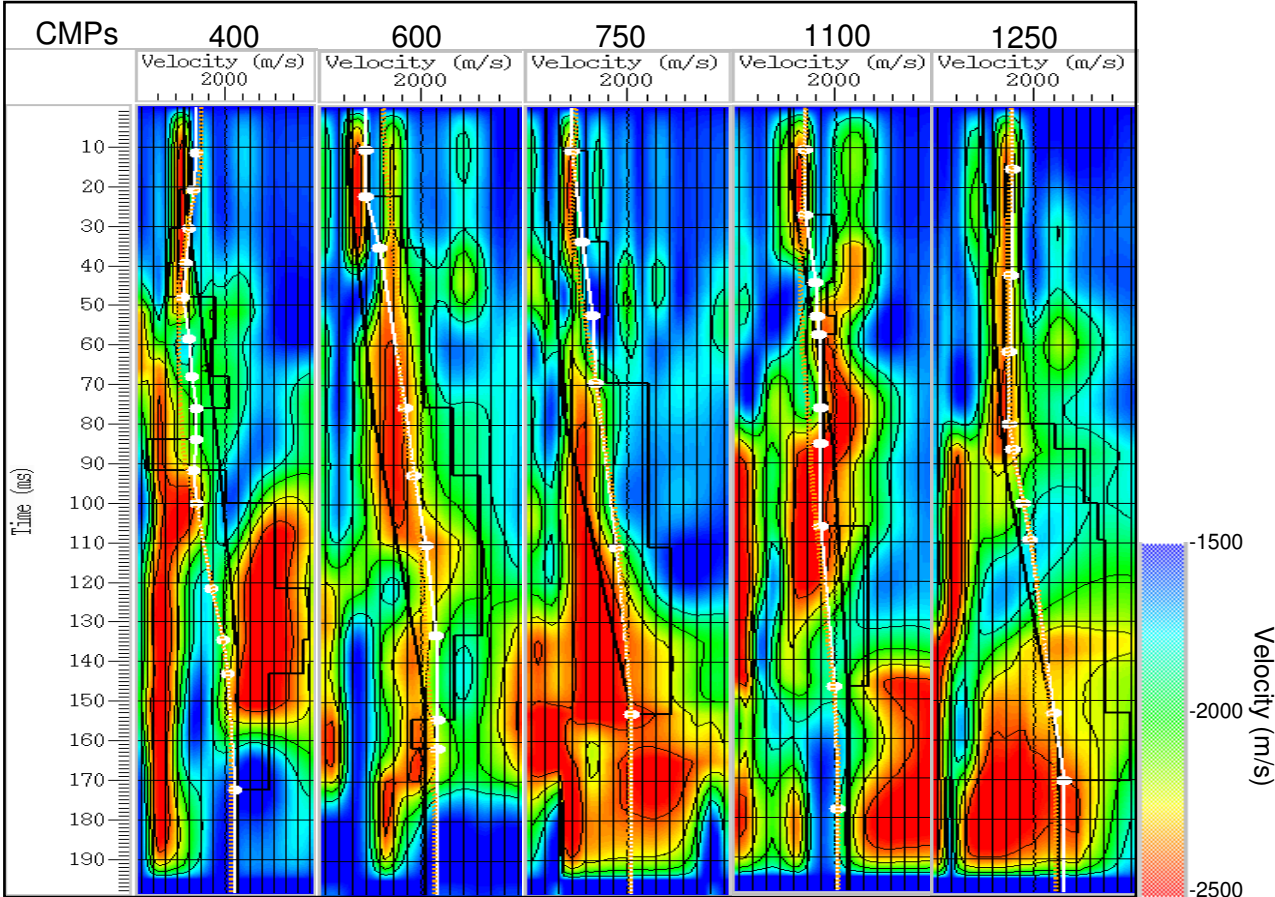


**Figure 5.21:** Velocity spectrum with the picked velocities at different CMP points.

Subsequently the stacking velocities are determined for selected CMP gathers. In the mean there was a velocity analysis every 100 CMP. The stacking velocities ranged from about 1500 m/s at 20 ms to about 2500 m/s at 200 ms. Figure 5.22 shows the lateral variations of stacking

velocities along the profile. The velocity field shows lower velocities in the east and an increase of velocities to the west down to 80 ms, and a higher velocity in between 80 to 200 ms in the east.

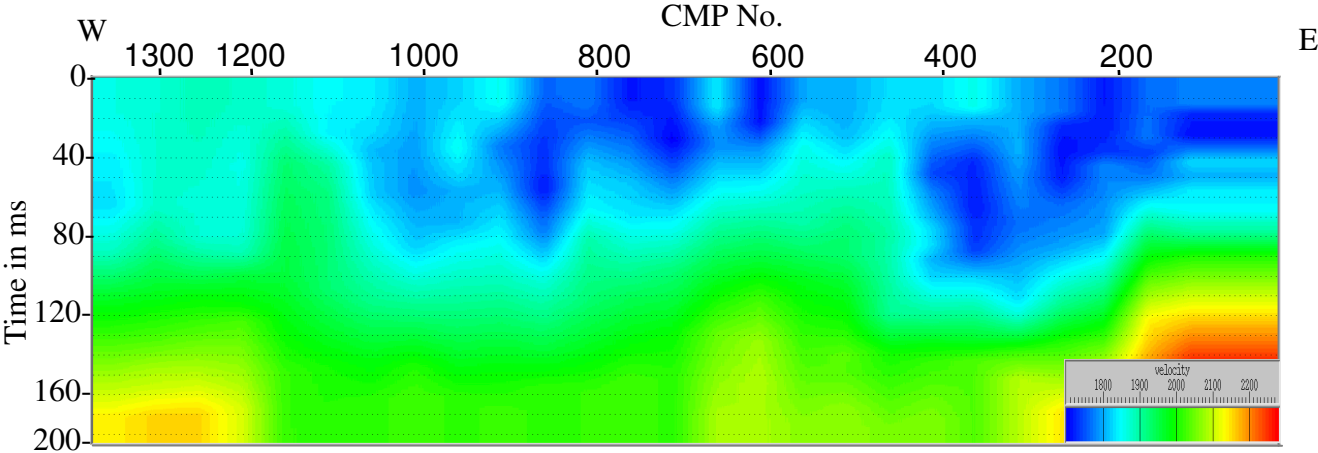


**Figure 5.22:** Stacking velocity field from the velocity analysis of CMP gather.

The stacked section of the profile shows a sequence of reflected events. These reflected events seem to be uninterrupted and dip to the west (Figure 5.23) and consist of five major reflection boundaries. The shallowest dipping reflection at ~25 ms, the second reflection ~50 ms, the third reflection ~70 ms, the fourth set of reflections from ~80 ms to ~140 ms and the fifth set of reflection starting at ~160 ms two-way travel time. The stacked seismic section also clearly shows depression like structure between CMP 60 and 400 (30 to 200 m).

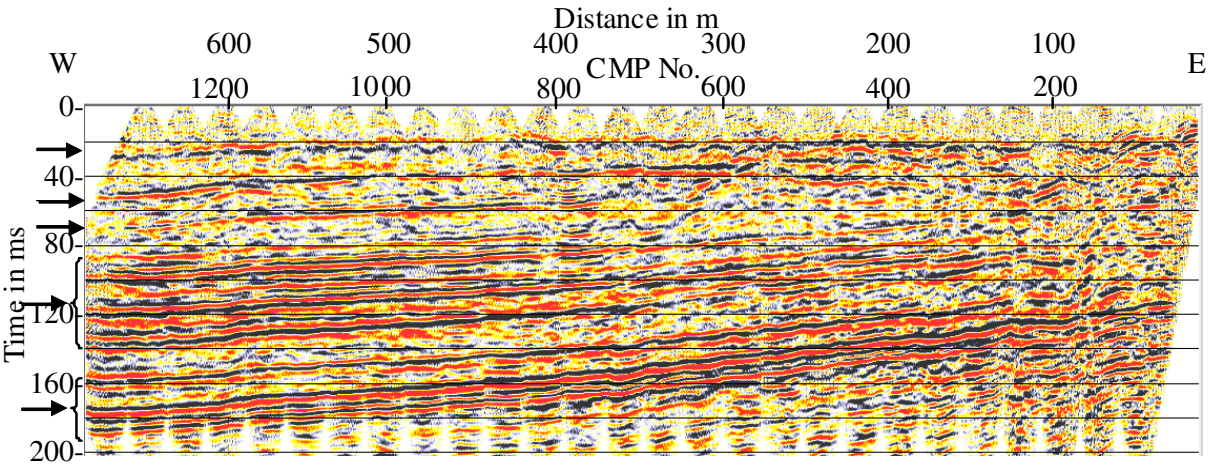


**Figure 5.23:** CMP time stacked section to reference elevation (20 m NN). The arrows point to major reflectors.

The stacking velocities (Figure 5.22) are used as input to generate the interval velocities. The Velocity Field Manipulation was employed to analyze the stacking velocities and convert them to an appropriate set of interval velocity functions. Applying a 100 CMP horizontal smoother and converting the stacking velocity model via a smoothed gradient function (i.e.

interval velocity functions having a smooth variation in slope) a single interval velocity function is estimated for migration. The interval velocity ranges from ~1800 to ~2340 m/s for the first 200 ms two-way travel time. Once the interval velocity is computed, a poststack Implicit FD time migration is carried out to produce the migrated section (Figure 5.24a). All the migration process was performed on the final datum (20 m NN). The migration procedure produces only minor changes for the reflectors.

For the time-to-depth conversion, the single interval velocity function in time was converted to depth interval velocities. Besides, the resulting interval velocity (~1800 m/s) from the surface to 5 m depth is replaced by the weathering layer velocity (~540 m/s). Finally the interval velocity field ranged from about 540 m/s at the surface to 2340 m/s at 200 m depth. Figure 5.24b displays the depth section. In this depth section we find the five above defined reflectors at ~25 m depth, ~50 m depth, ~70 m depth, ~ 100 m to ~145 m depth and ~165 m to ~200 m depth.

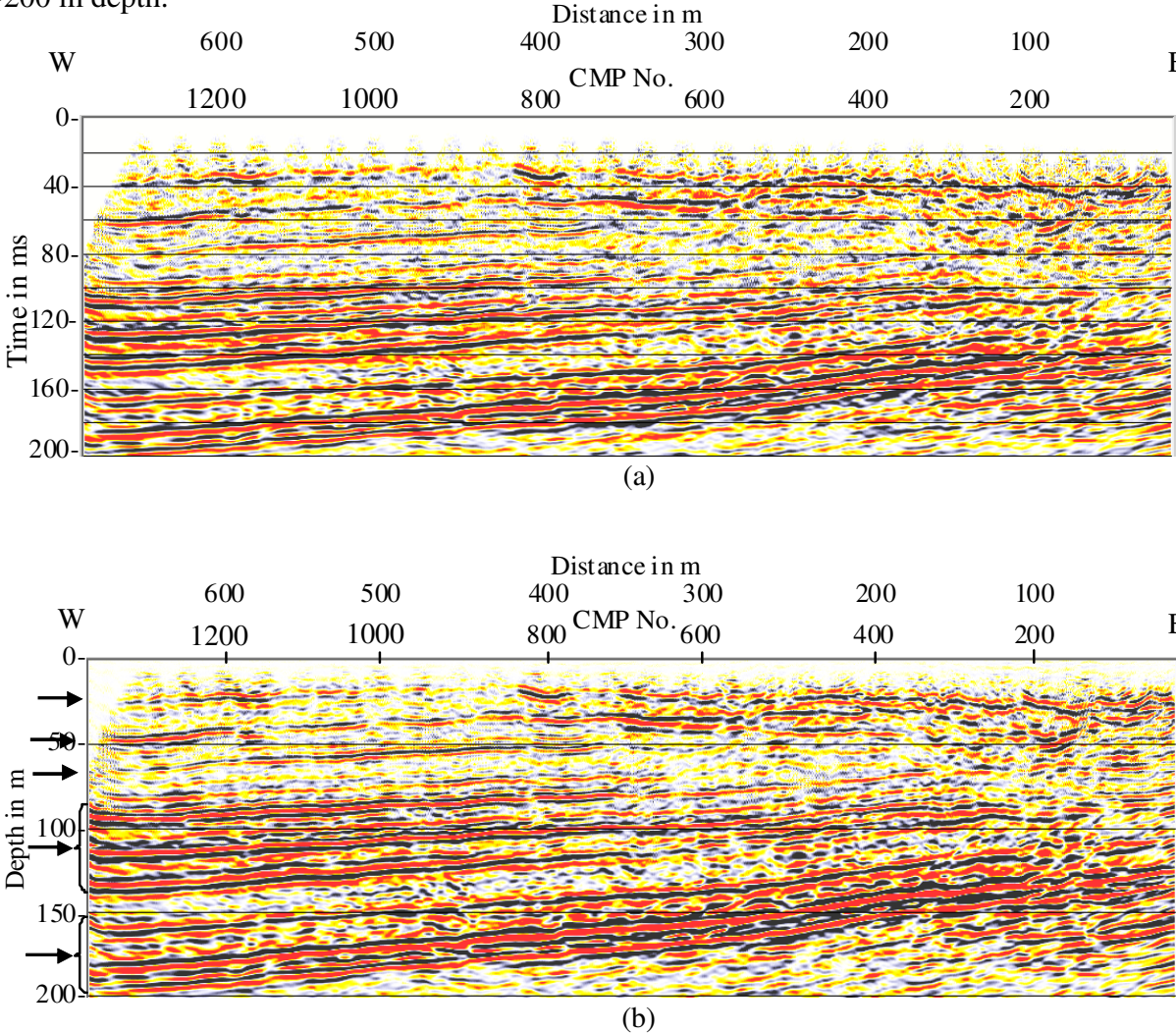


**Figure 5.24:** Stacked (a) migrated time section, (b) depth section (reference elevation (20m NN)). The arrows point to major reflectors.

## 5.2.2 S-wave Seismic Reflection Data of 2006

S-wave reflection data were acquired between June 26 and 28, 2006 along the same profile and overlapping the P-wave profile (Figure 5.16). A combination of end-on and split-spread geometry with 2 m shotpoint spacing and 1 m source offset was used (Figure 5.25).

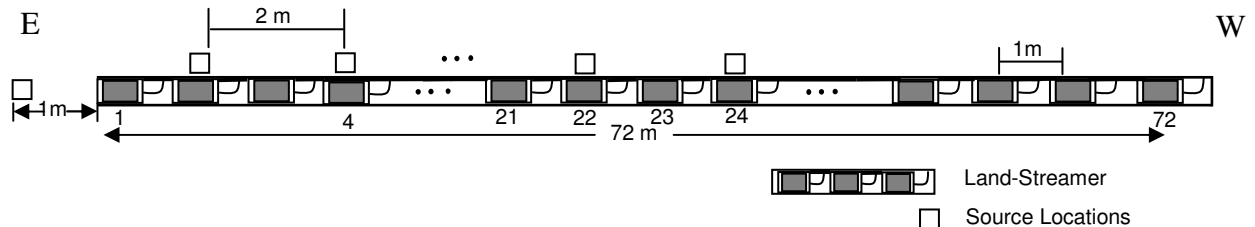


**Figure 5.25:** Field survey layouts for the acquisition of the data. A land streamer consisting of 72 geophones with 1 m separation used for recording the data with a combination of end-on and split-spread shot.

The active spread consisted of a land-streamer containing 72 SM6-H 10 Hz horizontal geophones. Seismic energy was generated by an S-wave vibrator (EIVis-4) and a sweep frequency of 20–200 Hz. In each case two shots are recorded at the same location with the source motion direction of the two records 180° apart. The reflection data were collected in SH mode (sensitive to horizontally polarized shear waves) on Geometrics Geoden with a 12 s record length, and a one-millisecond sampling interval. Table 5.5 summarizes the basic acquisition parameters.

After the data is stored in ProMAX format in the ProMAX system (Landmark Corp., Version 2003.12.1) it is correlated with an external sweep. The correlated data from a given shot point is summed together in order to enhance the S-wave signal and to reduce the coherent P-waves. The summing improves the quality of the data. Figure 5.26 shows correlated and summed data for a single shot point in the middle of the profile with AGC applied (with 300 ms window length). The data has a good quality for the upper 500 ms, but decreases significantly beyond this time.



Seismic source	SH-Vibrator(ElVis-4), Electrodynamic vibrator system
Recording instrument	Geometrics Geode (Geometrics Inc., Tulsa OK, USA), 24-channel each
Receiver	Land streamer (SM6-H 10 Hz geophone) orientation horizontal and perpendicular to streamer (SH-component)
Number of geophones	72
Geophone spacing	1 m
Shot spacing	2 m
CMP spacing	1.5 m
Maximum fold	36
Sweep frequency	20-200 Hz, 10 s length
Recording length	12 s
Sample interval	1 ms
Polarisation	SEG standard
Data format	SEG-2

**Table 5.6:** Shallow S-wave acquisition parameters, profile Tangstedt 2006.

The data processing of the S-wave survey was conducted using a sequence of steps listed in Table 5.7. After trace editing a trace-to-trace amplitude-balancing function (trace equalization) was applied. This function minimizes differences in sample amplitudes resulting from differences in acquisition equipment performance or source and receiver coupling with location. This has been done using a single time window gate for each trace. In order to suppress as much noise as possible without degrading the reflection signal quality, a zero-phase Ormsby band-pass filter in the frequency domain was applied to the shot gathers. A number of band pass filter tests (Figure 5.27) was made for specifying the four corners of the frequency band pass; 40-50-180-195 Hz has given the best result (Figure 5.27c).

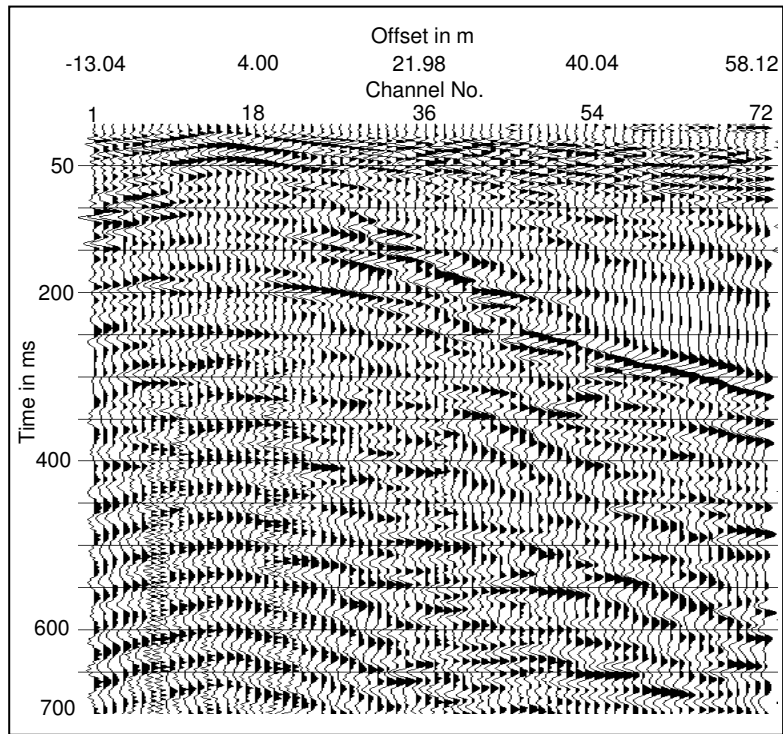


**Figure 5.26:** One sample shot gather, summed and correlated data with AGC (300 ms).

	Processing Steps
Raw data preparation	Correlation and Summing of traces
	Assignment of field geometry
	Trace editing
Signal-to-noise enhancement	AGC scaling (300 ms)
	Bandpass filter (40-50-180-195)
	AGC scaling (120 ms)
	Trace equalization
Velocity Analysis	Sorting to CMP gather
	Interactive velocity analysis
	NMO correction
	Stretch mute (500%)
	Bandpass filter (30-40-180-195)
Stacking	Stack
	Bandpass filter (20-30-180-195)
	F-X deconvolution
	AGC scaling (150 ms)
	Migration
	Depth conversion

**Table 5.7:** S-wave data processing sequences, profile Tangstedt 2006.

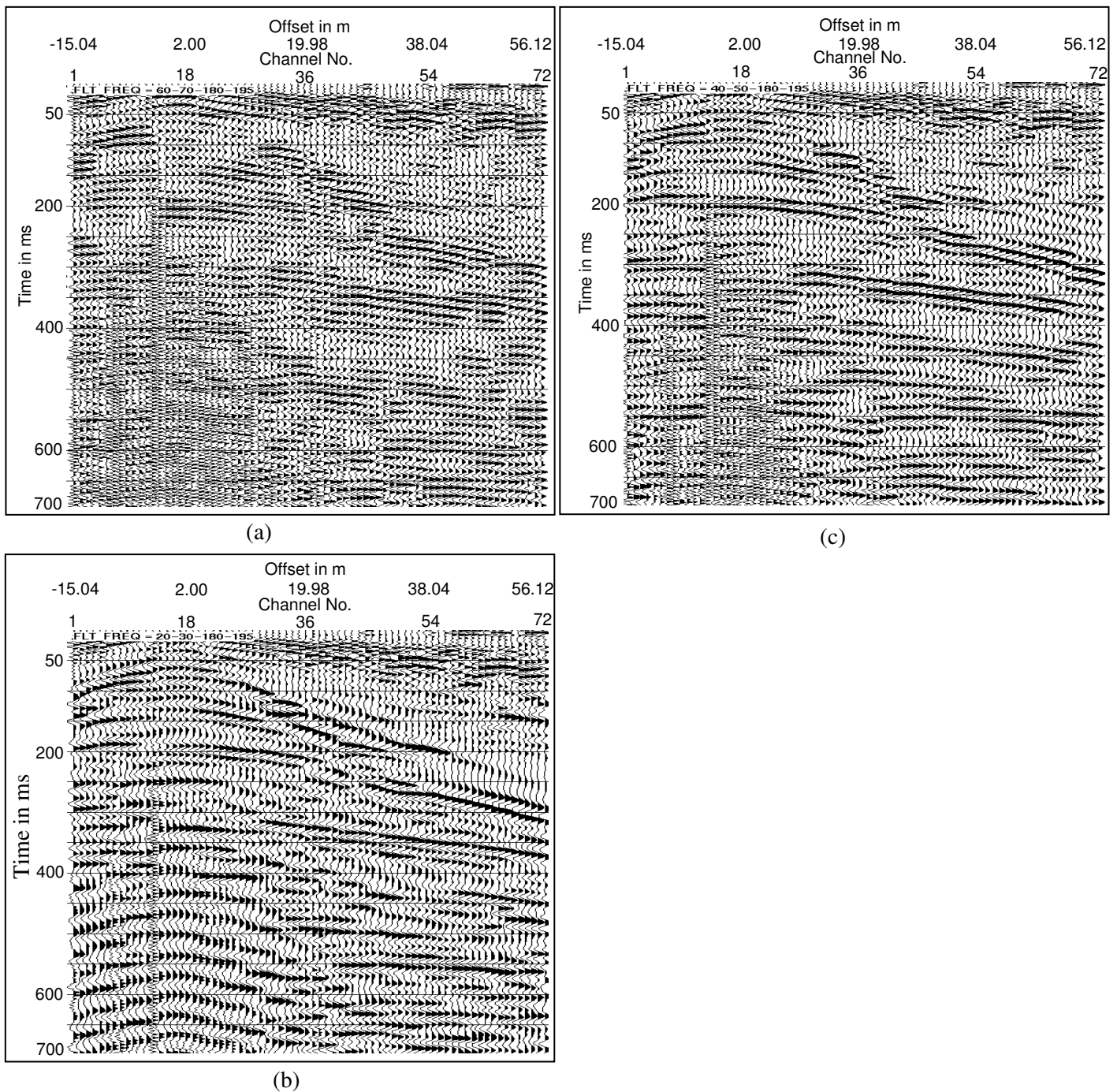


**Figure 5.27:** Shot gather with zero-phase Ormsby band-pass filter, trace equalization (50 ms time gate) and AGC (300 ms) applied. (a) 60-70-180-195 bandpass, (b) 20-30-180-195 bandpass and (c) 40-50-180-195 bandpass.

Estimates of velocity and velocity variations obtained from shot gather and constant velocity stack analysis are used to define optimal input parameters for semblance analysis. Figure 5.28 shows velocity spectra and picks for a CMP gather (left) at CMP 1225 and the same CMP gather after applying NMO correction and 500% stretch mute (right). The velocity scanning was performed on each CMP gather during velocity panel analysis that ranged from 100 to 800 m/s. A velocity of ~420 m/s at ~10 ms, ~310 m/s at ~50 ms, ~230 m/s at ~100 ms and

~200 ms, ~340 m/s at ~300 ms and ~500 ms provided the best alignment of normal move out (NMO) corrected seismic signals for the example in Figure 5.28.

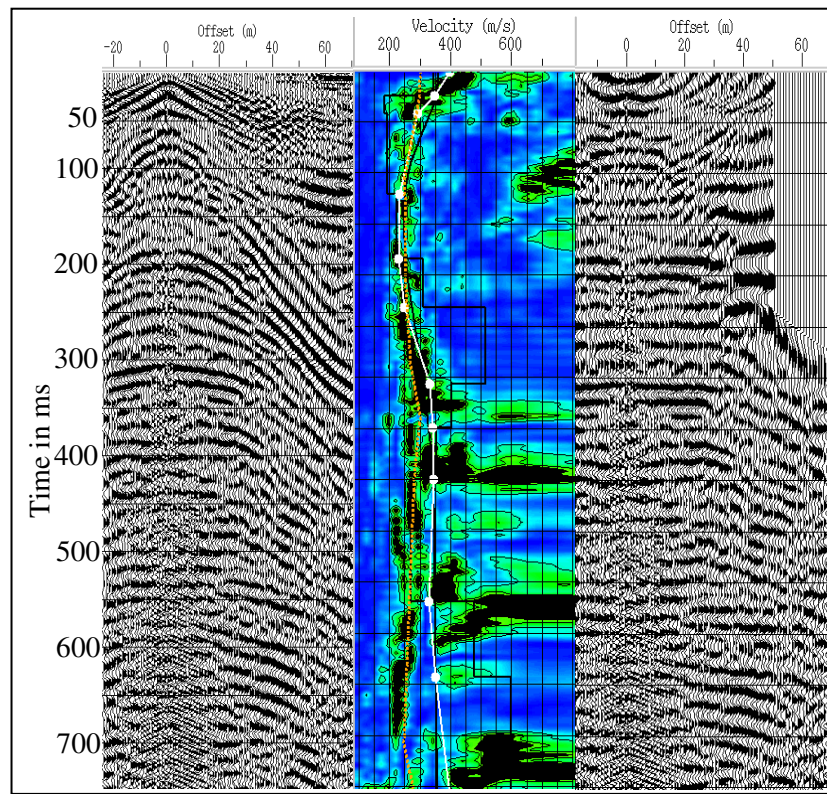


**Figure 5.28:** Velocity spectra, velocity picks and CMP gather before (left) and after (right) NMO correction.

The stacking velocity field (Figure 5.29) indicates that the optimum stacking velocity mostly ranges from about 240 to 400 m/s. And it comprises relatively higher velocities for the first ~50 ms, low velocities for the next 400 ms (~50 - ~450 ms) and a slight increase of velocities to the bottom part of the field. The lateral velocity variation is minor except for the part of the seismic line between ~400 ms to ~600 ms.

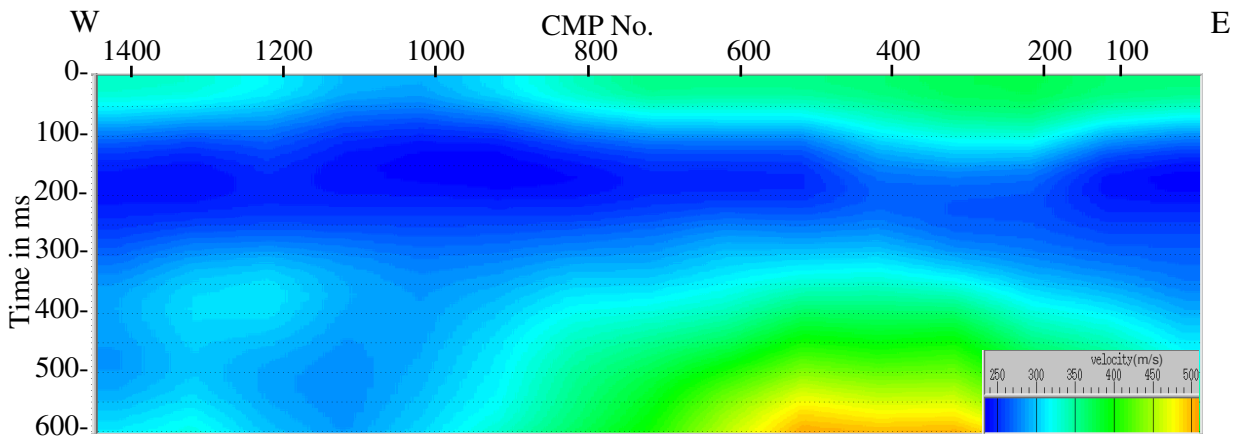


**Figure 5.29:** Stacking velocity field from the velocity analysis of several CMP gathers.

Stacking of the CMP-sorted data followed by bandpass filtering (30–40-180-195 Hz) and F-X deconvolution (20-200 Hz) results in the section displayed in Figure 5.30. The shallowest reflection appears at ~25 ms, this reflection can also be observed as distinct hyperbolic-shaped event in the raw and prestack processed data (Figure 5.26 & 5.27c) and could be confidently recognized as true reflection. The most prominent reflectors of the S-wave section are observed at approximately 200 ms and 350 ms. For longer times it is hard to see any coherent features (reflections).

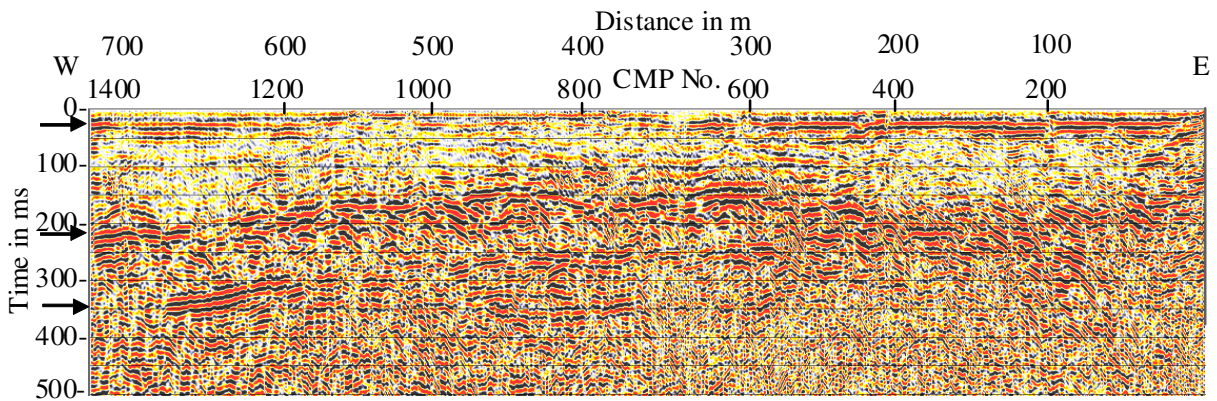


**Figure 5.30:** Stacked time section, the arrows point to major reflectors.

The single function interval velocity is generated from the stacking velocities through smooth gradient conversion. The interval velocities range from ~190 to ~530 m/s for the first 500 ms two-way travel time. These interval velocities were used to perform migration and time-to-depth conversion. A poststack implicit FD time migration is performed to produce the final migrated image. Since the interval velocity over-migrated the data and introduced some distortion the interval velocity was reduced to 80%. Figure 5.31a shows the fully migrated image of this line. In general, the migration improves the stacked section, scattering is reduced, and dipping reflectors are positioned better. The depth converted section is shown in

Figure 5.31b. The rough estimates of the depth range of the reflected events appearing on the sections were made on the basis of the interval velocities derived from the rms velocities of the seismic data. According to this depth section the shallowest S-wave reflection appearing at a time of about 25 ms is about 4 m deep, whereas the other reflectors that appear at a time of about 200 ms and 350 ms is about 25 m and 50 m deep respectively. As there were no static correction applied to the data the zero time or depth line refers to the surface and not to a certain reference datum.

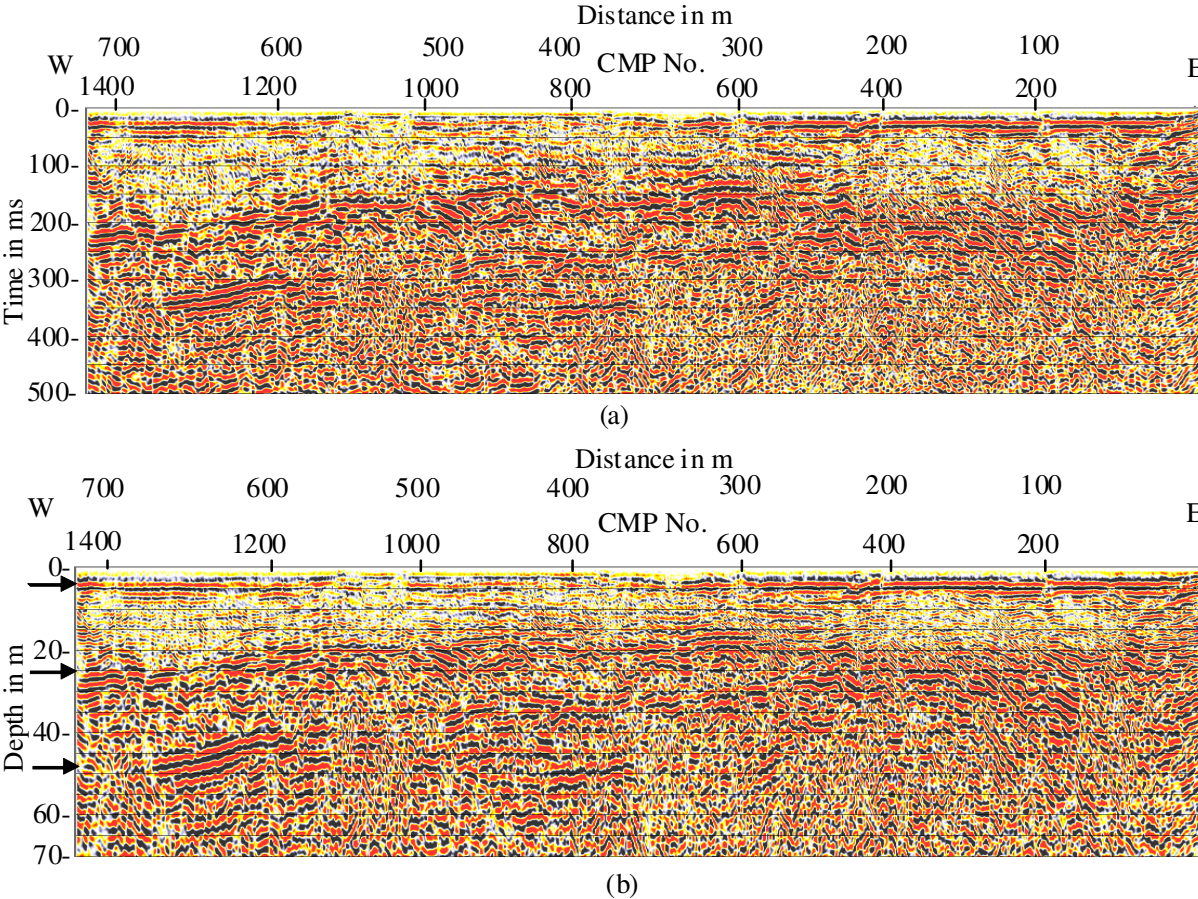


**Figure 5.31:** Stacked (a) migrated time section, (b) depth section (the arrows point to depth of the reflectors as discussed in the text).

### 5.3 Shallow P- and S-wave Seismic Section Correlation

Combining P- and S-wave wavefields provide independent measurements of rock and fluid properties. To identify those properties a comparison of P- and S-wave reflection at the same depth level is crucial. Miscorrelation of key strata surfaces will lead to mistaken seismic-based attributes ( $V_p/V_s$  ratio, Poisson's ratio, shear modulus, and bulk modulus) and make accurate interpretation impossible. In this section we look at correlations in shallow P- and S-wave reflection data which was acquired in the same line (section 5.2). The survey utilized higher frequencies (40-400 Hz) for P-wave and lower frequencies (20-220 Hz) for the S-wave. Figure 5.32 presents a typical example of P- and S-wave AGC scaled raw field data records. The acquired reflection data were of good quality; both shot records show recognizable reflections. The coherence of the S-wave data looks better than that of the P-wave data, probably because of lower frequency, less scattering and, last but not least absence of surface waves. The reverse stacking method (summing left and right shot) also removes much noise on the S-wave.

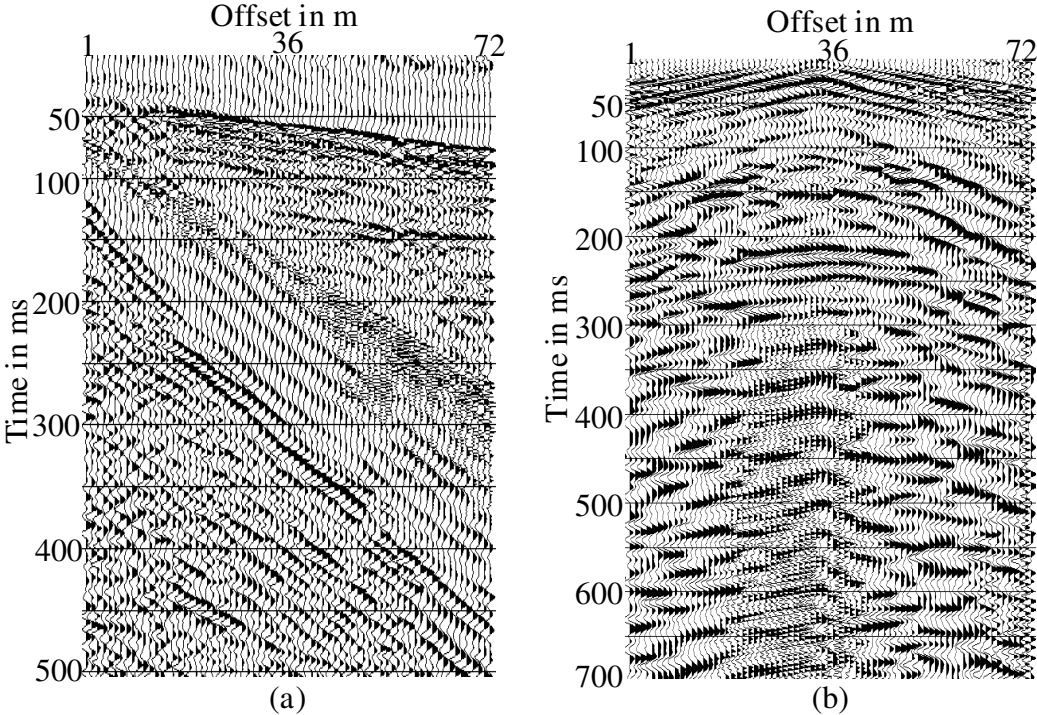


**Figure 5.32:** Raw shot gathers. (a) P-wave with AGC (100 ms), (b) S-wave with AGC (300 ms).

The prestack processed P-wave and S-wave shot records (Figure 5.33) show good quality and fine hyperbolic arrivals representing reflections. The P-wave prestack processed data has observable reflections from about 40 ms to 200 ms. Static correction is performed on this data with a datum of 20 m NN; this may create a shift on the position of the P-wave reflectors. In the case of the S-wave data no static correction is made. On the S-wave prestack processed

data (Figure 5.32b) hyperbolic reflections are observed just below the surface until about 500 ms.

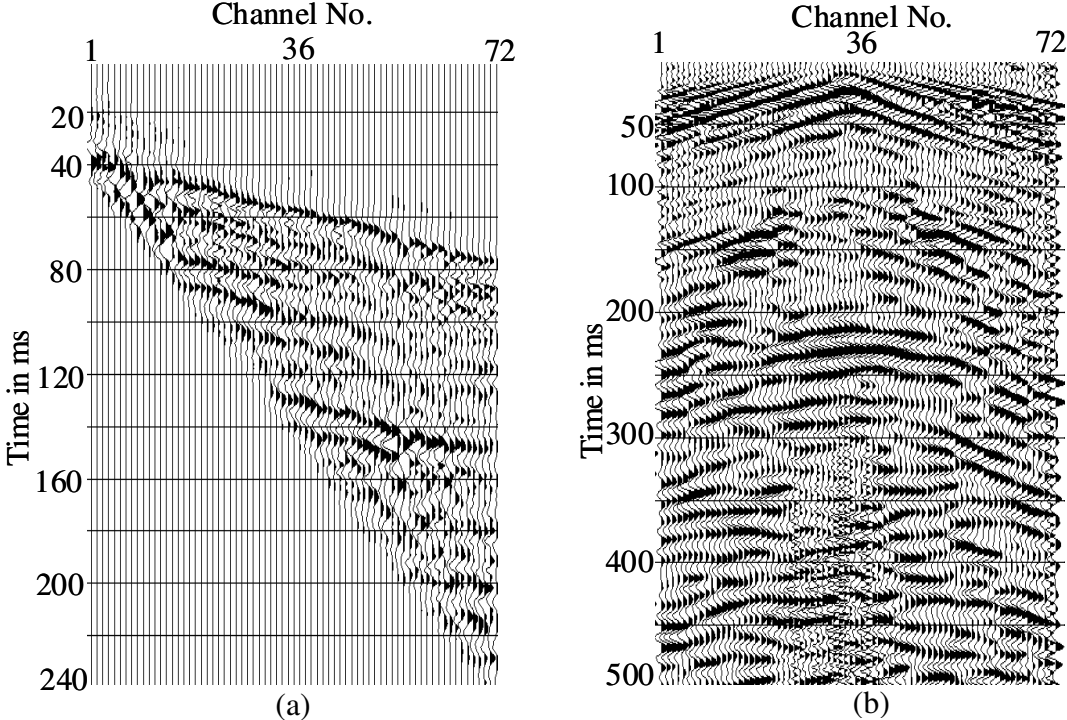


**Figure 5.33:** Example of P-wave (a) and S-wave (b) prestack processed shot gathers. The P-wave records are filtered with a 40-60-400-440 Hz frequency bandpass filter and the S-wave records with a 30-40-180-195 Hz bandpass frequency filter.

For establishing a P-wave to S-wave event correlation a common first intuition is to try to compare events between the two data sets in section view. Figure 5.34 and 5.35 show the P-wave and S-wave depth section (CMP 100 to 1360) and stacked time section (CMP 1200 to 1300) along the profile, respectively. When a visual comparison is made between the two stacked sections the S-wave shows a reverse of polarity; because of this a polarity reversion is made in the S-wave section. The S-wave seismic section along the line shows a sequence of reflected events within the ~25 ms (~4 m) - ~350 ms (~50 m) depth range, while the P-wave section shows clear reflected events from about 25 ms (25 m) to about 180 ms (200 m). In the P-wave profile there is hardly any reflection recognized in the shallowest part of the section (<25 ms or 25 m). On the other hand the deeper reflections from the P-wave section have no corresponding expression in the S-wave section.



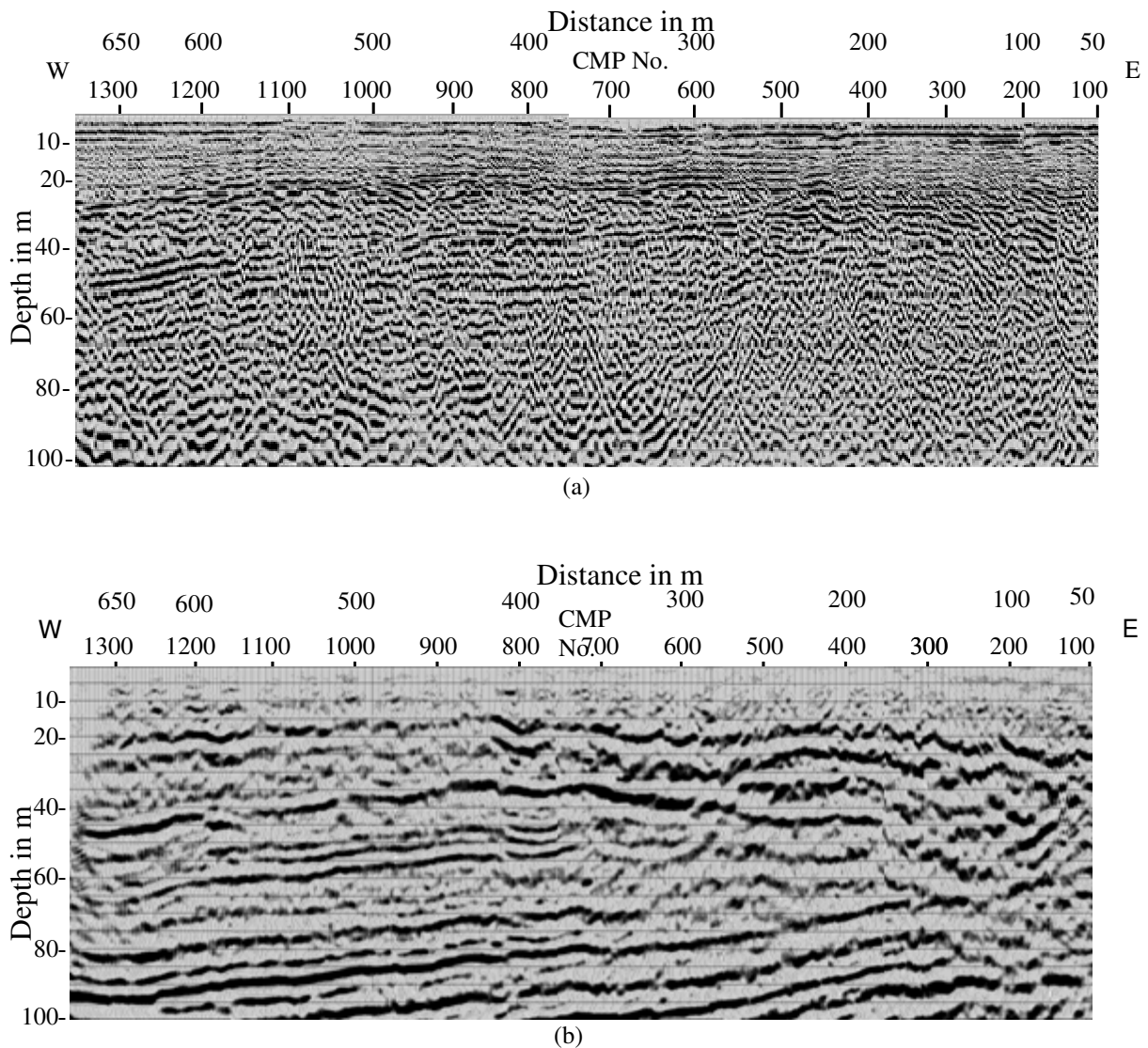


**Figure 5.34:** Depth section for 100 m depth. (a) S-wave section, (b) P-wave section.

In order to make the time correlation first a search of the P- and S-wave depth section was made to locate reflections that should be expected on both data sets and thus provide a correlation basis. Estimates obtained from this initial depth equalization attempt revealed the most definitive correlation on the intermediate section. Two “depth equivalent” horizons were picked on the P- and S-wave depth sections (Figure 5.34). Based on these horizons, Figure 5.35 correlates P-wave time of 25 ms to S-wave time of 200 ms and P-wave time of 50 ms to S-wave time of 350 ms. The ratio of correlated time intervals ( $t_s/t_p$ ) range from 4 to 5 across the analysis window. This time interval ratios have a relationship with  $V_p/V_s$  ratio (for details see section 6.2).

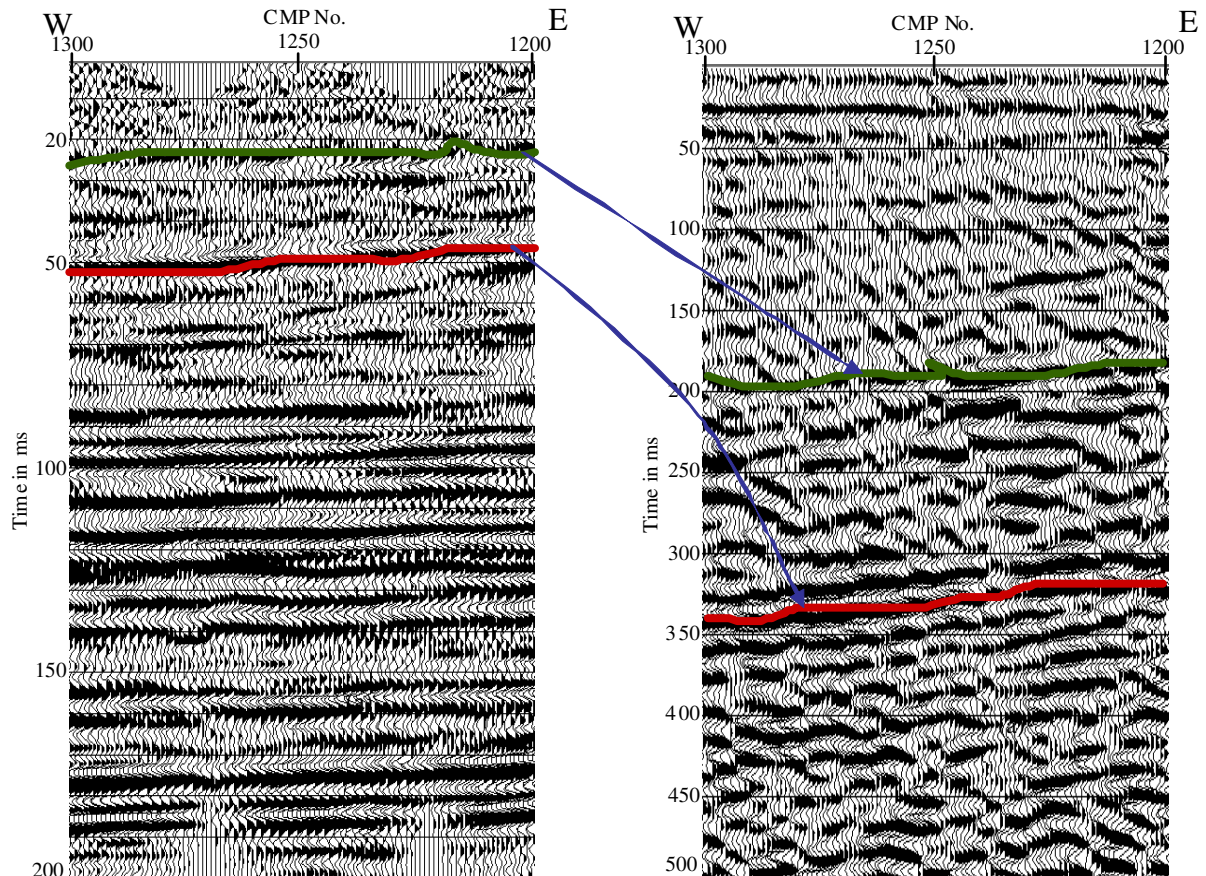


**Figure 5.35:** Part of P-wave (left) and S-wave (right) time section from CMP 1200 to 1300. The coloured lines indicate reflections from the same horizons.

#### 5.4 P-wave Velocity Field: Conventional P-wave Refraction Tomography vs. Shallow P-wave Reflection

The seismic refraction tomography approach in the conventional seismic reflection data was applied in section 5.1.1 to obtain detailed information in the shallow sub-surface ( $\sim <50$  m). The interval velocity field from the tomographic inversion for the whole profile (3415 m) is displayed in Figure 5.6b. Into this section, in order to compare the tomography inversion result, the shallow P-wave reflection data from section 5.2.1 is incorporated. Figure 5.36 is a rescaled version of the tomography velocity field at the same surface location and scale as the shallow reflection image in Figures 5.37.

On the basis of information presented in Figures 5.36 and 5.37 a comparison of the refraction tomography velocity field to boundaries or interval velocities of the shallow seismic reflection was made. There is some correspondence between the reflection image and the velocity interface on the tomographic model (Figure 5:38). As mentioned in section 5.1.1 it is difficult to get a sharp boundary in the refraction tomography field. By taking approximately the high

contrast velocity junction as boundaries for the tomographic velocity field the comparison can be done. The velocity boundary at ~10 m depth does not match in the shallow reflection section since it is hard to see a reflector within this depth range. The reflector at ~25 m depth can be approximated to the velocity boundary at ~30 m depth of the tomographic velocity field, and the reflector at ~50 m can be approximated to the velocity boundary at ~50m of the tomographic velocity field. Below ~50 m the refraction tomography velocity field is not reliable.

On the other hand the interval velocities have also some correspondence. For example the interval velocity ranges from about 540 m/s to 1900 m/s in the case of the shallow reflection section from the surface to a depth of 50 m; for the same depth the velocity varies from about 519 m/s to 2300 m/s for the tomography field. But for the high velocity gradient (anomalies) between 225 m and 350m for the tomography field along the profile there is no expression in the shallow reflection section. In Figure 5.36 and 5.37 the zero depth refers for both lines to 20 m NN.

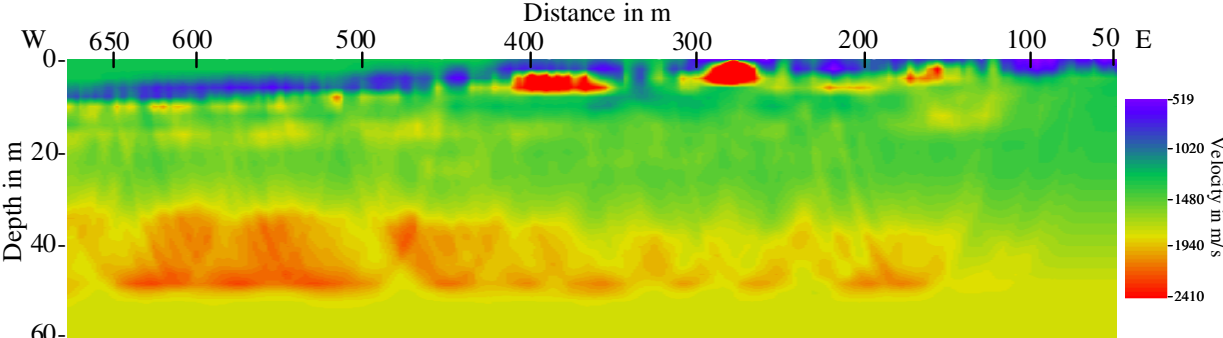


**Figure 5.36:** P-wave refraction tomographic velocity field rescaled for the same surface locations as the shallow P-wave reflection depth section in Figure 5.37.

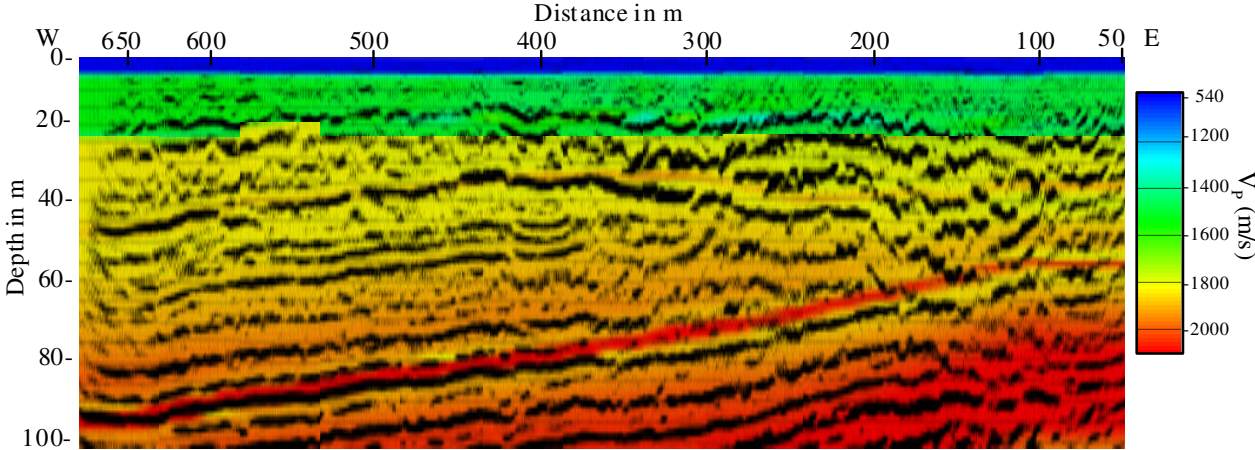


**Figure 5.37:** Shallow P-wave depth section with the interval velocity field.

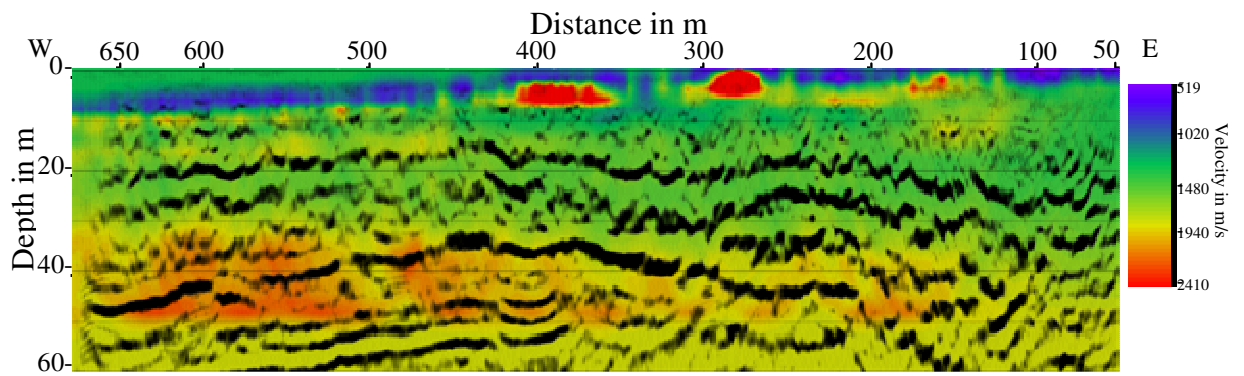


**Figure 5.38:** Shallow P-wave depth section with the refraction tomography velocity field.

# 6. Interpretation, Combination and Integration

In this section, the geological interpretation of the seismic velocity models, i.e. P-wave refraction tomography, and the shallow P- and S-wave reflection are presented. This interpretation involves the incorporation of borehole data as well as some well-known geologic and geophysical characteristics of the area from previous studies. The three nearby boreholes: Tangstedt 3914, Borehole B1 and B2 (see section 2.2) are used for the interpretation. The geophysical methods that have been used here include ground penetrating radar (GPR), airborne electromagnetic (AEM) and spectral induced polarization (SIP). The combination and integration of these different geophysical methods can provide solid constraints for the interpretation of the seismic results. Moreover this section presents how these different geophysical techniques provide complementary information concerning the near-surface lithology.

## 6.1 Interpretation of Refraction Tomography Result

Refraction tomography allows exploring near-surface information down to 50 meters below the ground surface. The interval velocity model (Figure 6.1) from the refraction tomography inversion shows a velocity gradient at about 10(12) m depth; this velocity gradient coincides approximately to a mixture of dry sand and till, and saturated sand interfaces in boreholes Tangstedt-3914 and B1, but not in borehole B2. In part of the model, from ~10 to ~25 m, minimal change in the velocity indicates more uniform and undisturbed lithology and this may correspond to the saturated sand layer in the borehole log. The velocity model also reveals two other velocity contrasts, i.e. at depth of about 25 and 50 m. The velocity gradient at about 25 m might be related to saturated sand and till interface in borehole log (Tangstedt-3914). The high-velocity zone between ~25 to ~50 m presents the till layer. The velocity gradient at about 50 m may be related to flakes of brown coal at 47 m in the borehole log borehole B1.

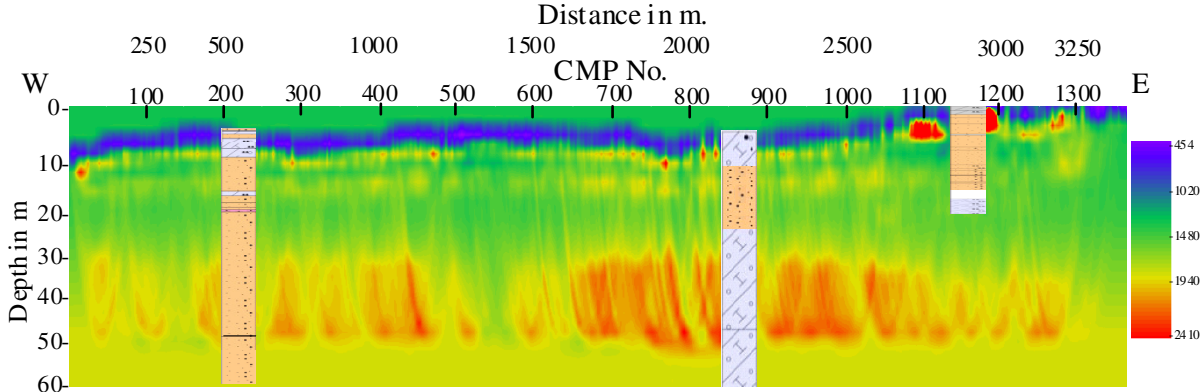


**Figure 6.1:** P-wave interval velocity model from the tomography inversion and the available boreholes (B1 (at 600 m), B2 (at 2800 m) and Tangstedt 3914 (at 2200 m)).

One can generalize that the resulting interval velocity model incorporated all important units observed in the boreholes and velocities in the expected ranges. These include: a surface layer with a mixture of dry sand, till and humus (~480 – ~1020 m/s); a uniform layer of saturated sand (~1480 – ~1700 m/s) and a till layer (~1800 – ~2400 m/s).

## **6.2 Combining $V_p$ , $V_s$ and $V_p/V_s$ with Borehole Logs and Previous VSP Results**

Jointly using P-wave and S-wave velocities can provide information about the lithology of the medium. Varying sensitivities for P-wave and S-wave velocities to the different properties of the medium allow the velocities to be utilized to image more effectively the sub-surface sequences. The ratio of  $V_p$  and  $V_s$  is known to be particularly sensitive to lithology, porosity and pore-fluid content, making it a useful parameter for evaluating and independently measuring those properties of rocks (see section 3.5). This section describes and evaluates the seismic attributes  $V_p$ ,  $V_s$ ,  $V_p$  to  $V_s$  velocity ratios for characterizing the shallow sub-surface. I try to correlate the available borehole data (section 2.2) to the results. I also seek the possible relations between the velocity models and the velocity ratios to the vertical seismic profile (VSP) results from previous studies in the area.

### **6.2.1 $V_p$ , $V_s$ and $V_p/V_s$ versus Lithology**

A detailed  $V_p$  and  $V_s$  interval velocity model (Figure 6.2a & b) is determined using the rms velocities from the shallow P- and S-wave reflection data (section 5.2). The rms velocities are manually adjusted by defining a polygon based on the dominant reflection boundaries. The interval velocity model is calculated with a velocity function defined at every 50th CMP. From the obtained  $V_p$  and  $V_s$  interval velocity models,  $V_p$  to  $V_s$  ratios (Figure 6.2 c) are calculated.

The P-wave interval velocity model (Figure 6.2a) indicates, in average, the velocities vary from low velocities (540 m/s) at the shallow depths to velocities 1700 m/s - 2250 m/s from 6 m to about 65 m depth. There are some patches of low velocities at ~ 20m depth but no significant lateral velocity variation in general. The S-wave interval velocity model (Figure 6.2b) reveals high and low velocity values (150 – 500 m/s). The low S-wave velocity anomalies are seen around 20 m and extend laterally with increase of thickness from small to higher CMP number. The  $V_p/V_s$  ratio varies in depth more distinctly than laterally (Figure 6.2c). The value generally ranges from 1.5 in the very near surface to almost 11 around 15 m depth with intermediate values elsewhere.

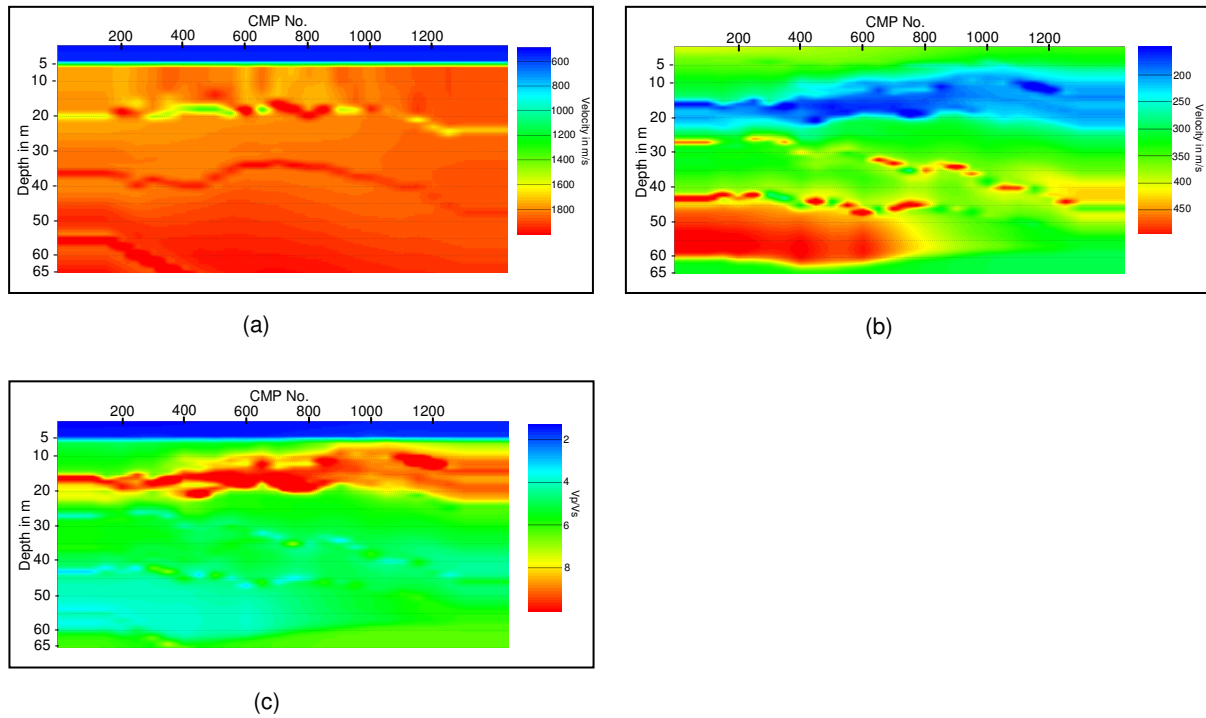


**Figure 6.2:** (a) P-wave interval velocity,  $V_p$ , (b) S-wave interval velocity,  $V_s$ , (c) P- to S-wave velocity ratio,  $V_p/V_s$ , for depth down to 65 m, respectively.

The calculated  $V_p/V_s$  ratios for the whole profile are shown in Table 6.1 for every 100 CMP and a depth interval of 5 m. The first obvious observation made from the table is that the  $V_p/V_s$  ratios increase until a depth of about 20 m and then decrease until 60 m with slight increases again below this depth. The  $V_p/V_s$  data has also been plotted (Figure 6.3) for the profile for depths between 1 and 65 m and interpreted in conjunction with the available borehole information. Even though the existing boreholes (Tangstedt-B2 and Tangstedt-3914) are not located exactly on the profile, it is observed that the result agrees well with the borehole data with some small depth variation in all the above depth ranges. The estimated average  $V_p/V_s$  ratios for the entire profile are 1.5-3.8 for the first 5 m depth section which corresponds to the mixture of sand and till; 7.6-8.7 between 10 and 20 m depth which correlates to the saturated sand column; 4.6-5.8 corresponding to the till layer and 5.2-6.2 to the clay section.

Depth (m)	CMP's																				
	100			200			300			400			500			600			700		
	V <sub>p</sub>	V <sub>s</sub>	V <sub>p</sub> / V <sub>s</sub>	V <sub>p</sub>	V <sub>s</sub>	V <sub>p</sub> / V <sub>s</sub>	V <sub>p</sub>	V <sub>s</sub>	V <sub>p</sub> / V <sub>s</sub>	V <sub>p</sub>	V <sub>s</sub>	V <sub>p</sub> / V <sub>s</sub>	V <sub>p</sub>	V <sub>s</sub>	V <sub>p</sub> / V <sub>s</sub>	V <sub>p</sub>	V <sub>s</sub>	V <sub>p</sub> / V <sub>s</sub>	V <sub>p</sub>	V <sub>s</sub>	V <sub>p</sub> / V <sub>s</sub>
1	543.0	391.2	1.4	543.0	388.3	1.4	543.0	383.5	1.4	543.0	380.6	1.4	543.0	376.5	1.4	543.0	372.3	1.5	543.0	366.0	1.5
5	1160.0	352.3	3.3	1135.9	353.6	3.2	1177.3	352.3	3.3	1191.8	340.4	3.5	1178.3	353.2	3.3	1132.1	332.4	3.4	1142.7	326.2	3.5
10	1766.0	316.7	5.6	1718.1	312.6	5.5	1801.1	312.0	5.8	1825.1	252.5	7.2	1803.7	260.6	6.9	1714.1	207.0	8.3	1713.3	220.9	7.8
15	1772.9	232.3	7.6	1720.6	264.4	6.5	1805.6	274.0	6.6	1784.2	184.5	9.7	1901.3	174.9	10.9	1718.2	176.1	9.8	1835.2	175.4	10.5
20	1559.1	207.4	7.5	1871.1	228.4	8.2	1486.7	223.0	6.7	1780.0	195.3	9.1	1775.5	208.4	8.5	1863.4	286.3	6.5	1785.7	256.0	7.0
25	1768.3	308.0	5.7	1773.2	300.5	5.9	1775.7	365.2	4.9	1785.2	275.8	6.5	1793.2	302.3	5.9	1803.8	312.9	5.8	1805.5	316.8	5.7
30	1829.7	321.4	5.7	1818.8	330.4	5.5	1807.2	333.4	5.4	1802.2	430.6	4.2	1810.4	380.1	4.8	1816.2	355.9	5.1	1813.1	352.8	5.1
35	1851.7	325.8	5.7	1821.5	329.8	5.5	1808.1	341.7	5.3	1805.0	341.9	5.3	1814.1	347.3	5.2	1859.1	352.6	5.3	1832.5	383.6	4.8
40	1795.5	361.4	5.0	1797.1	370.4	4.9	1809.7	379.3	4.8	1959.0	371.0	5.3	1825.2	385.3	4.7	1856.4	351.5	5.3	1851.4	367.0	5.0
45	1877.8	420.9	4.5	1850.4	422.2	4.4	1847.0	434.6	4.3	1863.9	311.1	6.0	1884.3	352.4	5.3	1890.4	386.6	4.9	1882.6	436.8	4.3
50	1934.1	479.8	4.0	1921.7	475.7	4.0	1896.4	465.4	4.1	1901.9	467.0	4.1	1910.8	447.8	4.3	1913.9	455.0	4.2	1908.1	422.4	4.5
55	2164.5	510.5	4.2	1891.2	504.6	3.7	1928.4	489.2	3.9	1935.7	496.6	3.9	1936.5	472.3	4.1	1938.5	486.5	4.0	1934.8	444.9	4.3
60	1888.4	417.1	4.5	1854.8	449.2	4.1	1942.8	454.4	4.3	1947.9	496.3	3.9	1961.3	468.5	4.2	1963.4	478.8	4.1	1961.3	412.4	4.8
65	1980.6	318.2	6.2	1934.2	321.6	6.0	1870.6	325.7	5.7	2203.3	331.8	6.6	1938.6	331.3	5.9	1975.2	324.1	6.1	1987.0	319.0	6.2



Depth (m)	CMP's																		
	800			900			1000			1100			1200			1300			Average
	V <sub>p</sub>	V <sub>s</sub>	V <sub>p</sub> / V <sub>s</sub>	V <sub>p</sub>	V <sub>s</sub>	V <sub>p</sub> / V <sub>s</sub>	V <sub>p</sub>	V <sub>s</sub>	V <sub>p</sub> / V <sub>s</sub>	V <sub>p</sub>	V <sub>s</sub>	V <sub>p</sub> / V <sub>s</sub>	V <sub>p</sub>	V <sub>s</sub>	V <sub>p</sub> / V <sub>s</sub>	V <sub>p</sub>	V <sub>s</sub>	V <sub>p</sub> / V <sub>s</sub>	V <sub>p</sub> / V <sub>s</sub>
1	543.0	358.0	1.5	543.0	348.6	1.6	543.0	339.9	1.6	543.0	337.2	1.6	543.0	337.4	1.6	543.0	339.8	1.6	1.5
5	1163.9	267.2	4.4	1205.3	265.2	4.5	1178.3	264.5	4.5	1200.5	282.0	4.3	1215.9	290.7	4.2	1213.0	304.7	4.0	3.8
10	1761.3	207.0	8.5	1851.3	206.2	9.0	1800.1	209.9	8.6	1744.1	202.5	8.6	1877.7	214.1	8.8	1871.9	224.7	8.3	7.6
15	1725.1	181.5	9.5	1777.1	201.3	8.8	1794.8	208.6	8.6	1761.8	231.2	7.6	1865.2	213.8	8.7	1872.9	207.0	9.0	8.7
20	2064.4	223.6	9.2	1784.6	293.7	6.1	1820.8	255.7	7.1	1775.3	246.5	6.8	1858.3	220.9	8.4	1873.6	209.2	9.0	7.7
25	1801.9	322.5	5.6	1809.4	323.8	5.6	1822.9	313.2	5.8	1838.1	310.3	5.9	1828.9	299.6	6.1	1801.6	283.5	6.4	5.8
30	1822.0	344.1	5.3	1822.7	349.4	5.2	1832.2	335.0	5.5	1843.6	340.4	5.4	1854.0	342.5	5.4	1859.9	326.1	5.7	5.2
35	1949.8	478.9	4.1	1913.5	416.3	4.6	1832.1	360.8	5.1	1848.3	380.4	4.9	1861.0	386.3	4.8	1864.3	359.4	5.2	5.1
40	1836.6	380.2	4.8	1830.7	359.0	5.1	1833.8	387.0	4.7	1918.7	496.7	3.9	1859.6	405.9	4.6	1868.5	420.6	4.4	4.8
45	1866.6	459.4	4.1	1854.0	369.0	5.0	1848.2	374.3	4.9	1850.7	372.0	5.0	1864.6	387.7	4.8	1868.1	376.9	5.0	4.8
50	1892.5	391.1	4.8	1878.2	365.1	5.1	1868.2	346.0	5.4	1863.8	316.8	5.9	1866.1	347.3	5.4	1865.9	379.9	4.9	4.7
55	1921.8	408.6	4.7	1908.4	380.5	5.0	1895.4	359.9	5.3	1885.7	337.2	5.6	1884.0	322.4	5.8	1876.0	318.2	5.9	4.6
60	1949.7	347.4	5.6	1937.1	314.3	6.2	1923.2	304.0	6.3	1912.4	313.5	6.1	1909.4	300.5	6.4	1897.6	312.1	6.1	5.1
65	1979.1	312.8	6.3	1966.9	307.1	6.4	1950.6	303.1	6.4	1937.2	301.4	6.4	1933.6	306.9	6.3	1924.6	300.3	6.4	6.2

**Table 6.1:** V<sub>p</sub>, V<sub>s</sub> and V<sub>p</sub> to V<sub>s</sub> ratio along the shallow P- and S-wave reflection profile (Figure 5.16) for the depth range 0 to 65 m, every 100 CMPs.

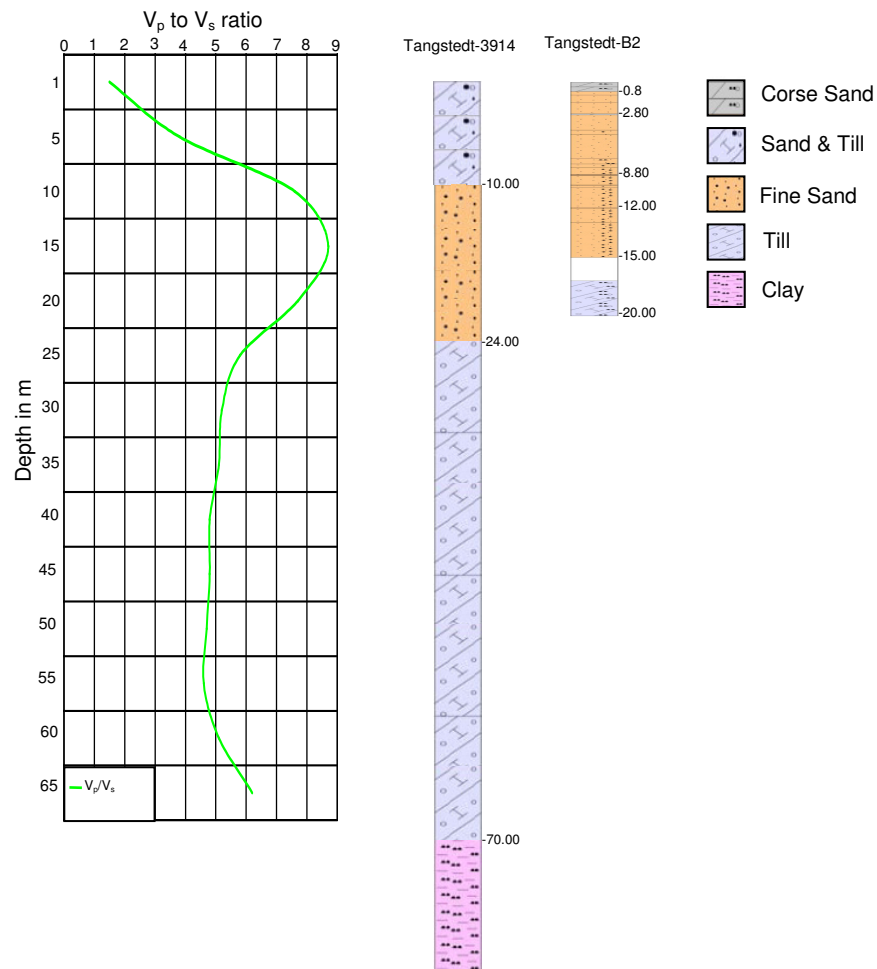


**Figure 6.3:** Plots of average P- to S-wave velocity ratio,  $V_p/V_s$  for the entire profile taken every 100 CMPs for a depth down to 65 m with lithology profiles from the nearest borehole logs: Tangstedt-B2 (depth 20 m) and Tangstedt-3914 (only 80 m depth displayed).

To assess the relevance of the velocities with regard to the lithology and to verify further the  $V_p/V_s$  result, a comparison between these values at particular CMPs has been made. The nearest CMPs to the boreholes Tangstedt-B2 and Tangstedt-3419 are CMP 150 and 1300, respectively. The P- and S-wave interval velocities and P- to S-wave velocity ratios at those CMPs (CMP 150 and 1300) are shown in Table 6.2 and the corresponding plots in Figure 6.4 and 6.5. From visual inspection the  $V_p$ ,  $V_s$  and  $V_p/V_s$  plots (Figures 6.4 and 6.5) correlate well with significant lithologic boundaries noted in the borehole log at depths of 15 (Tangstedt-B2), 10 and 24 m (Tangstedt-3419).

The result indicates the S-wave velocity and the P- to S-wave velocity ratio exhibit more variation compared to the P-wave velocity. The  $V_s$  plots show a pattern of decrease/increase/decrease and the opposite increase/decrease/increase effect on  $V_p/V_s$  for the whole depth range. The saturated sandy layer between 10 to 24 m (Figure 6.4 & 6.5) seems to be related to high P-wave velocity, low S-wave velocity, and high  $V_p/V_s$  ratio anomalies. The observed high values in  $V_p/V_s$  ratio are due to low S-wave velocities which can be explained by water saturation of the rocks (the water table is located at about 2 to 3 m below the surface). When a rock is saturated by a fluid, the fluid may either soften or harden the matrix (Wang, 2000). The softening/hardening occurs only for the shear modulus, as a result the dependence of S-wave velocity on pore fluid. This coupling of pore fluid to the S-wave velocity is interpreted as a manifestation of the effect of fluid interaction on the solid matrix (see section 3.1).

The thin layer with P-wave velocity of about 2000 m/s, S-wave velocity of about 500 m/s and P- to S-wave velocity ratio of 4.3 at 35 to 45 m depth at CMP 150 (Figure 6.4) or with P-wave velocity of about 1980 m/s, S-wave velocity of about 470 m/s and P- to S-wave velocity ratio of 4.2 at 50 to 60 m depth at CMP 1300 (Figure 6.5) are not observed in the borehole data. In general the depth interval between 25 to 60 m with high P- and S-wave velocity and low P- to S-wave velocity ratio may represent the till layer, whereas the increase of  $V_p$  to  $V_s$  ratio above 60 m depth may show the till clay interface in the borehole log. The result as a whole signifies that the P- and S-wave interval velocity model together with the velocity ratio can be considered to be reliable without knowledge of the borehole data.

Depth (m)	$V_p$ (m/s)	$V_s$ (m/s)	$V_p/V_s$
1	543.0	390.0	1.4
5	1160.0	353.5	3.3
10	1766.0	319.7	5.5
15	1772.9	284.8	6.2
20	1559.1	220.1	7.1
25	1768.3	305.2	5.8
30	1829.7	329.2	5.6
35	1851.7	333.1	5.6
40	1795.5	373.9	4.8
45	1877.8	436.8	4.3
50	1934.1	476.6	4.1
55	2164.5	504.4	4.3
60	1888.4	409.7	4.6
65	1980.6	319.8	6.2

(a)

Depth (m)	$V_p$ (m/s)	$V_s$ (m/s)	$V_p/V_s$
1	543.0	339.8	1.6
5	1213.0	304.7	4.0
10	1871.9	224.7	8.3
15	1872.9	209.2	8.9
20	1873.6	207.0	9.1
25	1801.6	283.5	6.4
30	1859.9	326.1	5.7
35	1864.3	359.4	5.2
40	1868.5	420.6	4.4
45	1868.1	376.9	5.0
50	1865.9	379.9	4.9
55	1876.0	348.2	5.3
60	1897.6	312.1	6.1
65	1921.9	300.3	6.4

(b)

**Table 6.2:**  $V_p$ ,  $V_s$  and  $V_p/V_s$  values (a) at CMP 150, (b) at CMP 1300.

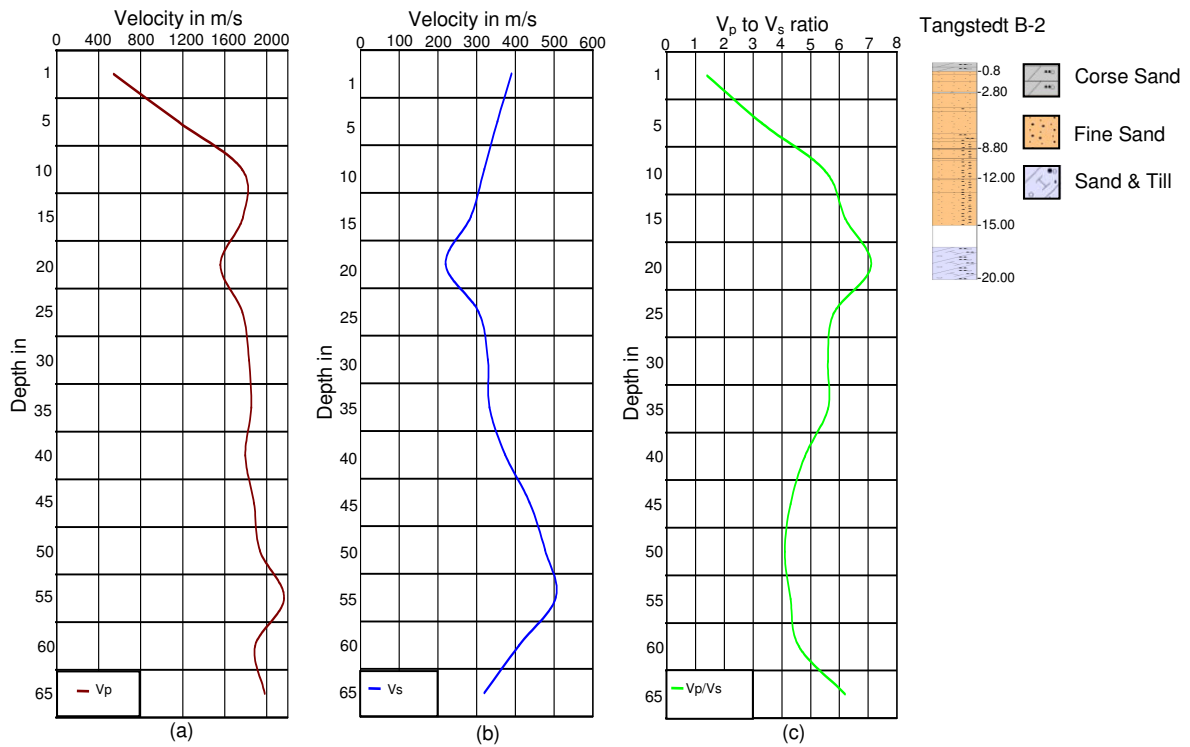


Figure 6.4: Plots of (a) P-wave velocity, (b) S-wave velocity, (c) P- to S-wave velocity ratio versus depth at CMP 150 and lithology log for the nearest borehole to CMP 150.

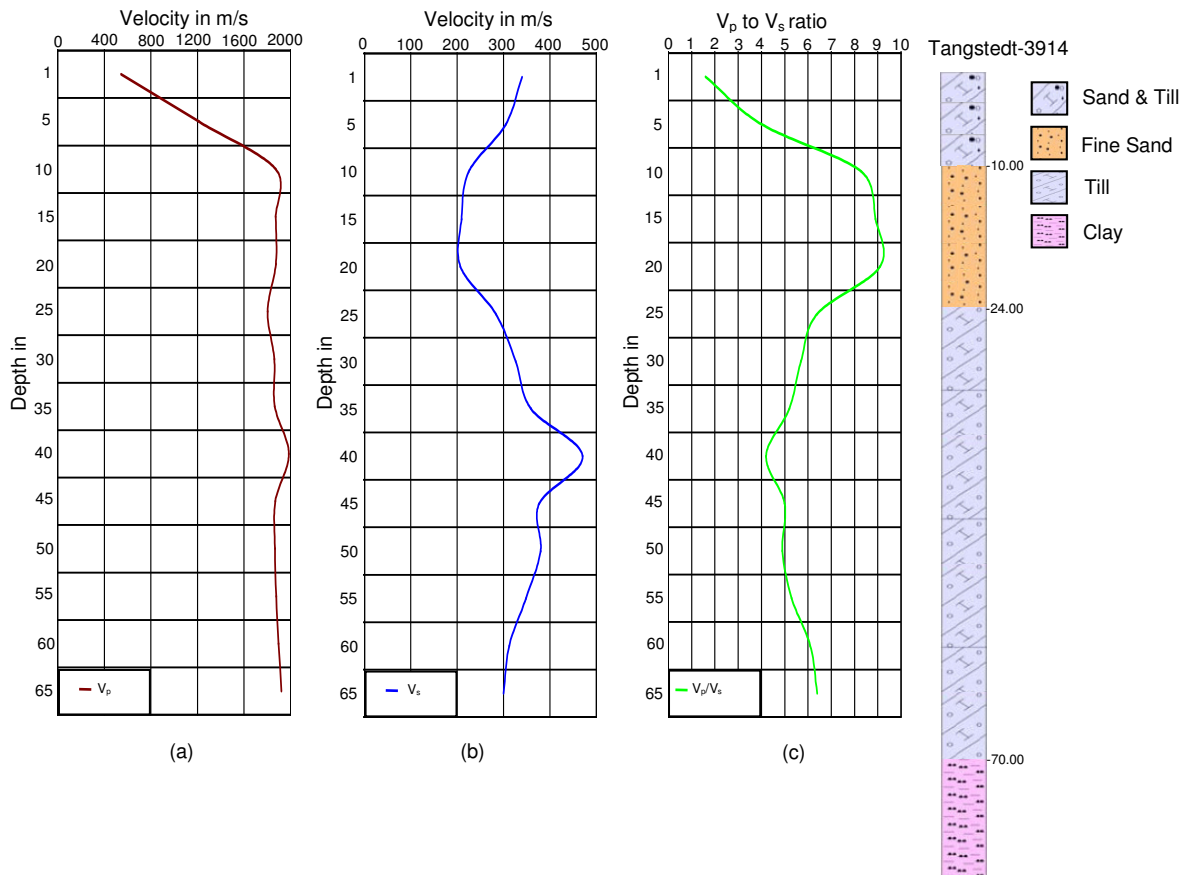
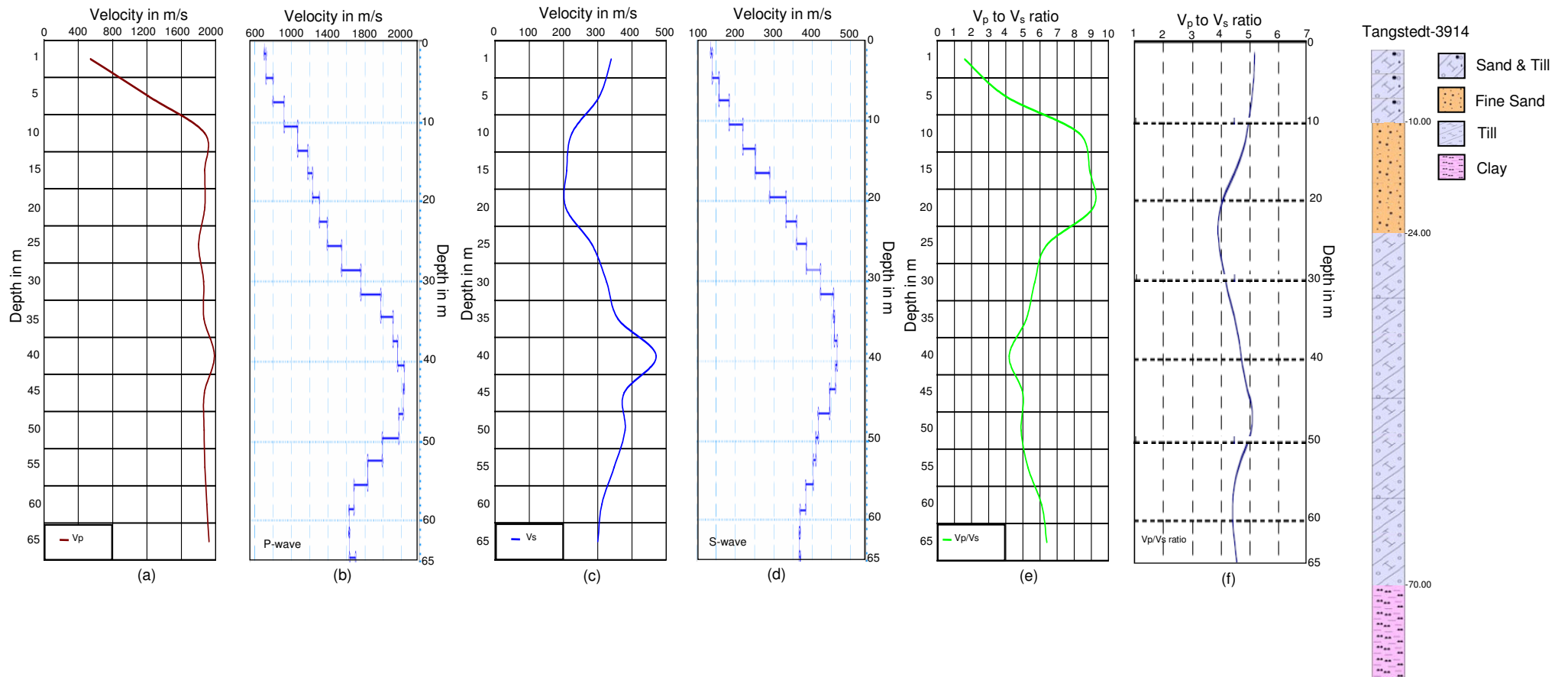


Figure 6.5: Plots of (a) P-wave velocity, (b) S-wave velocity, (c) P- to S-wave velocity ratio versus depth at CMP 1300 and lithology log for the nearest borehole to CMP 1300.

### 6.2.2 Comparing with Previous VSP Results

The available data, in particular the  $V_p$  and  $V_s$  velocity depth functions and the  $V_p$  to  $V_s$  ratios derived from the VSP measurement in the borehole Tangstedt-3914 (Rumpel et al., 2005) is compared with the above  $V_p$  and  $V_s$  velocities and the  $V_p$  to  $V_s$  ratios determined. The interval velocities and the velocity ratio from both data set show analogous results. As shown in Figure 6.6 there are some strong similarities in the two velocity functions. For example, the  $V_p$  and  $V_s$  interval velocities functions for the two methods within the range of depths 30 to 60 m are following a similar trend and tracking each other. In both cases the velocities vary from about 1800 to 2000 m/s ( $V_p$ ) and 300 to 500 m/s ( $V_s$ ) in the above depth ranges. Besides the higher velocity ( $V_p \sim 2000$  m/s,  $V_s \sim 500$  m/s) at about 40 m depth in the shallow reflection data was also detected in the VSP method.

The interval P- and S-wave velocities for the very near-surface (above  $\sim 30$  m depth) are also compared and no agreement was found. The prominent difference between the two results is the presence of an S-wave velocity inversion at about 10 to 25 m depth in the shallow reflection data that was not observed in the VSP result. For  $V_p$  to  $V_s$  ratio the values for the two methods agree below  $\sim 30$  m depth and disagree above this depth. Generally the results from the two methods are in good agreement except for the very near-surface area which is possibly because of a lack in good resolution of the VSP data in this depth range (this may be due to the poor first break picks for the first 20 m in the VSP data).



**Figure 6.6:**  $V_p$  and  $V_s$  interval velocities and  $V_p$  to  $V_s$  velocity ratios for the shallow surface seismic data at CMP 1300 (a, c & e) and from VSP results in borehole Tangstedt-3914 (b, d & f) (Rumpel et al., 2005a).

### 6.3 Description of other Geophysical Results in the Study Area

Ground penetrating radar (GPR), airborne electromagnetics (AEM) and spectral induced polarisation (SIP) data were acquired in the same location where the shallow P- and S-wave data were collected (Figure 6.7). Short descriptions of these data are presented in the following.

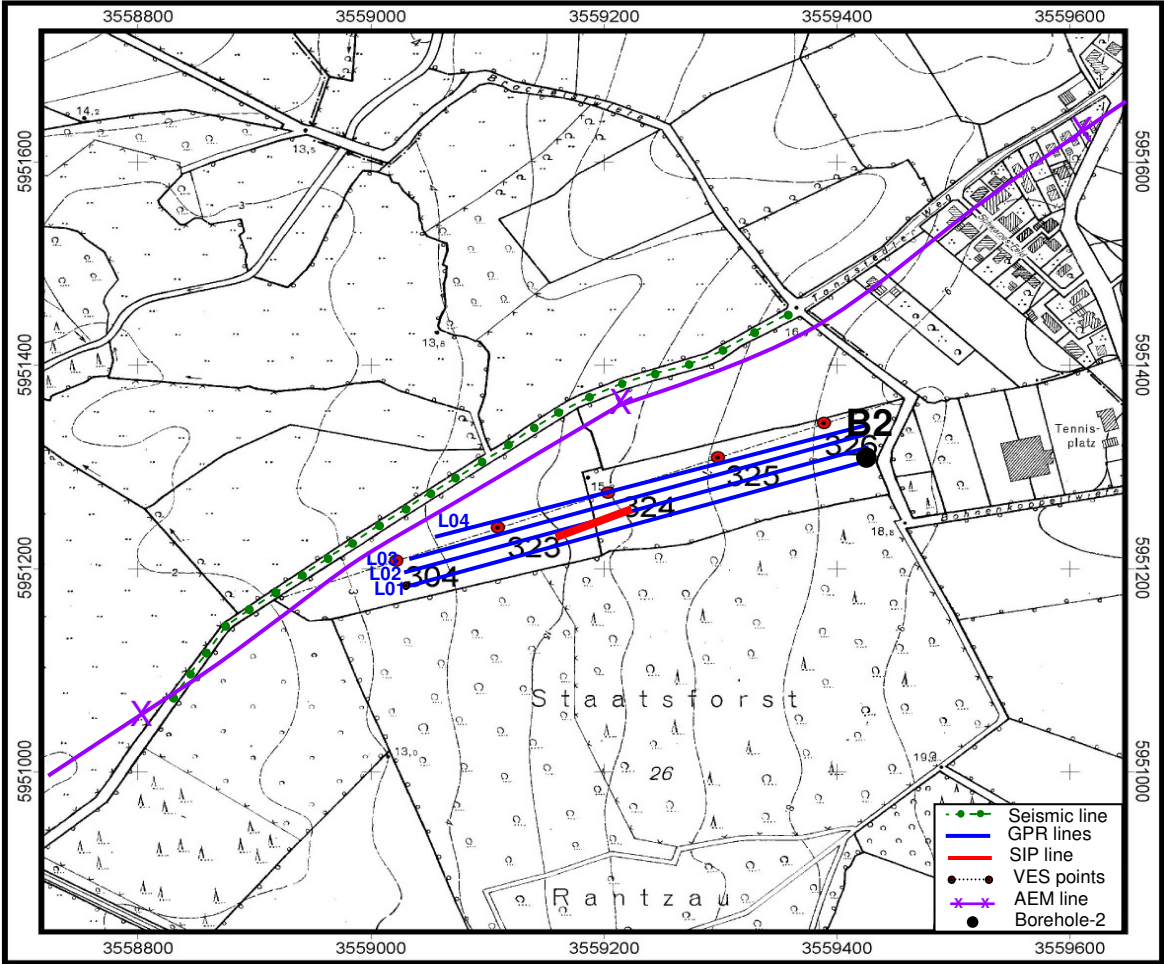


**Figure 6.7:** Profile map of seismic, GPR, SIP, VES and AEM lines and location of Borehole-2 in the survey area Tangstedt.

### Ground penetrating radar (GPR)

The GPR data were acquired along four profiles by the Geological Survey of Denmark and Greenland (Møller, 2006) in October 2005. The lengths of the lines are about 400 m and are orientated roughly E-W parallel to each other (Figure 6.7). A number of common mid point, CMP, gathers were collected with a spacing of 0.5 m between the adjacent CMP's. The survey was carried out with nominal center frequency of 100 MHz.

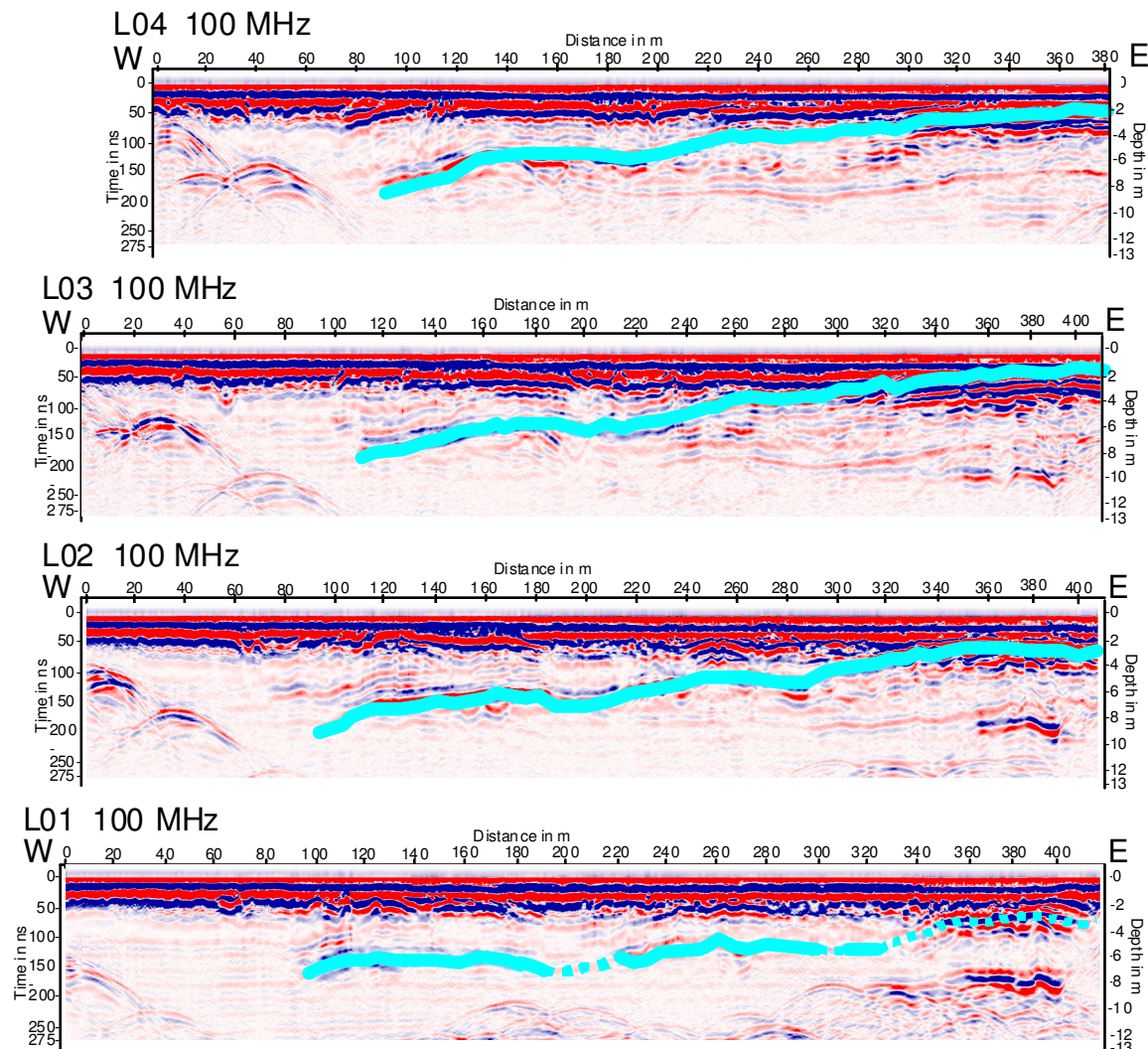


**Figure 6.8:** The GPR profiles L01-L04 collected with 100 Hz. The cyan lines mark a dipping reflection that can be recognized in all GPR profiles (Møller, 2006).



A standard processing is applied to the data and the velocities are evaluated through a simple curve matching of reflection hyperbolas for selected CMPs. The rms velocities are varying between 0.07 m/ns to 0.09 m/ns, with the majority of the CMP's having rms velocities of about 0.09 m/ns. The GPR profiles (L01- L04) have dominating penetration depth about 175 ns (~ 7.9 m) (Figure 6.8). In most of the GPR profiles continuous westward dipping reflections are seen. For example clear reflections are seen down to nearly 200 ns reflection time (or depths of about 8 m) in the sandy part (Møller, 2006).

#### *Airborne Electromagnetic (AEM)*

A helicopter-borne survey was conducted in the Ellerbeker Rinne survey area by the airborne group of the German Federal Institute for Geosciences and Natural Resources (BGR) in April 2005 and in May 2006 (Siemon et al., 2006). The airborne survey comprises an 8-12 km by 28 km wide area. There were 7 flights with 99 ENE–WSW profile lines of flight-line spacing 400/600 m and total length 893 km. The mean flight altitude of the electromagnet sensor above ground was 50 m. The AEM results are presented on maps and as vertical resistivity sections (VRS). From these results the resistivity distribution of the upper 70 m is obtained.

Figure 6.7 shows part of the flightline (profile number 258.1) close to the seismic profile Tangstedt. The resistivity cross-section along this flightline is displayed in Figure 6.9. The colour code red to orange (resistivity of more than 70  $\Omega\text{m}$ ) indicates dry and saturated sand, yellow to green (30 – 70  $\Omega\text{m}$ ) indicates till, and blue (resistivity below 30  $\Omega\text{m}$ ) indicates clay or saltwater saturated sediment. At a depth of 0 m bsl (Figure 6.9) the lateral resistivity distribution indicates mostly till and sand (Scheer et al., 2006 ).

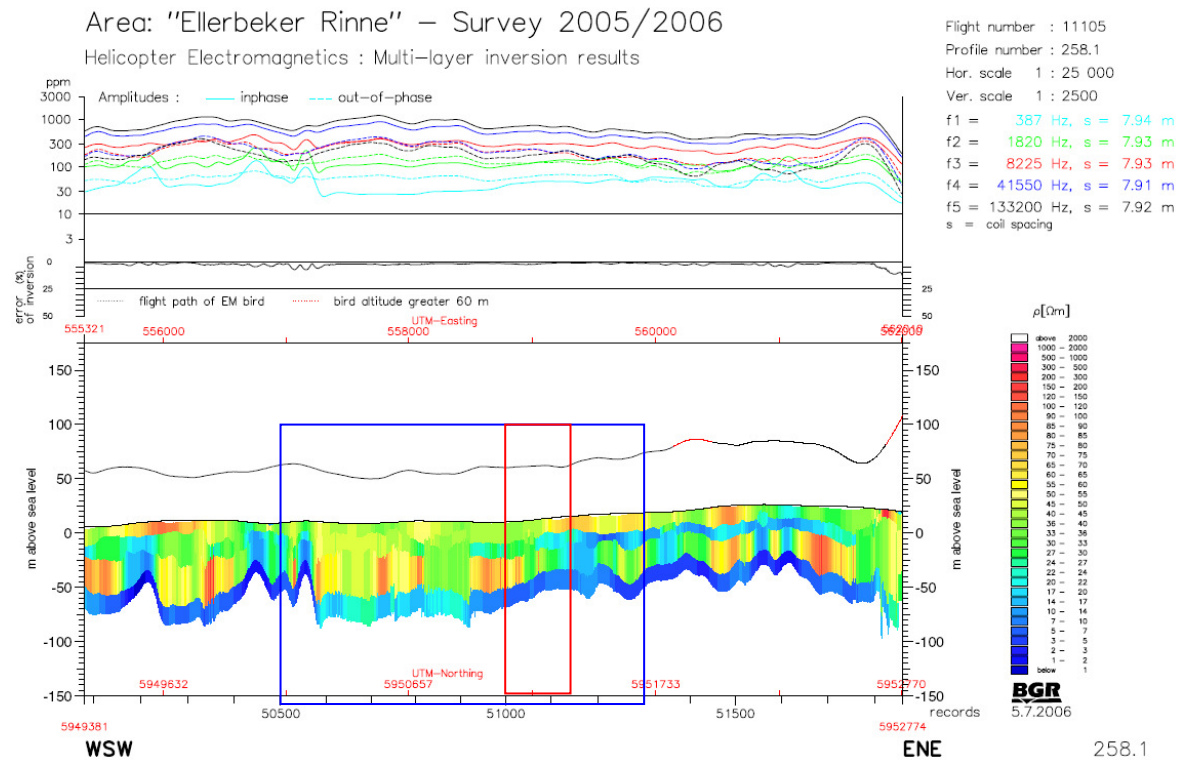


**Figure 6.9:** AEM resistivity cross-section along the flightline (profile number 258.1) close to the seismic profile Tangstedt (Siemon et al., 2006), blue box corresponds to Tangstedt P-wave profile 2005 and red box corresponds to Tangstedt shallow P- and S-wave profile 2006.

### Spectral induced polarisation (SIP)

SIP measurements were carried out in November 2007 by TU Braunschweig (Hoerdt et al., 2007). The overall SIP profile has a length of 84 m with an electrode spacing of 3 m. Spectral measurements were carried out using a frequency range typically between 0.1 Hz and 1 kHz. The data were inverted separately for each frequency with a 2-D finite element code using a particular regularization that supports sharp boundaries. Figure 6.10 shows the inversion result from Hoerdt et al. (2007). The aquifer between 5 and 12 m is characterized by resistivities of several 100 Ωm and phase values between -15 and -20 mrad. The aquifer consists of intermediate sand; glacial till forms the base at about 12 m depth (Hoerdt et al., 2007).

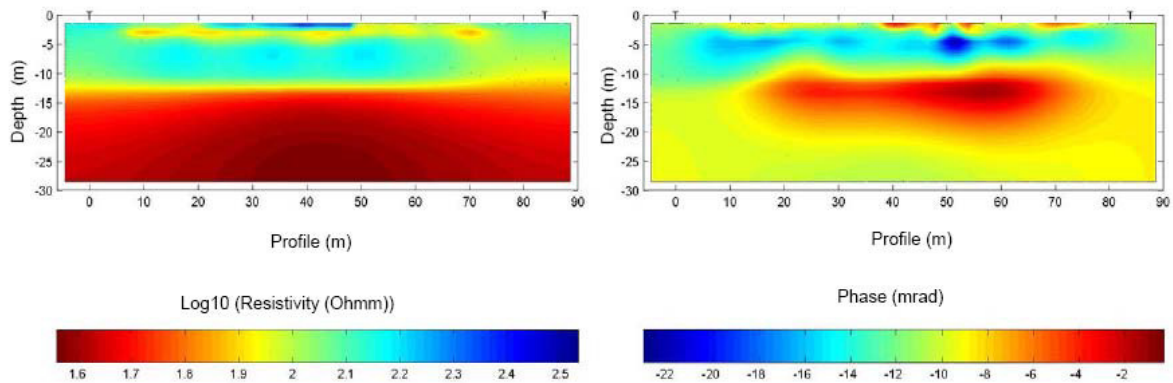


**Figure 6.10:** Inversion result along a profile at the Hasloh test site (Figure 6.7) for frequency of 1.25 Hz. Left panel: Resistivity magnitude, right panel: resistivity phase shift (Hoerd et al., 2007).

#### 6.4 An Integrated Interpretation of the Geophysical Results

The uses of more than one geophysical method have resulted in a more accurate definition and representation of the subsurface than a single method can provide. Here a combined interpretation of different geophysical results - refraction tomography, shallow P- and S- wave reflection, GPR, AEM and SIP - are performed to demonstrate how they complement each other to characterize the near-surface lithology. The comparison was made in two groups because of the different resolution of the methods. First between the GPR, shallow S-wave reflection (SSR) and SIP data and then between the refraction tomography, shallow P-wave reflection (SPR) and AEM data. The profiles investigated using these geophysical methods are shown in Figure 6.7 GPR (blue), shallow P- and S-wave reflection (green), SIP (red), and AEM (purple).

The SSR profile (Figure 6.11a) shows a slightly dipping shallow reflection at about 4 m. There is also a sharp change in velocity (velocity inversion) where the water saturated sandy layer appears. Below this at about 25 m there is a dipping reflection which is interpreted as the sand till interface according to the lithologic log of borehole Tangstedt-3914. There is also another reflection at about 50 m depth which has no corresponding stratum in the available boreholes near the profile, B1 and Tangstedt-3914.

The SIP profiles supply information of the subsurface until about 30 m depth (Hoerd et al., 2007). In Figure 6.11c two formations can be observed: An upper, high resistive layer (100 – 200  $\Omega$ m; logarithmic resistivity, in  $\Omega$ m, equal to 2.0 – 2.3) and a lower, less resistive layer (40 – 80

$\Omega$ m; logarithmic resistivity equal to 1.6 – 1.9) correspond to the fine sand and glacial till layers, respectively. In addition the model depicts the ground water table at about 2 m.

Figure 6.11b shows the 100 MHz GPR profile, where a strong reflector around 8 m of depth dipping towards the West, can be observed. This reflector is probably related with the top of the saturated sandy layer (Møller, 2006).

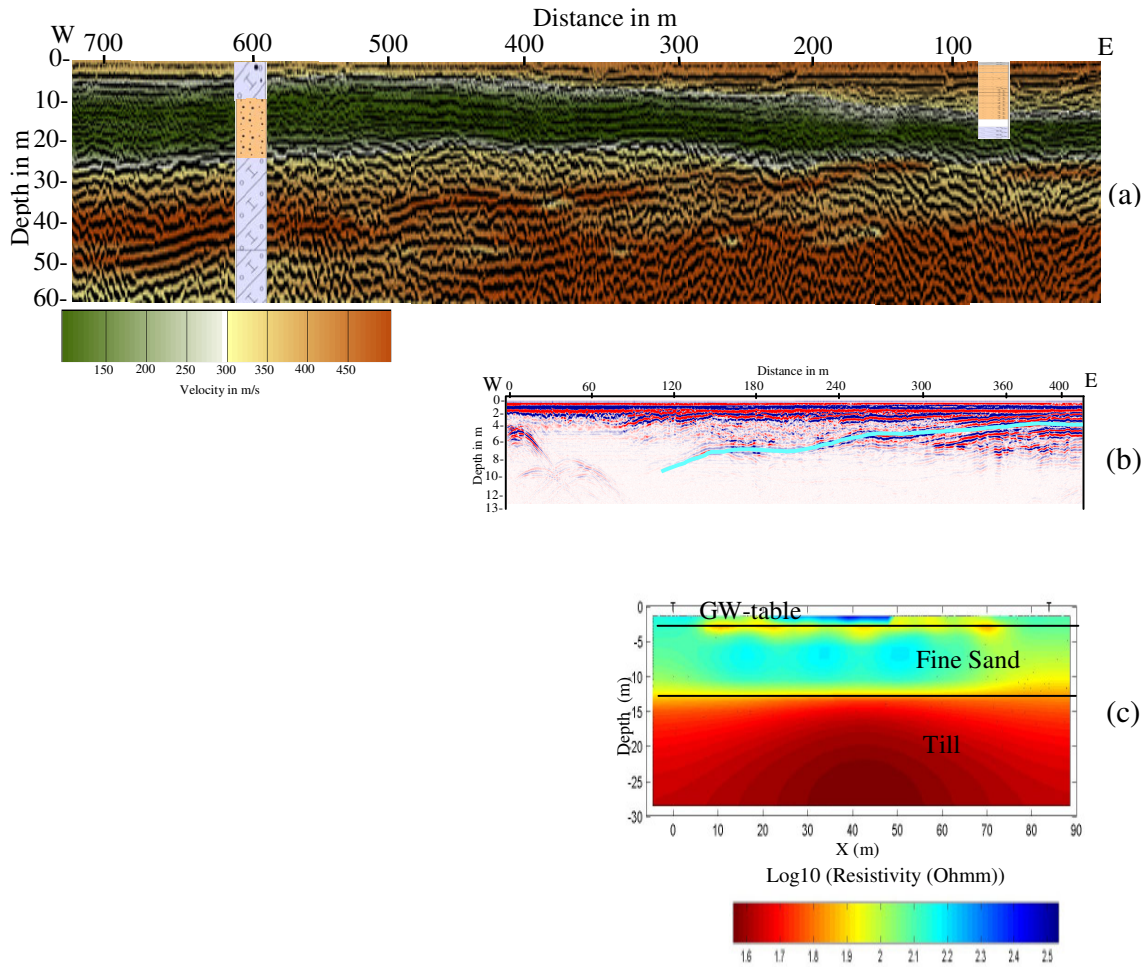


**Figure 6.11:** (a) Shallow S-wave reflection (720 m long) (b) GPR section (400 m long) with interpretation (Møller, 2006) (c) SIP (84 m long) interpreted result (Hoerd et al., 2007).

The SSR, GPR and SIP inversion results are merged into a single section (Figure 6.12), which provide a more complete image of the near-surface (~30 m). Since the SIP profile has a length of 84 m, only the parts of the SSR and GPR profile matching to the SIP profile are combined. As Figure 6.12 depicts the three geophysical methods image successfully the top of the saturated

sand zone. It can also be observed that there is a good agreement between the SSR section and the SIP model with minor depth deviations. The high resistivity layer (100 – 200  $\Omega\text{m}$ ) between 5 and 12 m, which is interpreted as sand layer, agrees with the low S-wave velocity strata (150 – 200 m/s). The till layer of resistivity between 40 – 80  $\Omega\text{m}$  coincides with the S-wave velocity layer of velocity 350 – 400 m/s.

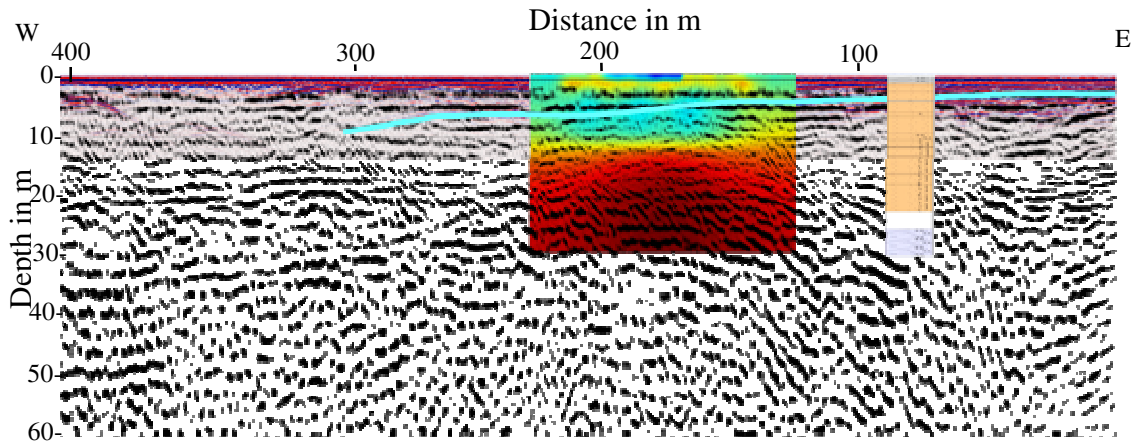


**Figure 6.12:** The GPR profile (the cyan line indicates the reflection) (Møller, 2006), the SIP resistivity section (Hoerdt et al., 2007) and the nearby borehole B2 superimposed on part of the S-wave reflection depth section.

A combined interpretation of the second group of geophysical methods - shallow P-wave seismic reflection (SPR), refraction tomography and airborne electromagnetic (AEM) - are presented as follows.

The SPR seismic section, shown in Figure 6.13a, displays a sequence of reflected events down to a depth of 100 m. The shallowest reflection at about 25 m is produced at the interface between the saturated sand and the till layers as it can be seen in the lithologic log (borehole Tangstedt-3914). The next strong reflection is revealed at about 50 m depth, but with no corresponding interface from the borehole log. The other prominent reflections are from depths of 60 to 70 m and 100 m generally correlate with significant lithologic boundaries noted in the borehole at depths of 70 (till/clay boundary) and 113 m (clay/sand boundary), respectively.

The results of the shallow P-wave seismic reflection can also be interpreted from the interval velocity shown in Figure 6.13a. Accordingly three seismic layers have been delineated and correlated with the borehole log. This included a saturated sand layer of velocities 1450 – 1700 m/s, a 45 m thick layer of till (1800 – 2000 m/s) and a clay layer (2000 – 2500 m/s).

As it has been discussed in section 5.1.1 the tomography refraction method shows three velocity zones (Figure 6.13b). From the surface to an approximate depth of 10 m the velocity increases from 450 to 1020 m/s and can be interpreted as a mixture of sand and till. The velocity in the second layer (~10 – 30 m) ranges from about 1480 to 1700 m/s, which is commonly found in water-saturated sand. The velocity layer between 30 and 50 m depth with a velocity of 1800 to 2400 m/s seems to be related to the till layer in the borehole section.

Even though the AEM resistivity cross-section has considerable lateral variation, it can be grouped into two environments. The first environment extends from 0 to 400 m and the second from 400 to 720 m along the profile. The first environment reveals three resistivity zones with high (70 – 100  $\Omega\text{m}$ ), medium (20 – 40  $\Omega\text{m}$ ) and low resistivity (3 – 10  $\Omega\text{m}$ ) down to a depth of 70 m. These resistivities indicate sand, a mixture of clay\till and a clay layer respectively, according to the colour code explanation in BurVal working group report (Scheer et al., 2006). In the second environment also three zones can be noticed. In the near surface, at depths down to 25 m, a resistivity of 20 to 40  $\Omega\text{m}$  (till) is observed. The second zone extends in a depth range of 25 to 50 m, with resistivities from 45 to 70  $\Omega\text{m}$  (sand). The third zone extends between 50 and 70 m, and is characterised by low resistivities, namely 3 – 20  $\Omega\text{m}$  (clay). The two environments are in agreement with the borehole section for the first 10 m depth and at 70 m but they are inconsistent for the other depths.

Figures 6.13 and 6.14 give a complete view of the combined cross-section established from refraction tomography, SPR and AEM. The three methods are in good agreement especially in the western side of the profile among one another and also with the borehole section. At an average depth of 10 m the layer boundary between till and sand is clearly marked by the refraction tomography and AEM methods. The next layer boundary at ~ 25 m is noticed with the three methods and the borehole section as well. The boundary at ~50 m is recognized by refraction tomography, SPR and AEM, and at ~70 m by SPR, AEM and the borehole Tangstedt-3914.

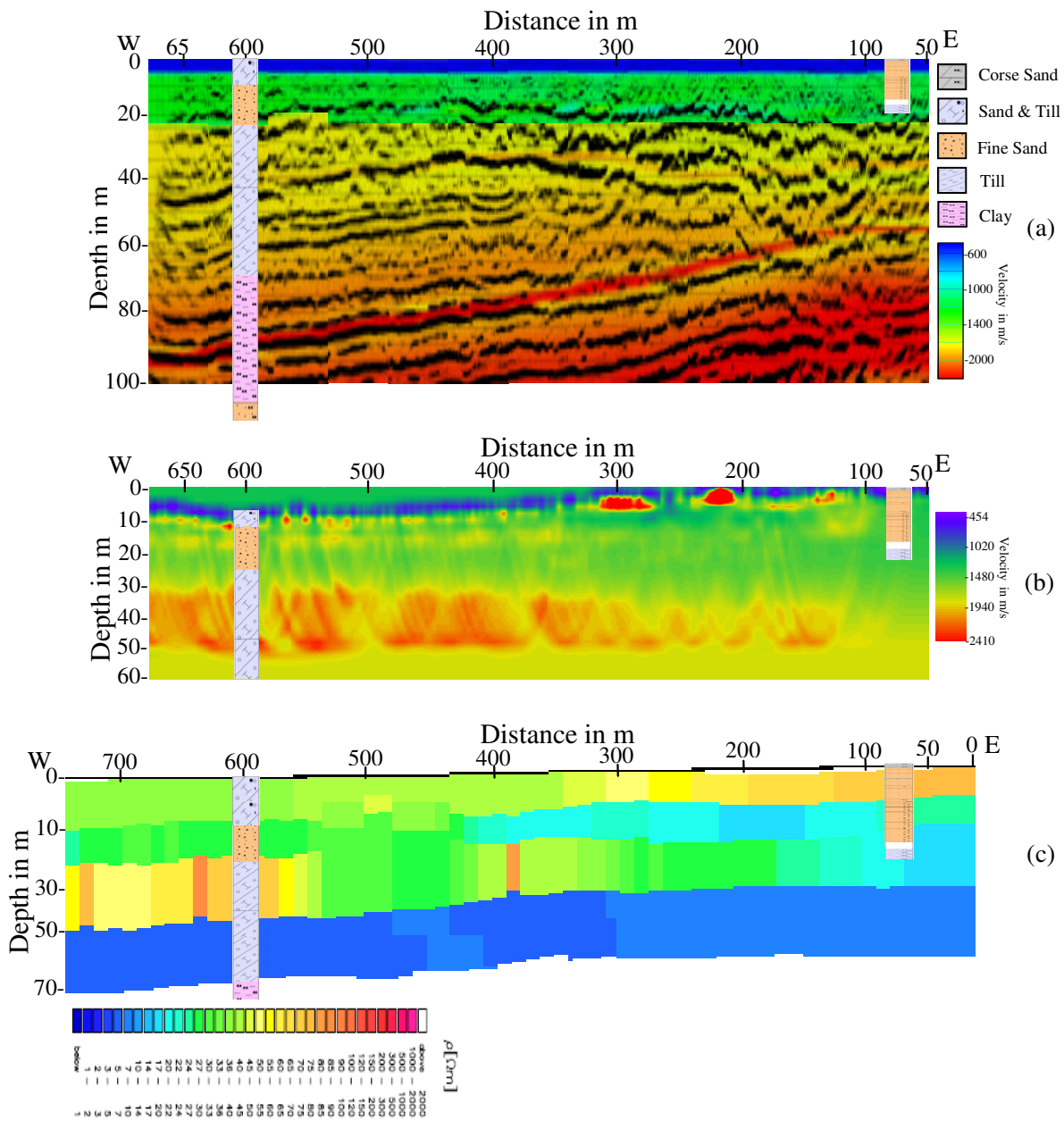


**Figure 6.13:** (a) Shallow P-wave reflection depth section with the interval velocities. (b) Refraction tomography velocity model. (c) AEM resistivity cross-section (Siemon et al., 2006). Part of the AEM and refraction tomography profile that overlap the SPR profile is displayed here as well as the nearby lithology logs from borehole B1 (at 75 m) and Tangstedt-3914 (at 600 m).

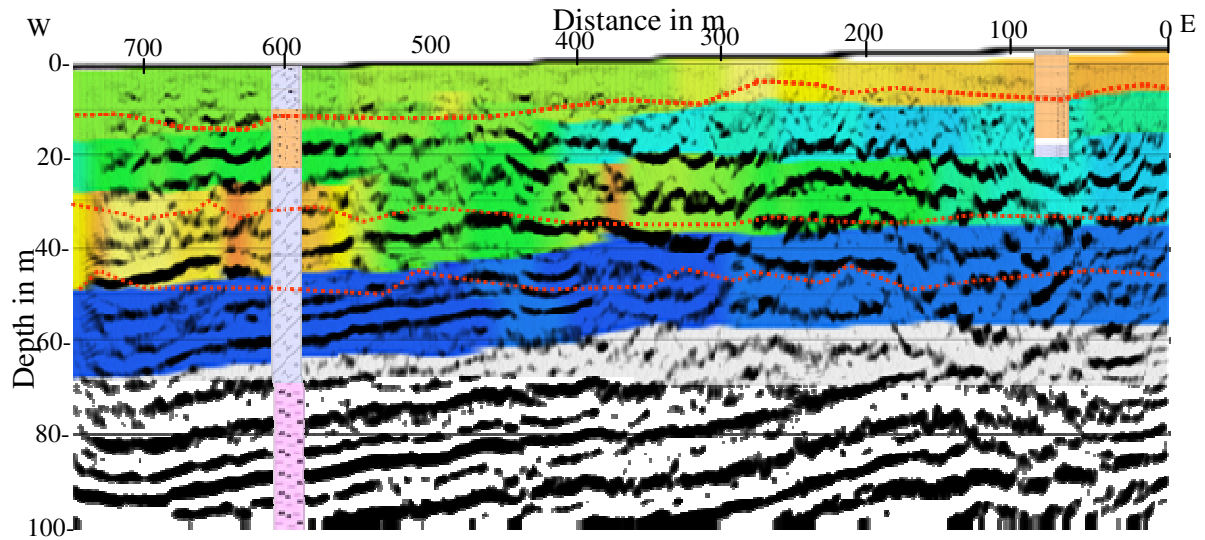


**Figure 6.14:** The shallowest refraction tomography boundary (~10 m, red dotted line), AEM resistivity cross-section and the lithologic log from borehole B2 (at 75 m) and Tangstedt-3914 (at 600 m) are inserted in the P-wave reflections depth section.

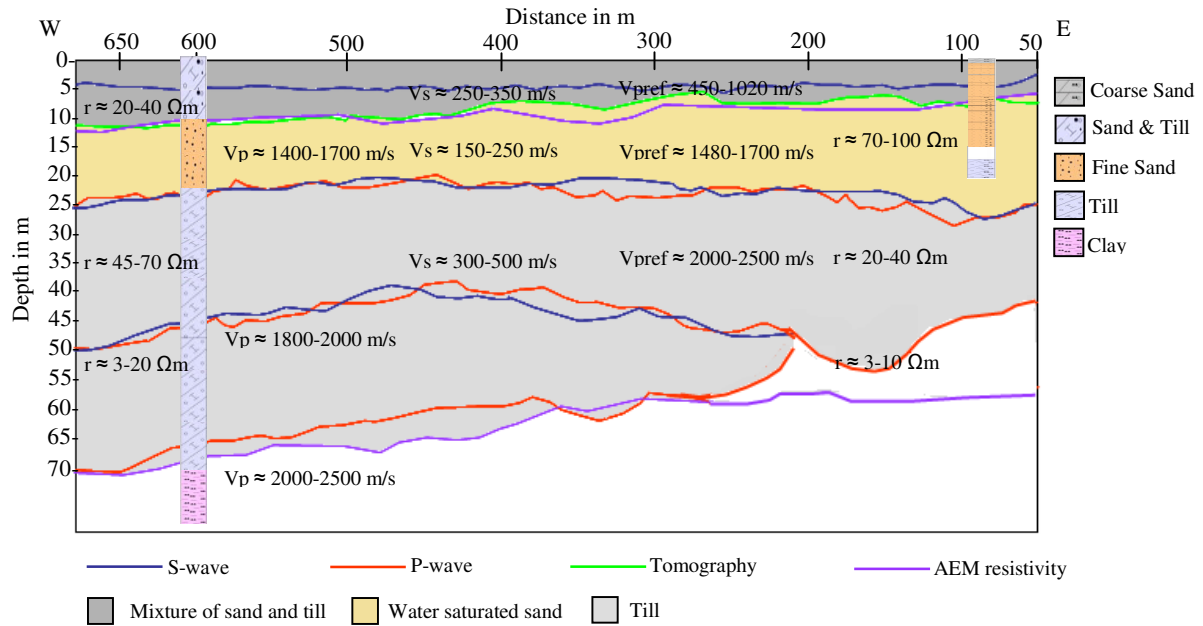
The results obtained show a good agreement among the methods, and they allow the near-surface lithological characterization of the area. The major lithological boundaries and sequences are recognized in the combined geophysical data sets (Figures 6.12 and 6.14). One can generalize that with the integrated interpretations three horizons are delineated: a heterogeneous mixture of near surface material mainly sand and till, a saturated sand column and till layer. In addition the stratigraphy boundaries between the above layers are outlined by most of the methods. Above all the accuracy of the seismic methods (refraction tomography, SSR and SPR) are well verified by combining the lithological information derived from the other geophysical methods.



Table 6.3 summarizes the obtained interpreted results for each of the above methods and the corresponding value of the measured physical properties.

Geophysical methods		Resulting depth (m)	Measured physical value	Interpretation
GPR		4/8	0.07 – 0.09 m/ns	The top of the saturated sandy layer
SSR		0 – 4/12	250 – 350 m/s	Mixture sand and till
		4/12 – 17/30	150 – 250 m/s	Saturated sand
		17/30 – 60	300 – 500 m/s	Till
SIP		2	~90 $\Omega$ m	Ground water table
		5 – 12	100 – 200 $\Omega$ m	Fine sand
		12 – 30	40 – 80 $\Omega$ m	Till
SPR		5 – 25	1400 – 1700 m/s	Saturated sand
		55 – 70	1800 – 2000 m/s	Till
		70 – 100	2000 – 2500 m/s	Clay
Refraction tomography		0 – 10	450 – 1020 m/s	Mixture sand and till
		10 – 30	1480 – 1700 m/s	Saturated sand
		30 – 50	1800 – 2400 m/s	Till
AEM	0 – 400 m	0 – 10	70 – 100 $\Omega$ m	Sand
		10 – 50	20 – 40 $\Omega$ m	Mixture till and clay
		50 – 70	3 – 10 $\Omega$ m	Clay
	400 – 720 m	0 – 25	20 – 40 $\Omega$ m	Till
		25 – 50	45 – 70 $\Omega$ m	Sand
		50 – 70	3 – 20 $\Omega$ m	Clay

**Table 6.3:** Summary of the interpreted results from GPR, SSR, SIP, SPR, AEM and refraction tomography. For all methods except for AEM the interpretation is based on the two nearby boreholes: B2 and Tangstedt-3914. AEM interpretation is based on the colour code definition from the BurVal working group report (Scheer et al., 2006).



**Figure 6.15:** Near-surface geologic model of the study area based on the seismic data, other geophysical data and the borehole information. Values of shallow P-wave reflection interval velocities ( $V_p$ ), P-wave refraction tomography velocities ( $V_{pref}$ ), shallow S-wave interval velocities ( $V_s$ ) and resistivities from AEM are shown for each layer.

## 7. Conclusion

Seismic reflection data (conventional/shallow) are contaminated by source-generated coherent noise - air wave, ground roll, guided waves, direct waves, refracted waves - especially in the near-surface depth range. The possibility to obtain reflections in the near-surface depth range depends on the separation of these coherent noises from reflected signals. However, most of the digital processing schemes are not sophisticated enough to fully enhance the reflected signals relative to these noises. Hence, these coherent noises limit the identification and interpretation of near-surface reflections. The other option is to use these noises to complement the near-surface zone in seismic reflection survey. Here I analysed the refracted waves (noise for reflection survey) from conventional reflection data by using the refraction tomography method and a promising result is found. And, the use of this unwanted signal (the refracted wave) allows for exploiting the information inherent in the reflection data to overcome the limitations of the conventional reflection method to improve the near-surface resolution.

In this regard, I examined the feasibility of processing conventional seismic reflection data using first arrival refraction tomography method to augment the near-surface stacked seismic section by a detailed velocity model. The P-wave reflection section (Figure 5.4) shows an observable shallowest reflection around 50 m. Even with the adaptation of high resolution P-wave reflection method in the same area it is only possible to get a shallow P-wave reflection as deep as 25 m (Figure 5.24). On the other hand, by inverting tomographically the refraction data from the conventional reflection data I succeed in determining a velocity contrasting boundary at around 10 m depth (Figure 5.6). It is confirmed from the borehole data that this velocity boundary is caused by lithological changes i.e. a mixture of till and sand and water saturated sand interface.

In general, the refraction tomographic approach was reliable and effective for defining the near-surface velocity model in the study area. The tomographic result gives a detailed velocity model (Figure 5.6), consisting of three contrasting velocity boundaries at ~10 m, ~30 m and ~50 m depth. The resultant velocity model is found to be compatible with knowledge supplied by the borehole, shallow P- and S-wave reflections and AEM data. This model includes a thin top layer of a mixture of dry sand, till and humus (velocities about 450 – 1020 m/s), a homogeneous layer of saturated sand (velocities about 1480 – 1700 m/s) and a till layer (velocities about 1800 – 2400 m/s).

High resolution P- and S-wave seismic reflection data were acquired along a coincident profile. The survey was carried out with the same acquisition parameter, 1 m geophone spacing and 2 m shot spacing. The resolution achieved with the P- and S-waves reflection data is depicted on Figures 5.24b and 5.31b, respectively. The P-wave reflection data permitted to get the uppermost reflection at about 25 m and the deepest reflection at about 200 m whereas the S-wave reflection data enabled the detection of a very near-surface reflection at about 4 m and the deepest reflecting interfaces at about 50 m. When a direct comparison is made between the P-wave and S-wave depth sections, two common reflections from the same interface are observed; at 25 m from the saturated sand and till interface and at 50 m (not observed in the nearby borehole data). The results demonstrate that the use of S-wave offers a better resolution for very shallow targets than the use of P-waves under commonly encountered subsurface conditions. Even if the combined application of both methods is costly the above result also shows that jointly using the two methods enable the derivation of more complete lithological information.

To better understand the relationship between seismic velocities and lithology in the near-surface zone a joint analysis of the P- and S-wave velocities via the velocity ratio is made. The P-wave velocity was found to be in the range of 550 to 2250 m/s (Figure 6.2a) and the S-wave velocity ranges between about 150 and 500 m/s (Figure 6.2b) for a depth down to 65 m. The average  $V_p/V_s$  ratio is 1.5 to 3.8 in the sand/till layer; 7.6 to 8.7 in the saturated sand column; 4.6 to 5.8 in the till layer and 5.2 to 6.2 to the clay section. The P-wave velocity has some ambiguity for the till-clay interface i.e. the velocity is expected to decrease while entering into the clay layer but this is not the case in most parts of the profile. This ambiguity could be first the large overlap of P-wave velocities in till and clay, second the accuracy of the estimated interval velocity from the reflection data. However, an increase of the velocity ratio is observed at the two layer interfaces which is as expected i.e. the  $V_p/V_s$  ratio increases with clay content.

To be reliable, the seismic methods (refraction tomography, shallow P- and S- wave reflection) are combined with the other geophysical methods - GPR, AEM and SIP - available in the area. Integration of the seismic data with these surface geophysical methods and borehole information reduces uncertainty in the interpretation of the seismic data for near-surface lithological characterization. The results obtained show a good agreement between the methods. The major lithological boundaries and sequences are recognized in the combined geophysical datasets (Figures 6.12 and 6.14). On the basis of the results from the seismic methods, the other geophysical methods and

from the knowledge of the boreholes it is also possible to construct a near-surface geological model of the study area. This geologic model consists of three horizons: a heterogeneous mixture of near surface material mainly sand and till, a saturated sand column and a till layer (Figure 6.15).

## References

- Aki, K., and Richards, P. G., 1980, Quantitative seismology: Theory and methods: W. H. Freeman and Co.
- Antes, H., and Wiebe, T., 1996, Analyses of waves in 3-D poroelastic media: Mechanics of poroelastic media, A.P.S., Selvadurai, 371-389 Kluwer Academic Publisher, Netherlands.
- Aracne-Ruddle, C. M., Bonner, B. P., Trombino, C. N., Hardy, E. D., Berge, P. A. Boro, C. O., Wildenschild, D., Rowe, C. D., and Hart, D. J., 1999, Ultrasonic velocities in unconsolidated sand/clay mixtures at low pressures, LLNL report UCRL-JC-135621, Lawrence Livermore National Laboratory, Livermore, California.
- Babuska, V., and Cara, M., 1991, Seismic anisotropy in the Earth: Kluwer Academic Publishers, Boston.
- Baker, G. S., Steeples, D. W., and Drake, M., 1998, Muting the noise cone in nearsurface reflection data: An example from southeastern Kansas: *Geophysics*, 63, 1332-1338.
- Biot, M.A., 1956a, Theory of propagation of elastic waves in a fluid-saturated porous solid. I. Low-frequency range: *Journal of the Acoustical Society of America*, 28, 168-178.
- Biot, M.A., 1956b, Theory of propagation of elastic waves in a fluid-saturated porous solid. II. Higher-frequency range: *Journal of the Acoustical Society of America*, 28, 179-191.
- Biot, M.A., 1962, Mechanics of deformation and acoustic propagation in porous media: *Journal of Applied Physics*, 33, 1482-1498.
- Bram, K., 1997, Der Kleinvibrator der NLFb-LIAG: Eine Energiequelle zur Untersuchung oberflächennaher Objekte. – *Mitt. Dt. Geophys. Gesellschaft*, 3, 2-6.
- BURVAL Working Group, 2006, Groundwater resources in buried valleys - a challenge for geosciences, ed R. Kirsch, H.M. Rumpel, W. Scheer, and H. Wiederhold. Hannover, Germany: Leibniz Institute for Applied Geosciences.

Butler, K. D., 2005, What is near-surface geophysics: Near Surface Geophysics: D. K. Butler, 1-6 (Investigations in Geophysics no. 13): SEG.

Butler, K., D., 2005, Near Surface Geophysics (Investigations in Geophysics no. 13): SEG.

Castagna, J.P., Batzle, M.L., and Kan, T.K., 1993, Rock Physics – The link between rock properties and AVO response: in Castagna, J.P., and Backus, M.M., eds., offset dependent reflectivity – Theory and practice of AVO anomalies: Society of Exploration Geophysics. Investigations in Geophysics, 8, 135-171.

Carr, B.J., Hajnal, Z., and Prugger, A., 1998, Shear-wave studies in glacial till: Geophysics 63, 1273.

Červený, V., 1987, Ray-tracing algorithms in three-dimensional laterally varying layered structures, D. Reidel, Norwell, Mass.

Claerbout, J. F., and Doherty, S. M., 1972, Downward continuation of moveout-corrected seismograms: Geophysics, 37, 741-768.

DiSiena, J.P., Byun, B.S., Fix, J.E., and Gaiser, J.E., 1984, F-K analysis and tube wave filtering, in Eds. Toksoz, N.M. and Stewart, R.R., Vertical Seismic Profiling, Part B-Advanced Concepts: Geophysical Press.

Domenico, S. N., 1984, Rock lithology and porosity determination from shear and compressional wave velocity: Geophysics, 49, 1188–1195.

Doornenbal, J.C., and Helbig, K., 1983, High-resolution reflection seismics on a tidal flat in the Dutch delta - acquisition, processing and interpretation: First Break, 1, No. 4, 9-20.

Ehlers, J., 1996, Quaternary and Glacial Geology: John Wiley and Sons, Chichester.

Fowler, C.M.R., Stead, D., Pandit, B.I., Janser, B.W., Nisbet E.G., and Nover, G., 2005, A Data Base of Physical Properties of Rocks from the Trans-Hudson Orogen, Canada, Can. J. Earth Sci. 555–572.

Gabriel, G., Kirsch, R., Siemon, B., Wiederhold, H., 2003, Geophysical investigation of buried Pleistocene subglacial valleys in Northern Germany: *Journal of Applied Geophysics*, 53, 4, 159-180.

Garg, S.K., Nayfeh, A.H., and Good, A.J., 1974, Compressional waves in fluid-saturated elastic porous media: *Journal of Applied Physics*, 45, 1968-1974.

Gray, S.H., Etgen, J., Dellinger, J., and Whitmore, D., 2001, Seismic migration problems and solutions: *Geophysics*, 66, 1622.

Grube, A., 2007, Nachfolge Burval, Schichtenverzeichnis, Landesamt für Natur und Umwelt des Landes Schleswig-Holstein.

Hardage, B. A., 1991, *Vertical Seismic Profiling, Part A: Principles*, Pergamon Press.

Hasbrouck, W.P., 1991, Four shallow-depth, shear-wave feasibility studies: *Geophysics*, 56, 1875-1885.

Helbig, K., 1987, Shear-waves – What they are and how they can be used, in Danbom, S.H. and S.N. Domenico, *Shear Wave Exploration*, SEG, *Geophysical Development*, 1, 19-38.

Hiltunen, D.R., Hudyma, N., Quigley, T.P., and Samakur, C., 2007, *Ground Proving Three Seismic Refraction Tomography Programs*, Florida department of transport, Florida.

Hoerdt, A., Blaschek, R., Binot, F., Druiventak, A., Kemna, A., Zisser, N., 2007, Case Histories of Hydraulic Conductivity Estimation with IP at the Field Scale, 13th European Meeting of Environmental and Engineering Geophysics, Istanbul, Turkey, 3–5 September 2007.

Hole, J.A., and Zelt, B.C., 1995, Three-dimensional finite-difference reflection travel times: *Geophysical Journal International*, 121, 427-434.

Hubral, P., Krey, T., 1980, Interval velocities from seismic reflection time measurements. 203 pages; SEG, Tulsa Oklahoma USA.



Inazaki, T., 1992, Development of subsurface survey methods. In Final Report of Research & Development of Utilization of Underground Space, 3, 2–26, Ministry of Construction (in Japanese).

Inazaki, T., 1999, Land Streamer: a new system for high-resolution S-wave shallow reflection surveys. Ann. Symp. Environ. Eng. Geophys. Soc. (SAGEEP1999) Expanded Abstracts, 207-216.

Inazaki, T., 2000, High-resolution S-wave reflection surveys for delineating near-surface geological structures: Proceedings of Geophysics.

Jaeger, J.C., Cook, N.G.W., and Zimmermann, R.W., 2007, Fundamentals of Rock Mechanics -4th ed., Blackwell Publishing.

Jenn, F., Knödel, k., Voigt, H.-J., 2007, Geological field observation: Environmental Geology: Handbook of Field Methods and Case Studies, K. Knödel, G. Lange, HJ. Voigt (eds.), 511-518: Springer Berlin.

Jensen, J.F., Ringgaard J., Skjellerup P., and Vangkilde-Pedersen, T., 2002, Pulled Array Seismic (PAS) - a new method for shallow, high resolution reflection seismic data acquisition: Proceedings of the 8th general annual meeting of the European Section of the Environmental and Engineering Geophysical Society (EEGS-ES, 2002), Aveiro, Portugal.

Kearey, P., Brooks, M., and Hill, I., 2002, An Introduction to Geophysical Exploration, (3rd. ed.), Blackwell.

Kirsch, R., 2006, Groundwater Geophysics: A Tool for Hydrogeology. Springer Berlin.

Knapp, R.W., and Steeples, D.W., 1986a, High-resolution common-depth-point seismic reflection profiling: Instrumentation: Geophysics, 51, 276-282.

Knapp, R.W., and Steeples, D.W., 1986b, High-resolution common-depth-point seismic reflection profiling: Field acquisition and parameter design: Geophysics, 51, 283-294.

Knödel, K., Lange, G., Voigt, H.-J., 2007, *Environmental Geology: Handbook of Field Methods and Case Studies*, Springer Berlin.

Kruppenbach, J. A., and Bedenbender, J. W., 1975, Towed land cable, US Patent 3 923.

Mavko, G., and Nur, A., 1995, Squirt flow in saturated rocks, *Geophysics*, 60, 97-107.

Mavko, G., Mukerji, T., and Dvorkin, J., 1998, *The Rock Physics Handbook: Tools for seismic analysis in porous Media*, Cambridge University Press, Cambridge.

Milholland, P., Manghnani, M. H., Schlanger, S. O., and Sutton, G.H., 1980, Geoacoustic modeling of deep-sea carbonate sediments: *J. Acoust. Soc. Am.*, 68, 1351-1360.

Milligan, P. A., Rector III, J.W., and Bainer, R.W., 1997, Hydrophone VSP imaging at a shallow site: *Geophysics*, 62, 842–852.

Miller, R.D., and Steeples, D.W., 1990, A shallow seismic reflection survey in basalts of the Snake River Plain, Idaho: *Geophysics*, 55, 761-768.

Miller, R.D., Anderson, N.L., Feldman, H.R., and Franseen, E.K., 1995, Vertical resolution of a seismic survey in stratigraphic sequences less than 100 m deep in southern Kansas: *Geophysics*, 60, 423-430.

Miller, C., Link, C., and Speece, M., 2003, Modified land streamer configuration for shallow seismic data acquisition: *SAGEEP Proceedings*, 857-865.

Moser, T. J., 1989, Efficient seismic ray tracing using graph theory. In 60th Ann. Internat. Mtg. : SEG, Expanded Abstracts, 1106-1108.

Moser, T.J., 1991, Shortest path calculation of seismic rays: *Geophysics*, 56, 59-67.

Møller, I., 2006, A ground penetrating radar survey at Hasloh in the Ellerbeker Rinne pilot area in the BurVal project: Data report. Danmarks og Grønlands Geologiske Undersøgelses Rapport 2006/xx. GEUS Kopenhagen.

Palmer D., 1981, An Introduction to the generalized reciprocal method of seismic refraction interpretation: *Geophysics*, 46, 1508-1518.

Park, C.B., Miller, R.D., and Xia, J., 1999, Multichannel analysis of surface waves (MASW): *Geophysics*, 64, 800-808.

Polom, U., 2005, Vibration generator for seismic applications, Patent application US 7,136,325 B2, USPTO, 14.11.2006.

Polom, U., Arsyad, I., Wiyono, S., Krawczyk, C.M., 2007, Classification of earthquake site effects by shallow reflection seismics using a shear-wave land-streamer system: AGU Fall Meeting AGU, Fall Meeting 2007 Abstracts.

Polom, U., Arsyad, I., and Kümpel, H.-J., 2008, Shallow shear-wave reflection seismics in the tsunami struck Krueng Aceh River Basin, Sumatra: *Adv. Geosci.*, 14, 135–140.

Prasad, M., and Meissner, R., 1992, Attenuation mechanisms in sands: Laboratory versus theoretical (Biot) data: *Geophysics*, 57, 710–719.

Pugin, A. and Pullan, S.E., 2000, First-Arrival alignment static corrections applied to shallow seismic reflection data: *Journal of Environmental & Engineering Geophysics*, 5/1, 7-15.

Pugin, A. J. M., Larson T. H., Sargent S. L., McBride J. H., and Bexfield C. E., 2004, Near-surface mapping using SH-wave and P-wave land-streamer data acquisition in Illinois, U. S.: *The Leading Edge*, 23, 677–682.

Pullan, S.E., and Hunter, J.A., 1990, Delineation of buried bedrock valleys using the optimum-offset shallow seismic reflection technique, in Ward, S., Ed., *Geotechnical and Environmental Geophysics, Volume III: Geotechnical: Soc. Expl. Geophys.*, 89-97.

Pullan, S.E., Hunter, J.A., and Neave, K.G., 1990, Shallow shear-wave reflection tests [Exp.Abs.]: *Soc. Expl. Geophys.*, 380-382.

Qin, F., Luo, Y., Olsen, K., Cai, W., and Schuster, G. T., 1992, Finite-Difference Solution of the Eikonal Equation: *Geophysics*, 57, 478-487.

Rabbel, W., 2006, *Seismic method: Groundwater Geophysics: A Tool for Hydrogeology*, R. Kirsch, 23-84, Springer Berlin.

Rawlinson, N., and Sambridge, M., 2003, Seismic Traveltime Tomography of the Crust and Lithosphere: *Advances in Geophysics*, 46, 81-197.

Rubin, Y., Hubbard, S.S., 2005, *Hydrogeophysics*, Springer, Netherlands.

Rucker, M. L., 2000, Applying the seismic refraction technique to exploration for transportation facilities: *Geophysics 2000 conference proceedings*, St. Louis, MO, Missouri Department of Transportation.

Rumpel, H.M., Grelle, T., Hölscher, F., and Stoll, M., 2005a, Vertikales Seismisches Profil (VSP) zur teufenabhängigen Geschwindigkeitsbestimmung im BurVal Messgebiet Ellerbeker Rinne – Bericht zur techn. Durchführung und Processing. - LIAG-Institut Hannover.

Rumpel, H.-M., et al., 2005b, Reflexionsseismische Untersuchungen der Ellerbeker Rinne bei Tangstedt und Schnelsen – Bericht zur technischen Durchführung und Processing. LIAG-Institut Hannover.

Saito, H., 1989, Traveltimes and raypaths of first-arrival seismic waves: computation method based on Huygens' principle: In 59th Ann. Internat. Mtg., SEG, Expanded Abstracts, 244-247.

Saito, H., 1990, 3-D ray-tracing method based on Huygens' principle: In 60th Ann. Internat. Mtg., SEG, Expanded Abstracts, 1024 – 1027.

Schanz, M., 2001, *Wave Propagation in Viscoelastic and Poroelastic Continua: Lecture Notes in Applied Mechanics Vol.2*, Springer-Verlag Berlin Heidelberg, Heidelberg.

Scheer, W., 2001, Untersuchungsprogramm zur Ermittlung des nutzbaren Grundwasserdargebotes im schleswig-holsteinischen Nachbarräum zu Hamburg (Südwest-Holstein). - Landesamt für Natur und Umwelt, Flintbek.

Scheer, W., Kröger, J., Kirsch, R., and Zarth, M., 2006, Ellerbeker Rinne, BURVAL Working Group: Groundwater resources in buried valleys – a challenge for geosciences, ed R.Kirsch,

H.M. Rumpel, W. Scheer, and H. Wiederhold, 205-226: Hannover, Germany: Leibniz Institute for Applied Geosciences.

Sheriff, R.E., and Geldart, L.P., 1982, Applied Geophysics, Cambridge University Press.

Sheriff, R.E., and Geldart, L.P., 1995, Exploration Seismology, Cambridge University Press, Cambridge.

Sheriff, R.E., 2002, Encyclopedic Dictionary of Applied Geophysics. 429 pages: SEG, Tulsa Oklahoma USA.

Skempton, A.W., 1954, The pore-pressure coefficients A and B, Geotechnique, 4, 143-147.

Siemon, B., Eberle, D., Rehli, H-J., Voß, W., Pielawa, J., 2006, Airborne Geophysical Investigation of Buried Valleys - Survey Area Ellerbeker Rinne, Germany, 2005/2006. BGR Report, Hannover.

Skvortsov, A.G., Hunter, J. A., Gorianinov, N.N., Burns, R. A., Tsarov, A. M., and Pullan, S. E., 1992, High-resolution shear-wave reflection technique for permafrost engineering applications: new results from Siberia: 62nd Ann. Internat. Mtg., SEG, Expanded Abstracts, 382-384.

Spitzer, R., Nitsche, F.O., and Green, A.G., 2000, Strategy for reducing source-generated noise in high-resolution seismic data: 62nd Ann. Internat. Mtg., EAGE, Expanded Abstracts.

Steeple, D.W., and Knapp, R.W., 1982, Reflections from 25 feet or less: 52nd Ann. Int. Mtg., Soc. Expl. Geophys., Expanded Abstracts, 469-471.

Steeple, D.W., 1984, High-resolution seismic reflections at 200 Hz: Oil and Gas J., 82, Dec. 3, 86-92.

Steeple, D. W., and Miller R. D., 1998, Avoiding pitfalls in shallow seismic reflection surveys: Geophysics, 63, 1213-1224.

Steeple, D.W., 2005, Near-surface geophysics 75 years of progress: The Leading edge 24, 582-585.

Stefani, J. P., 1995, Turning-ray tomography: *Geophysics*, 60, 1917-1929.

Stewart, R.R., Huddleston, P.D., and Kan, T.K., 1984, Seismic versus sonic velocities: A vertical seismic profiling study: *Geophysics*, 49, 1153-1168.

Stokoe, K. H., II, Wright, G. W., James, A. B., and Jose, M. R., 1994, Characterization of geotechnical sites by SASW method, in Woods, R. D., Ed., *Geophysical characterization of sites*: Oxford Publ.

Tatham, R. H. and McCormack, M. D., 1991, *Multicomponent Seismology in Petroleum Exploration, Investigations in Geophysics, Vol. 6*: Society of Exploration Geophysicists, Tulsa, Oklahoma.

Telford, W.M., Geldart, L.P., and Sheriff, R.E., 1990, *Applied Geophysics*, Cambridge University Press.

Todd, D.K., 1980, *Groundwater Hydrology* (2nd ed.), John Wiley & Sons, Ltd., Chichester.

Upadhyay, S.K., 2004, *Seismic Reflection Processing: with Special Reference to Anisotropy*: Springer Berlin Heidelberg.

Van der Veen, M. and Green, A.G., 1998, Land streamer for shallow data acquisition: evaluation of gimbal-mounted geophones: *Geophysics*, 63, 1408-1413.

Vidale, J. E., 1988, Finite-difference traveltimes calculation: *Bull. Seis. Soc. Am.*, 78, 2062-2076.

Vinje, V., Iversen E., and Gjoystdal H., 1993, Traveltime and amplitude estimation using wavefront construction, *Geophysics*, 58, 1157-1166.

Wang, H.F., 2000, *Theory of Linear Poroelasticity with Applications to Geomechanics and Hydrogeology*, Princeton University Press, Princeton, NJ.

White, D. J., 1989, Two-dimensional seismic refraction tomography: *Geophys. J.*, 97, 223-245.

Woolery, E. W., Wang, Z., Street, R. L., and Harris, J. B., 1996, A P- and SH-wave seismic investigation of the Kentucky Bend fault scarp in the New Madrid seismic zone: *Seismological Research Letters*, 66, 67-74.

Wyllie, M. R. J., Gregory, A. R., and Gardner, G. H. F., 1958, An experimental investigation of factors affecting elastic wave velocities in porous media: *Geophysics*, 23, 459-493.

Yilmaz, Oz., 1987, *Seismic data processing*: Society of Exploration Geophysicists.

Yilmaz, Oz., 2000, *Seismic Data Analysis (2nd ed.)*: Society of Exploration Geophysicists.

Yilmaz, Oz., 2001, *Seismic Data Analysis - Processing, Inversion and Interpretation of Seismic Data*. 2027 pages (2 volumes): SEG, Tulsa Oklahoma USA.

Zhang, J., Brink, U.S., and Toksoz, M.N., 1998, Nonlinear refraction and reflection traveltimes tomography: *Journal of Geophysical Research*, 103, B12, 29,743-29,757.

## **Résumé**

**Genet Tamiru HabteSelassie**

**P.O.Box 23901 Code 1000**

**Addis Ababa, Ethiopia**

**Tel.: 251 – 115 50 29 77 (Home)**

**251 – 911 66 51 07 (Cell phone)**

**Email: [gentamiru@hotmail.com](mailto:gentamiru@hotmail.com)**

**[gentamiru@gmail.com](mailto:gentamiru@gmail.com)**

**Date and Place of Birth:** 12 October 1973, Addis Ababa, Ethiopia

**Sex:** Female

**Nationality:** Ethiopian

**Marital Status:** Married

### **Educational Background**

- PhD candidate at Leibniz Institute for Applied Geophysics, LIAG and Leibniz University of Hanover, Germany, since 2005. Dissertation topic: ***"Lithological Relevance of Near - Surface Seismic Velocity Model"***
- MSc in Applied Geophysics, Department of Earth Science, Addis Ababa University. (2000 - 2002)
- BSc in Physics, Addis Ababa University, Faculty of Natural Science, Department of Physics. (1988 - 1992)
- Completed Secondary School with distinction at *Abyot Kirs* Secondary School, Addis Ababa. (1985 - 1988)
- Completed Elementary School with distinction at St.Jared Public School, Addis Ababa. (1979 - 1985)



## **Job Experience**

### **Teaching Physics at:**

- *Ediget Adult's Boarding College, Addis Ababa (As Instructor from 1998 - 2004)*
- *Nefasilk Comprehensive Secondary School, Addis Ababa (1995/96)*
- *Mekane-Selam High School, Borena, Wello Region (1992/93)*
- *Fana School (1997)*

### **Other**

Serve as coordinator and instructor of Computer Literacy Course at Progress Computer Service PLC. (1996/97)

### **Publications**

1. Masters Thesis: "*Integrated Geo-physical Investigation for Ground Water Exploration in East Akaki, South of Addis Ababa.*"
2. "*Exploring the very near surface depth range with seismic methods – three different ways.*" G.TAMIRU, H.WIEDERHOLD, & U.POLOM, (2008), Poster, 68. Jahrestagung der Deutschen Geophysikalischen Gesellschaft, 3.-6.3.2008; Freiberg.

### **References:** 1. Pro.Dr. Hans-Joachim Kümpel

Tel.: 49 511-643-2243

Email: Hans-Joachim.Kuempel@bgr.de

### 2. Dr. Helga Wiederhold

Tel.: 49 511-643-3520

Email: Helga.Wiederhold@liag-hannover.de

### 3. Dr. Tigstu Haile

Tel.: 251-111 23 94 62

Email: htigistu@geol.aau.edu.et

## **Erklärung zur Dissertation**

Hierdurch erkläre ich, dass die Dissertation "Lithological Relevance of Near-surface Seismic Velocity Model" selbstständig verfasst und alle benutzten Hilfsmittel sowie evtl. zur Hilfeleistung herangezogene Institutionen vollständig angegeben wurden.

Die Dissertation wurde nicht schon als Diplom- oder ähnliche Prüfungsarbeit verwendet.

Hannover, den 21.07.09

---

(Unterschrift)

Genet Tamiru